Real-Time Monitoring of Thermal Processes

by

Lucas A. Botelho

A thesis

presented to the University of Waterloo

in fulfillment of the

thesis requirement for the degree of

Doctor of Philosophy

in

Mechanical and Mechatronics Engineering

Waterloo, Ontario, Canada, 2023

Examining Committee Membership

The following served on the Examining Committee for this thesis. The decision of the Examining Committee is by majority vote.

External Examiner	NAME: YuMing Zhang Title: Professor, Electrical and Computer Engineering
Supervisor	NAME: Amir Khajepour Title: Professor, Mechanical and Mechatronics Engineering
Supervisor	NAME: Adrian Gerlich Title: Professor, Mechanical and Mechatronics Engineering
Internal Member	NAME: Mihaela Vlasea Title: Associate Professor, Mechanical and Mechatronics Engineering
Internal Member	NAME: Peng Peng Title: Assistant Professor, Mechanical and Mechatronics Engineering
Internal-external Member	NAME: John Zelek Title: Associate Professor, Systems Design Engineering

Author's Declaration

This thesis consists of material all of which I authored or co-authored: see Statement of Contributions included in the thesis. This is a true copy of the thesis, including any required final revisions, as accepted by my examiners.

I understand that my thesis may be made electronically available to the public.

Statement of Contributions

I would like to acknowledge the names of my co-authors who contributed to the research described in this thesis, these include:

Prof. Amir Khajepour: Supervising the research, generating novel concepts for this thesis, facilitating access to laboratory resources, and reviewing/proofreading papers.

Prof. Adrian Gerlich: Supervising the research, reviewing/proofreading papers, facilitating access to laboratory resources, and support in material characterization.

Dr. Mohammad Farshidianfar: Providing expertise in laser directed energy deposition, providing technical support in design of and conducting experiments, and reviewing papers.

Richard van Blitterswijk: Brainstorming and developing early concepts in convolutional neural networks for geometry monitoring. Providing technical support in design of and conducting experiments. Reviewing and editing papers and conference presentations.

Abstract

In this research, a monitoring system for thermal processes was developed which measures the most critical process phenomena, such as thermal dynamics (peak temperature, heating rate, and cooling rate) and geometric features, in real-time, which can be used for quality assurance and real-time feedback control. Thermal processes are a subset of manufacturing processes that are characterized by heating materials with a concentrated heat source to alter the properties of the materials or join them. Metal additive manufacturing and arc welding processes are considered thermal processes, where the concentrated energy source may be in the form of a laser, electron beam, electric arc, etc. While thermal processes can be used to create complex components without the limitations of traditional manufacturing, process disturbances may cause deviations from expected results.

During thermal processing, geometry and thermal dynamics of the heat affected zone (HAZ) directly influence the quality of the produced products. Therefore, it is critical to have an accurate tool to monitor the geometry and thermal dynamics in real time to better assure the quality of the part. Various sensors are available to measure these properties, though imaging is a common theme among thermal process monitoring. Imaging is an effective technique since it allows for non-contact in-situ measurements. Imaging in different wavelengths can provide different information regarding the HAZ, such as the temperature distribution from infrared (IR) light. While high resolution, and high frame rate geometry measurements from visible light can be monitored directly. Moreover, processing images with machine learning algorithms has also been shown to be capable of predicting porosity and detecting defects in the part being manufactured. Therefore, the monitoring system designed in this research features high dynamic range (HDR) visible light and IR dual camera sensors with a common optical path to monitor the geometry and thermal dynamics, with the potential to implement machine learning to monitor other features in the future. An enclosure was designed to house both sensors with a common optical setup for the sensors to have a similar field of view (FOV).

In this work, the IR sensor was used to create a dataset to predict the temperature distribution of the HAZ with the HDR sensor. From the temperature distribution, thermal dynamics such as peak temperature, cooling rate, heating rate, solidification time, and melting time were calculated in real-time to estimate the material properties of the final part. The HDR sensor was also used to predict the geometry of the deposited material (clad). Using the same sensors, the height and width of the

deposition are estimated from the captured images in real-time which are used for deposition geometry control. The geometry prediction algorithm evolved during this work with different algorithms and features used in the measurements to improve the robustness and accuracy of geometry measurements.

To test the effectiveness of the monitoring system, laser heat treatment (LHT) experiments were conducted to initially validate the thermal dynamics measurements. Thermal dynamics were then further validated during laser directed energy deposition (LDED), which was additionally used to validate the geometry measurements of the clad. Moreover, gas metal arc welding (GMAW) experiments were conducted as well to demonstrate the potential for using this system for different energy sources and materials.

The developed dual sensor camera was shown to be capable of capturing images in real-time during thermal processes. Processing the visible-light images allows the geometry of the HAZ to be monitored, while the IR sensor provides its temperature distribution. The system was shown to be robust enough to capture data with multiple materials (stainless steel and nickel-based alloys) and with different energy sources (laser and electric arc). The thermal dynamics measured with this tool have been shown to correlate to the material properties of the produced parts, thus demonstrating the potential to infer the material properties from these measurements. It has also been shown that a cost-effective alternative design using the visible light sensor to predict the temperature distribution with calibrated measurements from a pyrometer may be used for temperature measurements in thermal processes. Therefore, the developed monitoring system is shown to be an effective monitoring and control tool for various thermal processes.

Acknowledgements

First, I would like to express my gratitude to Professor Amir Khajepour, his guidance and experience was instrumental in my ability to complete this thesis. I would also like to thank Professor Adrian Gerlich for offering his insight and providing access to testing equipment and training to validate this research. A special thanks to Mohammad Farshidianfar whose previous research and laboratory expertise has been the building blocks of this work.

The University of Waterloo has been a fulfilling research and academic environment, I would like to thank all of those at the University involved in creating such a pleasant environment. I would especially like to thank Richard van Blitterswijk, with whom I spent countless hours conducting experiments and whose support increased the quality of this research. Moreover, I would like to thank the technicians in the Mechatronics Vehicle Systems Lab, Jeff Graansma, Aaron Sheratt and Adrian Neill for their technical expertise.

I would like to thank my extended family and friends for their support, patience, and encouragement throughout this experience. Especially, I would like to thank Sarah Moasser for her support and general feedback.

Finally, I would also like to express my sincerest gratitude to my parents, John and Filomena Botelho, and my brother, Alexander Botelho, who have shaped me into the person I have become, without them none of this would have been possible.

Dedication

This thesis is dedicated to my beloved family.

Table of Contents

List of Figures

List of Tables

List of Abbreviations

AM	Additive Manufacturing
ALFa	Automated Laser Fabrication
CAD	Computer Aided Design
CAM	Computer Aided Manufacturing
CAMJ	Centre for Advanced Material Joining
CCD	Charged-Coupled Device
CMOS	Complimentary Metal-Oxide-Semiconductor
CNC	Computer Numerical Controlled
CNN	Convolutional Neural Network
CT	Computerized Tomography
DED	Directed Energy Deposition
FCC	Face Centered Cubic
FEA	Finite Element Analysis
FOV	Field of View
GMAW	Gas Metal Arc Welding
HAZ	Heat Affected Zone
IR	Infrared
IWS	Intelligent Welding System
LAM	Laser Additive Manufacturing
LC	Laser Cladding
LCR	Laser Cladding Remanufacturing
LDED	Laser Directed Energy Deposition
LHT	Laser Heat Treatment
LIBS	Laser Induced Breakdown Spectroscopy
LMP	Laser Material Processing
LSTM	Long Short-Term Memory
MAPE	Mean Absolute Percent Error
MIMO	Multi-Input Multi-Output
ML	Machine Learning

MOC	Monitoring Optimization and Control
MPC	Model Predictive Control
MPCA	Multilinear Principal Component Analysis
NI	National Instruments
NIR	Near Infrared
NIST	National Institute of Standards and Technology
NN	Neural Network
PA	Photoacoustic
PBF	Powder Bed Fusion
PID	Proportional-Integral-Derivative
RNN	Recurrent Neural Network
SISO	Single-Input Single-Output
SLS	Selective Laser Sintering
SWIR	Short-Wave Infrared
UT	Ultrasonic Testing
WAAM	Wire Arc Additive Manufacturing

List of Symbols

t_i	Time
i	Timestep index
T_{Peak}	Peak Temperature
T_{Phase}	Critical temperature where a phase change occurs
t_{Peak}	Time that the HAZ reaches the peak temperature
t_{Phase}	Time when the HAZ undergoes a phase change
$R_{cooling}$	Cooling Rate
n	Number of Frames
f	Camera Framerate
$t_{solidification}$	Solidification Time
$t_{sol.,ss}$	Steady State Solidification Time
Δx	Displacement for cooling rate calculation
Δx_2	Displacement for heating rate calculation
v	Scanning Speed
d	Observable distance from top of the clad to the bottom of the clad
d_w	Distance from the center of the laser to the edge of the melt pool
w	Clad Width
θ	Camera Angle
α	Camera Angular FOV
b	Displacement of circle center in y-direction for clad cross-section geometry
r	Radius of circular arc which describes the clad cross-section

Chapter 1
Introduction

1.1 Motivation

There are various manufacturing methods which rely on a concentrated energy source to heat the material to change the part geometry and/or material properties. These methods include laser material processing (LMP), electron-beam processing, and many forms of welding. LMP can be further divided into two distinct processes: (1) laser additive manufacturing (LAM), and (2) laser heat treatment (LHT). Collectively these manufacturing processes will be referred to as thermal processing, because of the high temperatures experienced.

Thermal processes all feature a concentrated energy source and are typically used while working with metals; therefore, thermal processes all feature similar operating temperatures. The concentrated energy source, which may be a laser, electron beam, or electric arc, creates a relatively small heat affected zone (HAZ) in the metal workpiece, along with a melt pool if temperature is sufficient to melt the workpiece. The geometry and material properties can then be measured from the HAZ as the material in this area rapidly cools. The common thermal processes explored in this work include LHT, laser directed energy deposition (LDED), and gas metal arc welding (GMAW).

In thermal processes a fully dense component can be produced using appropriate process parameters; parameters including laser power and scanning speed. However, the interaction between the process parameters directly affects the thermal dynamics (peak temperature, heating rate, and cooling rate) of the HAZ. Accordingly, the complex thermal dynamics result in different microstructures and consequently, mechanical characteristics. Thereafter, these parameters lead to the generation of complex hydrodynamic fluid flows and accordingly change the crystal growth, orientation, and presence of microstructural defects [1]. Though the potential exists for these manufacturing methods to create complex parts, these fabrication techniques remain unreliable since any disturbances to process parameters or deviations in manufacturing conditions can result in large deviation in material properties and geometry. Hence, there is a strong desire to implement closed-loop control to correct errors found in the process in real-time to reduce the deviation between the real and the desired properties of manufactured parts. Process disturbances are also corrected with closed-loop control by reducing the errors caused by sudden changes to the state of the system. To apply closed-loop control with manufacturing processes there must first be accurate measurements to determine the current state of the

system. Therefore, there is a need for accurate real-time monitoring of key phenomena, such as thermal dynamics and geometric features, during thermal processing to establish control and improve the quality of parts fabricated within this field of manufacturing.

The goal of this research is to create and validate an integrated real-time monitoring system which can capture key features during the thermal processes mentioned above. Though the phenomena needed to be measured are slightly different from each of these processes, the similar size and temperature range of the HAZ allow the same sensors to be used to capture the relevant data for all processes. LHT is used to alter the material properties of the substrate; therefore, it is most critical to monitor features that can be used to estimate the microstructure and material properties. During LDED, the geometry of the added material must be monitored since that determines the dimensional accuracy of the final part. However, microstructure must be known as well, since predicting the material properties is essential to ensure that the strength of the part is consistent throughout and meets the requirements. In GMAW, it is crucial to know the quality of the weld bead to ensure the joint is sufficient for the application, which is determined by the material properties and geometry of the weld bead. Another common concern across all thermal processes is the presence of defects and porosity in final parts, which is present in these processes. Moreover, monitoring the defects and porosity in real-time would also provide a more accurate estimate for the part's overall strength than the microstructure alone. Finally, since LAM parts are notorious for containing imperfections, monitoring these phenomena in real-time would eliminate the need to qualify each part after the process, allowing it to be a cheaper and more reliable manufacturing technique for complex parts. Therefore, it has been determined that estimating the material properties is critical for all thermal processes, and geometry is critical for the subset which includes added material.

Real-time in-situ monitoring represents the initial step in improving the quality of parts produced through LMP and other similar fabrication techniques since it provides information on the current state of the process. As mentioned earlier, the error between desired properties and current properties can be used for closed-loop control to improve the quality of produced parts. Alternatively, this information can be integrated with quality assurance; where if a fatal flaw is found, the process can stop immediately without wasting time and material, finishing the part and checking the quality in post-processing. Therefore, accurate monitoring would provide improvements to the quality of parts fabricated through thermal processes by reducing the need of post-processing, stopping the process if a flaw is detected and providing the foundation for correcting process errors in real-time. Review articles within the field

of DED have also stated the necessity of real time measurements of geometry and microstructure to enhance the reliability and repeatability of DED [2].

1.2 Thermal Processes

Thermal processes are an advanced field of manufacturing in which a concentrated energy source is utilized to fuse materials or change the material's properties. In this research three specific thermal processes are analyzed: (1) LHT, where a laser is used to heat a metal substrate to change its properties, (2) LDED, which implements a laser to melt and fuse metal powder to fabricate complex parts layer by layer, and (3) GMAW, which uses an electric arc between the wire feed and workpiece to form the weld bead while joining materials. In these processes, the HAZ, which is the region of the material that is affected by the concentrated energy source, can be analyzed to determine the thermal dynamics and geometry in real-time.

1.2.1 Laser Heat Treatment

LHT is typically utilized to enhance resistance to corrosion, oxidation, wear, and surface degradation of engineering materials. Only a thin surface layer of the substrate (instead of the entire bulk) is rapidly heated to change the material's phase followed by rapid self-quenching (by conduction through the cooler bulk) to produce the desired microstructure [3]. In LHT, shielding gas is provided to the HAZ to protect it from oxidation, as this phenomenon occurs more rapidly at higher temperatures [4]. A schematic of the LHT process is displayed in Figure 1-1, where the key components are highlighted.

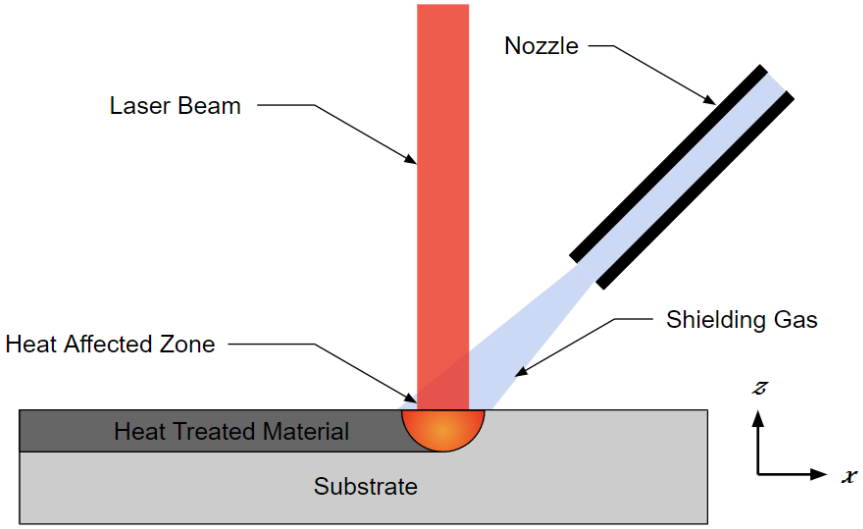

Figure 1-1 Schematic of laser heat treatment

1.2.2 Laser Directed Energy Deposition

Additive manufacturing (AM), a process of joining materials to make objects from three-dimensional (3D) models layer by layer [5]. AM is a growing field in manufacturing due to its ability to produce parts with complex geometries [6], of which, direct energy deposition (DED) is a subset. DED is an AM process in which a heat source is used to generate a small portion of melted material (melt pool) on the substrate surface and simultaneously deposit the additive material onto the substrate. As both a thin layer of the substrate and the additive material are fully melted, metallurgical bonding can be formed with very high bonding strength since the melt pool is rapidly cooled to form a solid layer [7]. LDED is a DED process which involves using a high-energy laser beam as the heat source to melt the feedstock material and a small region of the substrate, allowing it to bond and solidify, forming a desired structure or part. LDED is commonly used for rapid prototyping, repair of components, and the production of complex geometries in industries such as aerospace and automotive. A schematic representation of the process is summarized in Figure 1-2.

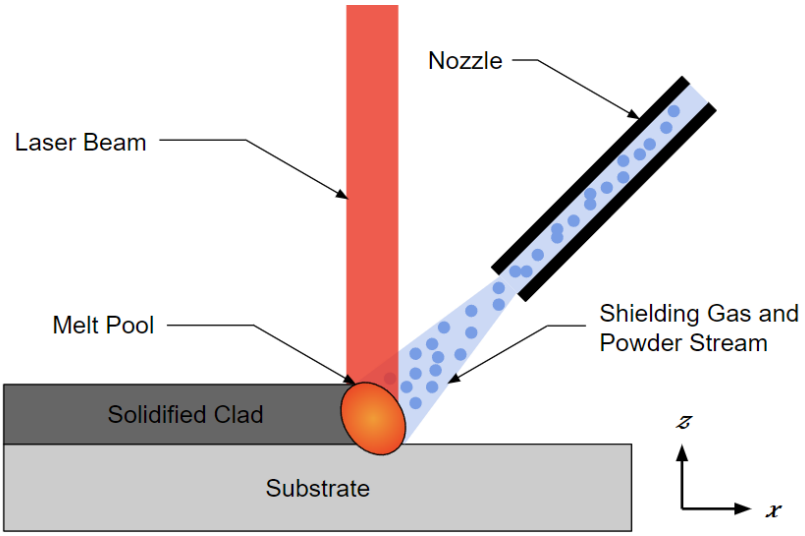

Figure 1-2 Schematic of laser directed energy deposition

1.2.3 Gas Metal Arc Welding

Welding is a fabrication process whereby two or more parts are fused together by means of heat, pressure, or both. While welding includes many variations, a subset of welding techniques can be considered thermal processes, including laser and arc welding. In these welding processes, the material is rapidly heated above the melting temperature to form a melt pool [8, 9]. Specifically, GMAW is a welding process that utilizes an electric arc formed between a consumable wire electrode and the

workpiece to create a weld joint. During GMAW, shielding gas is used to protect the weld area from atmospheric contamination. The consumable wire electrode is continuously fed through a welding gun, and the electric current creates an arc that melts the electrode and a small region of the workpiece, forming a weld bead. GMAW is widely used in various industries for its versatility, high welding speed, and ability to weld different types of metals. Figure 1-3 illustrates the key components of the GMAW process.

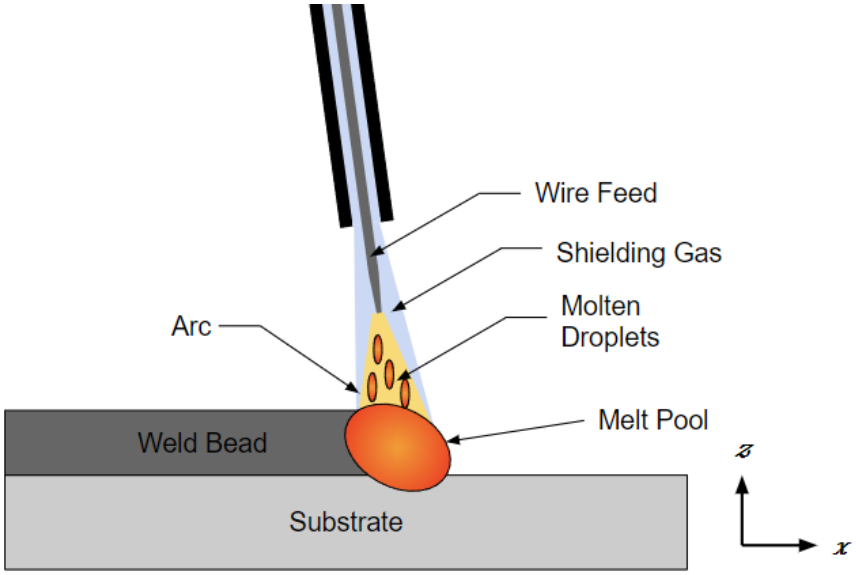

Figure 1-3 Schematic of gas metal arc welding

1.3 Statement of Objectives and Scope

The main goal of this research is to develop a robust system for real-time cost-effective monitoring of critical process phenomena, which are driven by the process parameters, during various thermal processes with different materials for the use of real-time control and quality assurance.

To achieve this goal, this research is divided into the following objectives:

a) Develop a monitoring system capable of capturing both geometric measurements and thermal dynamics in real-time. Experimental validation must be conducted to verify the correlation between the geometry measured from images captured during thermal processes and reliable measurements found in post-processing.

b) To monitor thermal dynamics, such as the peak temperature of the melt pool, the cooling rate, solidification time and the heating rate, with a cost-effective methodology featuring a CMOS

camera used in conjunction with pyrometry measurements to estimate the temperature distribution of the HAZ.

c) Determine the correlation between thermal dynamics and material properties to demonstrate that thermal dynamics are an effective metric to monitor the material properties of the workpiece during thermal processes.

d) Prove the system is robust by implementing it on multiple different systems within the field of thermal processes. Moreover, the system must be validated with different materials and different process parameters to demonstrate its effectiveness at monitoring the key features of different experimental conditions.

e) Implement the real-time measurements from this system with a variant of proportional-integral-derivative (PID) control to exhibit its effectiveness to be used with control algorithms to reduce errors encountered during thermal processes.

1.4 Thesis Overview

The proposal is divided into seven chapters. **Chapter 2** provides a review of the literature related to the topic of monitoring thermal processes to highlight the contribution and novelty of this work. The current standards of monitoring geometry, material properties, defects, and porosity are discussed since these properties are most critical during thermal processing.

The design of the monitoring system and experimental setups used to validate the system are discussed in **Chapter 3**. Where the design decisions and constraints are detailed to describe how the hardware was created for real-time monitoring. Additionally, the experimental setups used to validate the system are shown to illustrate the robustness of the measurements with various thermal processes.

In **Chapter 4**, the methodology in which geometry measurements are extracted from images in real time is discussed. This includes monitoring the geometry of single tracks created through LDED measured with model-based approximations and utilizing machine learning to predict geometry from multi-layer and adjacent tracks created with LDED and GMAW.

Chapter 5 describes cost-effective methods to predict the temperature distribution of the HAZ in real-time from visible light imaging. Initially, temperature distribution was estimated with a combination of machine learning algorithms and a mathematical model of the HAZ. Later iterations of

temperature prediction were created by using a high dynamic range camera and determining a correlation between camera intensity and temperature based on Planck's law.

The results and performance of the real time geometry and thermal dynamics measurements are presented in **Chapter 6**. This chapter shows how material properties can be extracted from real-time thermal dynamics measurements. Moreover, PID control is used to demonstrate the effectiveness of the measurements derived from this system being used to improve the quality of parts produced through thermal processes.

Finally, **Chapter 7** provides a summary of the results and contributions of this research. Moreover, future work is also proposed in this section to improve the performance of real time monitoring and to outline other features that may be monitored with this system.

Chapter 2
Literature Review and Background

In this chapter, existing tools and methodologies for monitoring key features in thermal processes are reviewed. This outlines which features are deemed most critical to be monitored in real-time and what tools are being used to do so. The correlation between the available sensors and desired features is explored to provide an understanding of how sensors are selected for thermal process monitoring. Finally, the limitations of current systems and how this research iterates on the foundation of literature is highlighted.

2.1 Geometry Monitoring in Thermal Processes

Some forms of thermal processes such as welding and LAM feature deposited material fused to the substrate, this added material is referred to as the clad. During thermal processes it is observed that monitoring is essential since deviations in the geometrical accuracy of the clad are compounded by future layers [10, 11]. Moreover, it has been shown that despite using constant process parameters the height of subsequent layers can vary, further motivating the need for geometry monitoring [12]. Unfortunately, there are limited means in which geometry is measured during AM processes, and there is wide variation between the algorithms currently implemented. Some methods are only capable of monitoring one dimension such as either the height or the width, and others are not capable of working in real-time. Though some algorithms can successfully monitor the height and width, these depend on the orientation of the monitoring device and are not suitable for all applications.

2.1.1 Monitoring Melt Pool Geometry

Some tools are designed to monitor the shape of the molten portion of the deposition, the melt pool, to predict the final geometry of the deposited material. One approach to measure the height in real-time during DED was explored by Iravani et al. in which images of the melt pool were captured by three cameras positioned 120° apart [13]. Of the three images captured at each timestep, the two most appropriate images were selected for image processing based on the direction of cladding since the system is designed to work for any direction in 360°. Once the images were selected, image thresholding was used to separate the clad from other features in the image, where the optimal threshold is found using a fuzzy logic approach. An ellipse is then fitted to the melt pool of each image and the

major and minor axes of each ellipse, and the scanning direction are used to determine the height of the clad. The five features are input to a recurrent neural network (RNN) which estimates the height based on previously recorded data which the RNN was trained with. The model was able to predict the clad height with an average error of approximately 12%. Though height could be measured for any scanning direction the width could not be measured with this system.

Song et al. also developed a trinocular system to monitor the height of LAM in [14], however, the methodology differed from prior work [13]. By thresholding the images from all three cameras the approximate shape and location of the melt pool can be found. The centroid of the melt pool is then determined from each image to estimate the height of the clad. The three calculated heights are compared to the reference height to determine the necessary control effort.

ML has also been used in monitoring other geometric properties in thermal processes, such as in-situ monitoring of weld penetration [15]. In this work, several methods are summarized which feature deep-learning to predict penetration in weld penetration with convolutional neural networks (CNNs). Penetration has been achieved with high dynamic range (HDR) cameras, infrared (IR) cameras, and other sensors. Utilizing the reflectivity of the weld pool surface is one case in which another sensor was used to monitor features during welding [16].

An alternative approach to measuring geometry of the clad is to measure the width of the melt pool in real-time. A variation of this is described by Hofman et al., where a camera is setup with a field of view (FOV) colinear to the laser allowing the melt pool to be captured from an aerial perspective [17]. Figure 2-1 displays the experimental setup of this work and demonstrates how images were processed to extract the width of the clad. Image thresholding was performed on the images captured by the camera and an ellipse was fitted to the remaining image. The width of the ellipse was measured and controlled to ensure clad had a consistent width throughout the printing process. By controlling the melt pool width in real-time the authors were able to maintain more consistent properties such as dilution and hardness, but the authors did not report how the height was affected by this control. A similar methodology has been used to monitor the width of the melt pool by Ding et al. in [18] and Liu et al. in [19]. A notable difference is the use of the IR spectrum of light to eliminate the noise caused by the powder above the melt pool. While Hofman et al. [17] used the image acquired by a CCD camera and image thresholding to determine the size of the melt pool, others have used [18, 19] thermal contours to extract the size of the melt pool. In both cases, only the width of the melt pool can be measured and

controlled. Though a coaxial camera is best suited for monitoring the area or width of the melt pool, it is possible to augment the data with other sensory information to provide height estimation as well. This was done by Aubry et al. where the width of the clad was measured with a coaxial CCD camera and triangulation measured the height [20]. However, a disadvantage of this system is the need for two cameras to measure the geometry, and if the 2D trajectory is not oriented, the system requires three cameras.

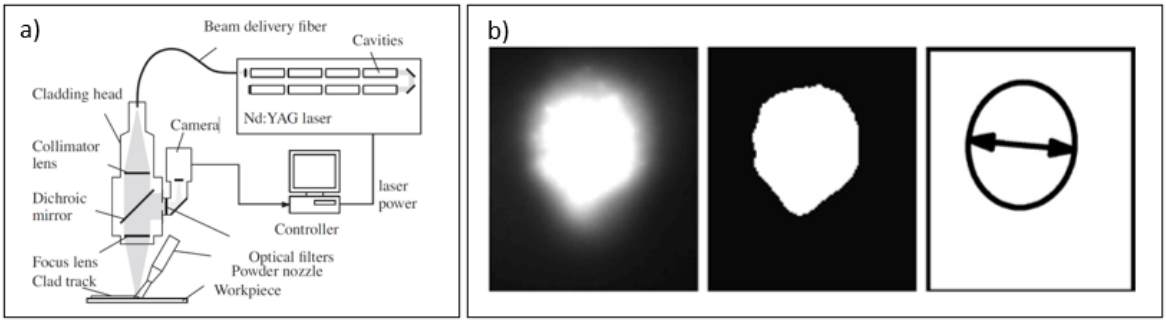

Figure 2-1 Coaxial width monitoring a) experimental setup b) image processing to extract width [17]

Real-time monitoring of the clad height during DED with a camera positioned with a leading view of the melt pool has been patented by Suh [21]. To monitor the geometry of the clad a camera is positioned, at some angle above the substrate, in front of the melt pool to capture images of the leading edge of the melt pool. Similar to some of the previously described methods, an ellipse is fit to the melt pool and the major and minor axes of the ellipse are measured. Suh has determined that from these axes of the melt pool the height of the clad can be measured and controlled. Meriaudeau et al. used a similar method to monitor the geometry of the clad in real-time [22]. However, the camera was positioned directly in front of the melt pool on the plane of the substrate, allowing the height and width of the clad to be measured directly once an edge detection algorithm was used to differentiate the clad from the surrounding environment. Though this monitoring system is adequate to measure the height and width simultaneously, it is not always feasible to mount the camera directly in front of the clad.

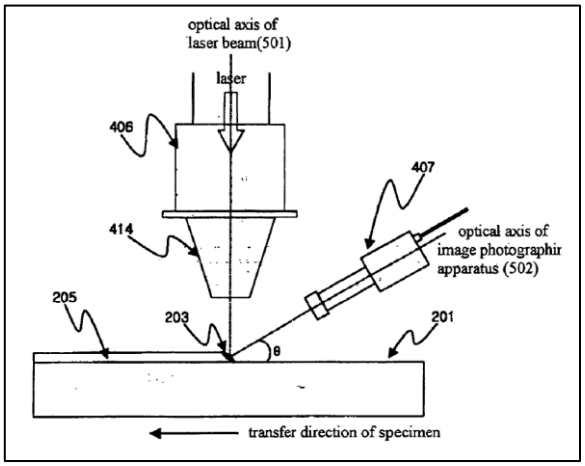

Figure 2-2 Real-Time monitoring of LDED with a leading view, invented by Suh [20]

Though the previous literature is focused on measuring the geometry during DED, other forms of thermal processes have similar challenges in geometry monitoring. Since welding has a similar HAZ to AM, geometry monitoring can be done with the same methodology; therefore, signals captured by CCD or X-ray cameras can provide position and shape information [23]. Where X-ray imaging features a focused beam of high-energy X-ray photons directed through the melt pool, creating an image on a detector [24]. These images then undergo image processing or machine learning to differentiate the melt pool from the bulk material in real-time [25]. Once the melt pool is differentiated, either by temperature or pixel intensity, the geometry is estimated.

In wire-fed DED, CNNs have been implemented to predict the geometry of the melt pool from images and thermal dynamics (temperature history) captured in real time, as shown in [26]. The CNN developed by Jamnikar et al., shown in Figure 2-3, was designed to take images of the melt pool and its thermal profile as inputs to predict the geometric properties of the deposition. Using these inputs, the CNN was able to predict the height, width, fusion zone depth and fusion zone area. The percentage error in prediction was shown to be 14% for bead height, 14% for bead width, 8% for fusion zone depth, and 9% for fusion zone area. Thus, demonstrating the potential for using CNN for geometry prediction in DED, however, this algorithm was limited to single-track depositions.

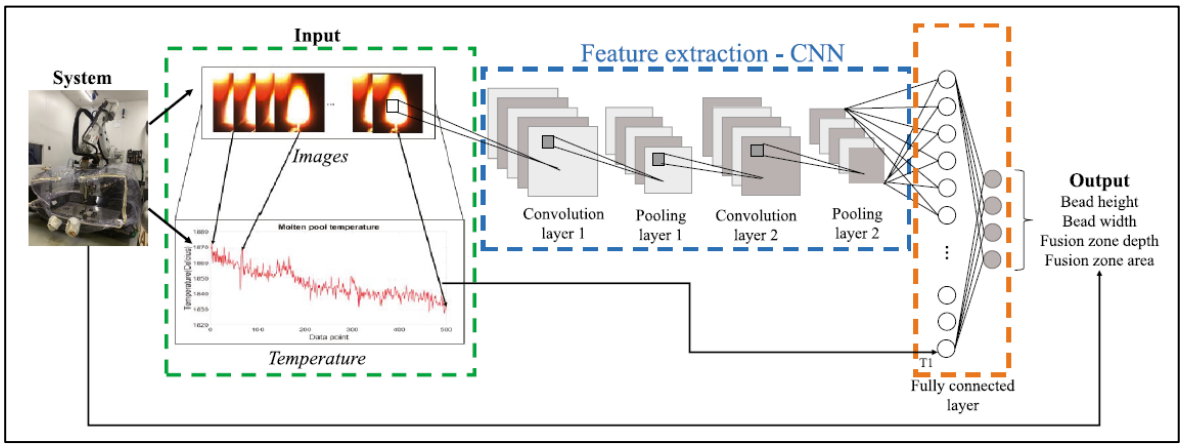

Figure 2-3 Sensing-geometry relations modeling using m-CNN for geometric parameter prediction using molten pool images and temperature data [26]

Melt pool depth is a feature that cannot be directly observed in DED, though it has an influence on the material properties of the final part. A neural network (NN) was developed by Jeon et al. in [27] which used the laser power, scanning speed, melt pool length and width, and measurements from a line scanner to predict the melt pool depth in real time. Where the melt pool length and width were extracted from a coaxial IR camera. When comparing the predictions to optical microscopy the mean absolute percent error (MAPE) was found to be 8.95%, showing the effectiveness of this algorithm. However, the line scanner was positioned 120 mm from the printing nozzle, which results in a time delay, making this technique unsuitable for real-time control. Another methodology implementing a 3D scanner for geometry control was shown in [28]. Where a 3D scanner created a point cloud to represent the geometry of the manufactured part, which was compared to the desired CAD model to quantify if there is significant distortion due to thermal effects.

ML has also been implemented in real-time monitoring of the size and shape of the melt pool and spatter by implementing segmentation [29]. Mi et al. trained a CNN that was capable of segmenting the melt pool and spatter from images captured during LDED. Moreover, their results show that the performance of their CNN method was not affected by the quality of images, camera size, and working distance.

There have also been cases of coaxial imaging being utilized for height measurements when augmented with ML [30]. In this work by Kim et al., a coaxial IR camera was used to capture the temperature distribution of the HAZ in real time. Thermal dynamics, namely the heating rate, cooling rate, and maximum temperature were extracted from the IR images. The thermal dynamics and process

parameters (laser power, scanning speed, powder feed rate, accumulated height, melt pool width, melt pool length) were then used to create a NN to predict the height at each timestep. Once trained, the NN was able to predict the height with a MAPE of 12.62%. This NN utilized images to extract features for geometry prediction but did not use the images directly as input features for the NN to predict the clad height.

Li et al. described a technique to control part geometry during DED by adjusting the powder flow rate to maintain constant melt pool energy [31]. Due to heat accumulation in thermal processes, melt pool energy does not remain constant, which typically results in geometric distortion. Usually, the energy input is decreased to compensate for the heat accumulation but by altering the powder flow rate instead Li et al. were able to maintain geometry while increasing the productivity of the DED process. Moreover, this work showed that the thin-walled clad produced with feed rate-based control had dimensions closer to the desired part than the thin-walled clad produced with laser power control.

2.1.2 Monitoring Solidified Geometry

Alternatively, some approaches utilize monitoring the solidified deposition to determine its geometry. Such as the method devised by Davis and Shin to measure the clad height in real-time by using a line laser and charge-coupled device (CCD) Camera [32]. The line laser was mounted 130 mm above the clad and the camera was mounted behind (in the direction of clad motion) the line laser and at an angle of 55° from the light plane. The camera would be able to capture the location of the line laser on the clad in real-time and use the known angle and distance of the camera to determine the clad height. However, measuring directly over the melt pool with this method is unfeasible since the light radiating from the molten metal would interfere. Therefore, the line laser was displaced 5 mm behind the melt pool to avoid image noise. This introduces a signal delay of $5/v$ (s) where v is the scanning speed (mm/s), which negatively impacts the ability to control LAM with this monitoring system.

A unique method developed by Donadello et al. measures the height of the clad by using triangulation [10]. A custom unit was designed and mounted to the deposition head which featured a CCD camera and a second laser, referred to as the probe laser. The probe laser has a wavelength of 532 nm and passes through a series of lenses and onto the clad. The lenses bend the light from the laser such that the probe laser is not perpendicular to the substrate, therefore the location of the probe laser changes with height. The CCD camera has a bandpass filter which only allows the same wavelength of the probe

laser to be visible and therefore, by detecting the location of the probe laser on the camera the height can be calculated in real-time.

A novel sensor setup was discussed in [33], in which a welding camera is utilized to measure track width and an in-process depth meter is used for height measurements. These measurements are then integrated into a controller to simultaneously control the laser power and scanning speed based on the height and width measurements. The uniqueness of this method was utilizing melt pool monitoring for width measurements and the solidified region for height measurements.

Therefore, tools exist to monitor the geometry, usually the height and width of the clad, in real-time. However, existing tools are often limited in their performance since the geometry cannot be measured directly from the melt pool, it is often predicted. While the geometry can be measured after the deposition has solidified, this results in a delayed data acquisition. Moreover, these existing techniques often use process parameters, such as the laser power and scanning speed in their calculations, which may make these algorithms less applicable when working with other materials or thermal processing machines.

2.2 Microstructure and Material Properties in Thermal Processes

Process parameters influence the microstructure during thermal processes, as shown in [34], meaning that in-situ microstructure monitoring is necessary. Zhao et al. utilized high speed X-ray imaging to monitor the powder bed fusion (PBF) process in real-time from a lateral perspective, in the plane of the powder bed [24]. Images were captured at a frame rate of 50kHz, allowing for large amounts of data to be measured in real-time. Since the solidification in PBF is highly localized and extremely fast, a high frame rate camera is ideal for monitoring the microstructure. Applying image processing to the X-ray images captures allows for the solidification front to be outlined, as well as the instantaneous solidification direction. Finally, the phase transformation is also probed by the high-speed X-ray diffraction technique. Since the solidification rate and phase transformations can be monitored in real-time with this high-speed X-ray it can estimate the microstructure of the final PBF produced part. Some understanding of PBF is necessary since other thermal processes work with similar materials and temperatures; hence, sensors used in PBF may be applicable to other thermal processes. Another way that X-rays are used to monitor the microstructure in thermal processing is with spatially resolved X-ray diffraction [35]. Titanium fusion welds were selected as a case study to use spatially resolved X-ray diffraction to map the material phases and their solid-state transformations during the welding

process. Though the material phase is monitored in real-time, the measurements are only taken over a narrow area, meaning the material properties of the entire melt pool cannot be measured. The cost of X-ray imaging is also prohibitive which is a limiting factor in using X-ray imaging more widely in thermal process monitoring.

Although X-ray imaging enables the direct monitoring of microstructure, the temperature of the melt pool can also offer valuable insights into microstructure and material properties, as the final microstructure is primarily influenced by the thermal dynamics (peak temperature, heating rate, cooling rate, and solidification time) of the HAZ. The correlation between high temperatures, like those seen in thermal processes, and microstructure are well known [36]. Therefore, understanding the thermal dynamics can be used to predict the microstructure of the thermal process part in real-time. Thermal dynamics have also been shown to change with process parameters [37], which further supports the use of thermal dynamics to infer microstructure.

2.2.1 Inferring Microstructure and Material Properties in Thermal Processes

Material properties are among the most important outputs of thermal processing since it determines the strength and quality of the final part. The microstructure provides a strong indication of the underlying material properties; therefore, monitoring and control of microstructure is sufficient to estimate material properties in many cases. There are various ways to monitor the material properties of a part during thermal processes, which are explored in this section.

Since temperature is the main influencing factor in the formation of phase precipitation during DED [38], the cooling rate of the melt pool is strongly correlated to the microstructure of parts produced with thermal processes [39]. During thermal processes, variation in build geometry and heat accumulation can alter the melt-pool temperature, geometry, and layer height, which directly influences the quality of the produced parts in terms of dimensional accuracy, microstructure, properties, and defects [40]. Moreover, the complex thermal history of thermal processes that defines the incident energy and the geometry of the melt pool, is directly affected by the interaction among process parameters. Accordingly, this complex thermal history results in different microstructures and consequently, mechanical characteristics because the thermal dynamics lead to the generation of complex hydrodynamic fluid flows which influences the crystal growth, orientation, microstructural defects and finally melted particles [41].

To monitor thermal dynamics with a non-contact sensor, calibrated IR imaging or pyrometers are often used, which estimate the temperature based on light emitted from the melt pool. This was demonstrated by Muvvala et al. where the temperature cycle of the melt pool was monitored with a pyrometer [42, 43]. Thermal dynamics such as the heating rate, peak temperature, and cooling rate were extracted from this data and through testing the authors were able to estimate the microstructure based on these parameters. Cooling rate is shown to influence the microstructure of several materials in LMP such as Inconel powder [42, 43], and 316L stainless steel [44]; therefore, the cooling rate will also likely affect the microstructure of other metals. Figure 2-4 shows that as the cooling rate decreases the microstructure of Inconel 718 transforms from fully dendritic structure with small traces of equiaxed grains into complete stray grains near the surface.

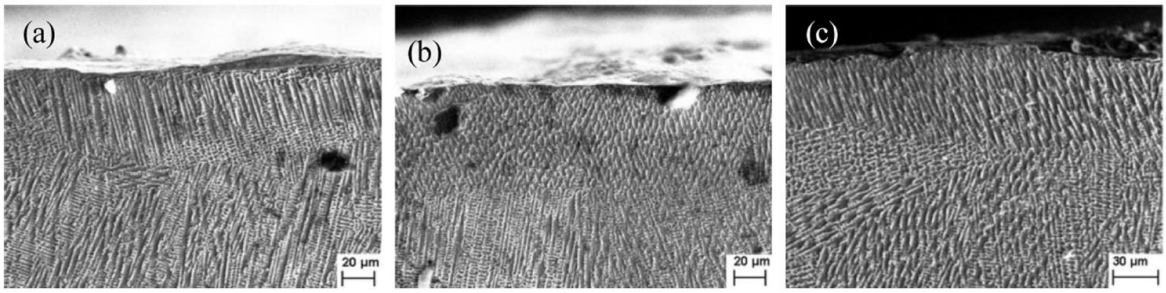

Figure 2-4 Effect of cooling rate on stray grains layer thickness (a) 680 °C/s, (b) 430 °C/s and (c) 260 °C/s corresponding to scan speeds of 1000, 800, and 600 mm/min respectively, (P = 1200W, pre-placed layer thickness = 2 mm) [43].

Measuring the cooling rate can be done with an IR camera, such as by Marshall et al. [45], where an IR camera monitors the melt pool in real-time. To gather more accurate measurements the IR camera was also calibrated with a pyrometer for high temperature measurements and a thermocouple for low temperatures. The authors determined that it is possible to determine a macroscale grain morphology by comparing the local temperature gradient at the solidus isotherm and the solidification speed to the solidification map compiled by Kobryn and Semiatin [46]. In recent work [47], the effects of thermal dynamics were compared to the formation of martensite, with hardness used to estimate the material phase. It was shown that analysis of the cooling rate alone may not be sufficient in predicting the microstructure because of the phase transformations while the melt pool is heating and the melt pool's peak temperature. Therefore, to have a more accurate estimate of the final microstructure an IR camera can be implemented to monitor all the relevant thermal dynamics: heating rate, peak temperature, and cooling rate.

A pyrometer in conjunction with thermocouples can be used to monitor the thermal cycles of the melt pool as shown by [48]. A pyrometer was used to monitor the melt pool during the entire test, while at two stages during the building of a wall, a thermocouple was positioned on the side surface of the uppermost deposited track, halfway along it. The thermocouples were used to measure the peak temperature without the error seen in the pyrometer due to the changing emissivity of the melt pool. Though the previous works featured a laser as the power source, using an IR camera to predict the microstructure can also been used for electron-beam processing [49]. Regardless of the power source, the microstructure can be predicted based on the temperature gradient and solidification rate. The literature reveals that in-situ monitoring the microstructure of thermal processes is commonly done based on the thermal dynamics [50, 51].

Though IR cameras are commonly used to measure the thermal dynamics, it is possible to supplement IR imaging with other information. Such as when Huang et al. [52] combined temperature monitoring data with temperature simulation and used thermal gradient and solidification rate to correlate product qualities. The results indicated that the dendrite arm spacing was more sensitive to scanning speed, and the cooling rate value had sufficient abilities to predict the microstructure when depositing 316L stainless steel and Inconel 625. Raplee et al. used an IR camera to monitor the thermal dynamics of the system; however, an algorithm was used to augment the raw data to improve the temperature measurements [53]. Their algorithm was inspired by the sudden change in emissivity that occurs upon melting, to correct for this the temperature of the melt pool was monitored to develop the thermal cycle of that location. From the thermal cycle it is possible to determine where melting occurs and where reheating from nearby melting occurs. This distinction allows for more accurate measurements of the thermal gradient which can be related to microstructure formation.

High-speed vision cameras are also capable of monitoring the material properties in real-time as shown by Mohanty and Mazumder [54]. Their technique enables in-situ monitoring of the solid/liquid interface due to the characteristic difference in reflectivity. Since the different phases are observable in the image data, it is possible to measure the solidification rate of the melt pool. The solidification rates that exist in LMP fall in the range between the rates found in conventional casting and in rapid solidification technology. Though there is no proper theoretical formalism to relate these solidification rates to material properties, further study may be possible to relate the solidification rate to the material properties of the part in real-time.

Parts produced in additive manufacturing (AM) are highly anisotropic in material microstructure and mechanical behavior due to the change of the local processing conditions in the build-up process [55]. Monitoring has been implemented in many AM processes to better understand the properties of the final product, thermal-based signatures particularly, have been adopted in many applications [56, 44]. Thermal dynamics (melt pool temperature gradient and cooling rates) have been shown to predict defect formation, microstructure evolution, and mechanical properties. Thus, measuring the temperature distribution of the heat affected zone (HAZ) can be used to predict many facets of the overall quality of the final product.

Titanium alloys such as Ti-6Al-4V are utilized in AM projects, due to their material properties regarding strength, weight, and ductility. However, the anisotropic material properties are inhibiting the widespread adoption of this material. Hence, a methodology is described in [55], where the process parameters are used with a thermal model to predict the solidification cooling rate of every node during the directed energy deposition (DED) build. Experimental validation was used to correlate the simulation-determined solidification cooling rate to the size, shape, and density of pores created during manufacturing. Therefore, this study has shown the relationship between porosity and cooling rate. Thermal modeling has also been demonstrated in [57], where rising temperatures in the substrate and the incident heat flux control material properties.

The correlation between thermal dynamics and material properties has been observed in other materials as well, such as in [58], where stainless steel 316L was studied. Where process parameters were linked to thermal characteristics, such as the thermal gradient, temperature, and cooling rate, and the corresponding microstructure was found. Additionally, this study explored Inconel 625 powder, where a similar correlation was found, where microstructure is related to thermal characteristics. Thermal dynamics have been shown to influence the microstructure of Inconel alloys, as shown in [59]. IR thermal images were used in this work to calculate the cooling rate, which was graphed against hardness measurements, demonstrating the correlation between these properties.

Heat dissipates from the melt pool into the bulk material and substrate, this rapid cooling allows parts to be manufactured during DED and determines the material properties. Conversely, monitoring the substrate temperature has some indication of the melt pool temperature, as shown by Guo et al. [60]. A thermocouple was fixed 2 mm below the substrate to continuously monitor its temperature while building a 50-layer thin-walled deposition with wire-arc additive manufacturing (WAAM). The

microstructure was analyzed throughout the specimen and the measured temperature to determine the final material properties.

2.2.2 Microstructure Control in Thermal Processes

Currently used techniques for controlling the microstructure in literature must be reviewed to demonstrate the need for real-time monitoring in thermal processes. During the DED process of Ti64 the deposition layer is formed as the melt pool solidifies. The β-grains precipitate from the liquid phase, grow epitaxially from the deposition due to the high temperature gradient and low solidification rate at the bottom of the melt pool. Only a part of equiaxed grains would form at the surface region of the melt pool due to the columnar to equiaxed transformation [61]. This mechanism of grain growth demonstrates how the thermal dynamics, particularly the cooling rate and solidification time determine the material properties of the final product in DED.

A unique technique for microstructure control in Ti64 was discussed in [61] where induction heating was used to control the temperature gradient of the melt pool. This allows for a larger material property control range than previously observed in DED; however, the inclusion of the induction coil may limit the geometry of parts that can be manufactured. Alternatively, changing the melt pool morphology, including its size, shape and solidification parameters at the liquid/solid interface influences the crystal growth in DED [62]. Shao et al. changed the power density of the laser by changing the laser power, spot diameter, and scanning speed for different labels and noting the different microstructures. Hence, a correlation was developed between the morphology of the melt pool, which is controlled by the power density of the laser, and the microstructure of the manufactured part.

Hence, measuring the temperature distribution of the HAZ is shown to be correlated to the material properties of the final deposition. However, different thermal dynamics can be extracted from the temperature distribution and correlated to the material properties and selecting the appropriate measurement tools appears to be a challenge in literature since different techniques exist. Options include X-ray imaging to capture the microstructure directly or estimating the temperature distribution with a pyrometer, IR camera, or thermal couples.

2.3 Temperature Measuring in Thermal Processes

Since the temperature distribution is closely related to the material properties, typically in the form of cooling rate or solidification time, the temperature distribution of the process must be known. The

temperature distribution can be measured from tools such as pyrometers or IR cameras, or estimated with predictions from other sensors, such as thermocouples and visible-light cameras. Numerically modelling the thermal properties of the HAZ has also been implemented in literature to estimate the temperature distribution.

2.3.1 Temperature Detection in Thermal Processes

Common techniques to measure temperature are to use a pyrometer to measure the temperature of a specific point [43] - [48] or a thermal camera to provide the full temperature distribution [49] - [52]. IR imaging is a common tool used to measure the temperature distribution in AM applications [56, 44, 2]. IR imaging is often preferred over pyrometer measurements since measuring the temperature distribution of the entire HAZ is desirable to determine thermal dynamics such as the peak temperature, heating rate, cooling rate, and thermal gradient. However, IR cameras can be expensive and offer limited optical customization, which motivates shifting to other temperature prediction tools.

Thermocouples can be used to augment thermal imaging data for improved temperature measurements. However, an alternative approach is to use only thermocouples to estimate the entire distribution since they are a more cost-effective sensor than IR cameras. Hu et al. has used thermocouples placed on the computer numerical control (CNC) table below the substrate to measure the temperature cycles of the melt pool based on the known material properties of the substrate and the distance between the thermocouple and laser center [63]. The clad-zone temperatures were between 1650 and 1800 °C with a wide range of process parameters and various clad materials, which agreed with optical pyrometer measurements.

2.3.2 Temperature Prediction in Thermal Processes

Thermal modelling and simulations have been used to predict the temperature distribution of AM where a finite element analysis (FEA) approach was shown to achieve a MAPE below 2.5% for predicting temperature profiles [64]. To improve the computational efficiency of this model, a machine learning (ML) algorithm was trained to predict nodal temperatures and was able to achieve a MAPE of less than 5%. Finite element models are capable of predicting the thermal distribution of the melt pool but are too computationally inefficient to use in real-time; hence ML is used to speed up the process [65]. Analytical models, based on thermal conductivity, have also been used to predict the temperature distribution based on the thermal properties of the material, and the energy added into the system [66].

Using an analytical model, the depth of the melt pool was calculated with less than 3.7% error when compared to experimental measurements.

FEA was also implemented with other thermal processes, such as a WAAM DED system, to simulate thermal and build time for residual stress analysis in [67]. In this study, two four-inch square tubes were deposited on a 6.35 mm build plate using the WAAM process. The FEA model was developed using temperatures from the first sample to calibrate the boundary conditions with an average deviation of 8.9% and the second sample temperatures verified the model with an average deviation of 12%. Hence, it was shown that FEA modelling can be used to predict the temperatures of the melt pool during DED processes. FEA simulation was also implemented in [68], which demonstrated the integration of FEA simulation with PI control. In this work, the desired melt pool size was input to a PI controller, which calculated the corrected laser power and fed that result into FEA simulation to determine the updated melt pool size. The resulting variable laser power profile obtained from the simulation is implemented during the DED experiment. This allowed Liao et al. to control the depth of the melt pool, which is correlated to the temperature distribution of the HAZ, since it cannot be directly monitored. This methodology was shown to control the material properties at different locations of a single part but relies entirely on simulation measurements and is unable to correct process disturbances. Therefore, FEA has been shown to be sufficient at modelling the temperature of the HAZ during thermal processes to predict the microstructure of produced parts [69, 70, 71].

However, FEA models are often computationally expensive, which limits its potential to be used in real-time monitoring. Therefore, ML techniques have been implemented to improve the efficiency of temperature simulations in DED [72]. The ML algorithm used the input features: x-y coordinates, time step, the laser position, and the distance between laser head and each point P (x, y) at each time step. Using these features a NN was created to predict the temperature evolution of the melt pool in DED of 316L stainless steel with an accuracy of 99% when compared to the FEA model.

Another approach to circumvent the use of expensive thermal imaging is the use of a simple mathematical model of the process to estimate the temperature distribution. Kumar utilized mathematical formulae for heat conduction to derive and solve equations for the thermal dynamics in a solid work piece during laser welding [73]. The formulae were able to solve for the temperature distribution, peak temperature, cooling rate, and thermal cycles, using only assumptions made to the heat source and materials. The analytical model was found to be capable of predicting results of any

solid material in laser welding but was limited to scenarios where there was no melting. Farahmand and Kovacevic used a combination of a thermal and mechanical finite element model for laser cladding by a high-power direct diode laser [74]. The numerical model was able to calculate the thermal gradient and comparing the results to experimental data reveals a maximum predicted error of 3.5%. Though, the performance is quite good, this kind of model is too computationally demanding to be used in real-time. Thermal modelling has also been used to predict temperature of the process for future states for control purposes [75]. Though this model was used with real-time measurements, the basics may be used for temperature estimation as well.

Temperatures have also been predicted using vision cameras, which are typically less expensive than thermal cameras and have other benefits such as higher framerate and/or resolution as well. Devesse et al. used a hyperspectral line camera with a spectral response from 400 nm to 950 nm [76]. The camera can capture a line of pixels at the center of the HAZ perpendicular to the scanning direction of the laser. Though the spectral response is not in the IR range, using Planck's law and estimated emissivity values, the temperature of these pixels can be calculated from the intensity captured by the camera. This method is capable of clearly detecting the melt pool boundary, however, there is an uncertainty of 10% associated with the temperature calculation. Lu et al. were able to use the same principles to calibrate a vision camera, with spectral response from 300nm to 1050nm, to estimate the temperature of the camera's field of view [77]. Though the error of temperature prediction with this method is within 3%, this was not used with thermal processes. Gobbi proposed a method to use two CCD cameras to create a low-cost thermal imaging system for welding applications [78]. However, this method was only able to accurately measure a maximum temperature range of 640°C - 825°C, which is not suitable for LMP applications.

ML has also been implemented to predict temperature distribution and history of the melt pool during DED in [79]. Zhang et al. developed two ML predictive models, one using extreme gradient boosting and the other using long short-term memory (LSTM). Twenty-five experiments were conducted with a combination of different laser powers and scanning speeds to create the training and test sets for the ML models. The input variables for the prediction were: laser power, scanning speed, layer index, time index, average height, and average width. These parameters allowed for the temperature to be predicted with a relative error of less than 3.7% for the extreme gradient boosting model and less than 3.4% for the LSTM model. It was also found in this work that the extreme gradient boosting model was 400 times faster to compute the temperature than the LSTM model.

Another implementation of ML to predict temperature of the melt pool was demonstrated in [80], where Xie et al. created a NN that was able to predict temperatures with a mean relative error of 4.83%. The loss function of the NN was augmented with the generalized heat conduction equation to account for the underlying physics of heat transfer in the DED process. Moreover, Xie et al. showed that the addition of physics-based boundary conditions allows the network to be trained with a smaller dataset. Ultimately, this NN was able to predict the temperature of the HAZ during DED by using the laser power, scanning speed, time, and spatial coordinates (x, y, and z) as inputs with an accuracy over 90%. Figure 2-5 shows the architecture of the NN which uses the previously mentioned process parameters to estimate the 3-dimensional temperature field, labelled L (W, b).

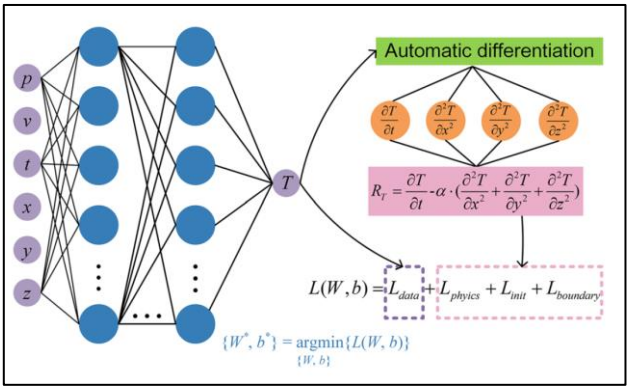

Figure 2-5 Schematic diagram of the NN model for predicting the temperature with physics-based boundary condition [80]

2.3.3 Temperature Control in Thermal Processes

Since control is one of the main motivations towards having accurate real-time monitoring of thermal processes, it is necessary to explore the state of temperature control of thermal processes in literature. An example of thermal dynamics control was demonstrated by Bennett et al. while using Inconel 718 [81]. An IR camera was used to monitor a powder fed LDED process and recorded the process with emission of temperatures ranging from 300 ºC to 2,000 ºC to calculate the cooling rate. Images of the microstructure were then captured at nine locations of a thin-walled test specimen with optical microscopy to verify the influence of cooling rate on the tensile strength of laser deposited Inconel 718.

Real time monitoring of thermal dynamics has been used in various materials such as during solidification of aluminum [82]. Hagenlocher et al. devised a methodology where isotherms extracted from images captured with an IR camera are used to determine the local solidification rates. This work

showed the highest temperature gradients and solidification rates in the case of high process velocities, demonstrated the relationship between process parameters and thermal dynamics.

A technique was outlined in [83] where two photodiodes observed the melt pool at different wavelengths to estimate the temperature without accounting for emissivity adjustments. The setup developed by Jeong et al. was able to monitor the temperatures with a frequency of 100kHz, within ranges that are supported by literature, but measures the average temperature over the FOV. The developed method was able to measure solidification cooling rates above 5000 °C/s.

In [84] it was shown that thermal dynamics are correlated to the microstructure and material properties of 316L stainless steel in DED. Moreover, using a PID controller to adjust the scanning speed to keep a constant cooling rate resulted in more consistent properties throughout multi-layer samples, when compared to open loop samples.

Since material properties and microstructure of parts manufactured with thermal processes are desired features to monitor and control, temperature measurements are often used to infer these properties. However, temperature measurements often offer limited data in the case of pyrometers or have prohibitive costs in the case of thermal cameras. Modelling techniques can be implemented as well, but assumptions are made in favor of computability which reduces the accuracy of these models. Therefore, there is a desire in literature for cost-effective methods for temperature measurements with reduced computational time and error.

2.4 Real-Time Quality Monitoring

AM is shown to have a high rejection rate, which indicates that between 5% and 50% of parts are rejected [85]. The high rejection rate is because AM parts are known to vary significantly in quality which is the result of many process parameters and environmental conditions [86]. Monitoring the process in real-time may provide more information to predict the quality of the part during manufacturing. In process quality prediction would allow for fatal errors to be detected immediately and the process can be forced to stop. Moreover, effective evaluation of quality in real-time can also be used instead of part validation at a later point of the manufacturing process, which would improve the efficiency of AM.

During laser cladding remanufacturing (LCR), which is a process used to repair damaged metal components, low quality of repair layers is noted as a main challenge. Liu et al. demonstrated the

effectiveness of using different sensors to monitor the LCR process to provide enough information to improve the quality of repair layers [51]. The review paper highlights the possibility of using visual information, temperature information, spectral information, or acoustic signals to monitor the quality of repair layers. Liu et al. concluded that currently these sensors are not capable of directly monitoring quality; however, the potential has been shown for this sensor data to be augmented with machine learning (ML) techniques to indirectly monitor and control quality.

Another measurement technique is to use audio signals to monitor the quality during thermal processes and welding processes, since sudden acoustic changes may correspond to sudden changes to the weld or melt pool's properties, which may indicate poor quality. Audio signals can be in the form of acoustic emissions which are monitored by a piezoelectric transducer coupled to the workpiece or via audible sound, which can be measured with a microphone in the vicinity of the melt pool [87]. Both forms of measuring audio signals have been shown to detect defects and predict quality in laser welding, with the main drawback of acoustic emissions being the need to be in contact with the workpiece and the main drawback of audible sound is collecting background noise. The performance of both these audio signals can be improved for thermal process monitoring with the addition of ML. To improve the quality prediction of arc welding, Sumesh et al. trained a random forest to classify the quality of welds [88]. Their random forest was able to classify the welds with an accuracy of 88.69%, which the authors claim suggests that this can be used for quality monitoring in real-time. Shevchick et al. was similarly able to improve the performance of monitoring acoustic emissions during SLM to classify parts with an accuracy between 83 – 89% [89].

An alternative method that has been used in hot-wire cladding is to monitor the electron temperature, which can be correlated to the stability of the process [90]. During the wire fed DED cladding process, S. Liu et al. used a CCD camera to monitor the deposition process and an Ocean Optics spectrometer to detect the emission signal of the plasma over the melt pool. It was found that the standard deviation of the plasma's electron temperature, which was found by analyzing the incoming signal from the spectrometer, was an indicator of the instability of the cladding process. Since process stability is correlated to quality, this is an effective technique to monitor quality during cladding of Inconel 625.

2.4.1 Real-Time Defect Monitoring

Defects, such as voids, cracks, cavities, lack of connection or foreign material inclusions, lead to the weakening of manufactured parts and compromise the repeatability and precision of the manufacturing

process. Monitoring defects in AM can be accomplished through photoacoustic (PA) imaging, which is a low-cost sensing technique that can be easily implemented to the original AM system [91]. To add PA imaging to the system, a microphone was set near the manufactured part and connected to the control computer. The PA signal generated during the laser sintering process is then captured by the microphone to provide in-situ data. In theory, if the property of the laser heated material changes the peak pressure will change, allowing the microphone to record a different volume. This was done with ceramic AM for defect detection, though the same principles may work in metal based thermal processes as well. Alternatively, acoustic signals have been used for online monitoring of short circuit gas metal arc welding [92]. The experimental setup featured a piezoelectric sensor fixed to the welding specimen to monitor the acoustic signal during welding. All discrepancies which have a dramatic influence on the quality of the weld, such as burn-through or extinguishing of the arc are clearly monitored by acoustic signals. It was found that sudden changes in the microphone signal waveform result from process errors, like those mentioned above.

In IR imaging the incoming images suffer from large data volume and low signal-to-noise ratio. To account for these issues, Kahanzadeh et al. used multilinear principal component analysis (MPCA) to reduce the size of the incoming data [93]. The implementation of MPCA reduced the feature space and allowed for more efficient computation due to the smaller dataset. It is then easier to detect anomalies in the reduced data, which can be an indication of defects such as porosity and mini cracks. IR imaging can be used to monitor defects during welding as well, as shown by Sreedhar et al. [94]. In their research, IR images were captured while TIG welding the shell of a propellant tank. Defects were detected via their thermal contrasts in the solidified weld region close to, but not colinear to, the weld pool. It has also been shown that simply controlling the thermal dynamics of the system can be used to prevent the formation of defects [95]. Hassler et al. also demonstrated the effectiveness of using IR thermography to monitor the formation of defects during LAM [96]. They noted that though defects are visible through their different emissivity value, the defects are only visible for a few milliseconds.

Though some researchers have explored the use of optical data or acoustic data for defect detection, it is possible to use both sensor types for more incoming information. Ma et al. proposed this detection setup, which features an acoustic collector positioned above the melt pool and an off-axis optical collector [97]. This monitoring system was used with laser welding and wire arc additive manufacturing. It was found that since the amplitude of the ultrasonic signals in the defect zone were lower than those in the normal zone, defects can be detected. The optical data was more suitable in

predicting defects due to changes of elements in the manufacturing process, while acoustic signals are more appropriate for in-situ monitoring of the stability of the arc.

2.4.2 Porosity Monitoring

Porosity is a specific subset of defects, and another unintended result of some thermal processes that reduces the quality of fabricated parts and must be considered. Producing fully-dense parts is an ongoing challenge in AM, which justifies exploring porosity detection more thoroughly than other defects. Imani et al. used a DSLR camera positioned above the plane of the powder bed to monitor porosity during PBF [98]. Understanding which sensors are used in PBF is critical in DED as well since these processes use similar materials and temperature, and therefore, sensing technology may be applicable to both. Images are taken between each layer of the process to detect process drifts in the early layers. Image processing allows the images to be converted into a feature space which allows for ML to be used to estimate the porosity of the part. The porosity of test samples was measured offline using computerized tomography (CT) scanning to create a dataset for the ML algorithm. This method of PBF monitoring can classify parts as defective with up to an 89.36% accuracy. Since the porosity is only measured between every layer and not in real-time this method has limitations in being implemented with control and quality assurance. A similar approach was taken by Zhang et al. in [99], where a coaxial monochrome camera was used to capture images at 395 frames per second during laser welding. To label the collected images with the correct porosity, an optical microscope was used to observe the pores exposed on the cross section and image processing was used to extract the porosity. A CNN was then trained to use the raw images as input and classify whether there is the presence of a pore in that image. Their CNN reported an accuracy of 96.1% in lap laser welding of 6061 Aluminum alloy, but pores less than 150μm were difficult to detect. Another experiment by Zhang et al. featured the same methodology with Titanium powder and the porosity was detected with an accuracy of 91.2%, further demonstrating the capability of deep learning in porosity measurements [100].

DMP Meltpool is a commercially available monitoring system which consists of two photodiodes installed on either side of the build chamber of a PBF system [101]. Coeck et al. were able to use the DMP Meltpool monitor system to achieve 92.3% detection efficiency for all lack of fusion pores after applying false positive reduction [102]. DMP Meltpool measures the intensity of the melt pool, not necessarily the shape or temperature, which reduces the capabilities of this monitoring. However, it has

been found that sudden changes in intensity may be caused by defects; therefore, monitoring and controlling the intensity can predict the defects in the part.

2.5 Summary

Real time monitoring of thermal processes with image-based sensing is commonly used in research and literature to help solve the repeatability and stability problems of the metal AM process [103]. Imaging is often implemented as it offers a noncontact solution with a range of available sensors and image processing can improve quality. Moreover, many tools exist for image processing which can be utilized to extract key information from images capture while monitoring thermal processes.

For real-time geometry measurements in thermal processes, most often a visible-light camera is used to measure the melt pool. However, the placement of the camera is crucial in determining which feature can be measured; for example, if the viewing angle of the camera is coaxial to the laser, it can only measure the width. The viewing angle may also be affected by the addition of an IR camera if the same viewing angle is optimal for both cameras, it may not be possible to install both onto a system. This results in the desire in the industry to have a sensor capable of measuring both the width and height of the clad in real-time without sacrificing the placement of the thermal camera.

Microstructure is another critical feature to monitor during thermal processes, which is typically accomplished by measuring the real-time thermal dynamics of the HAZ and inferred from known correlations based on phase transformation theory. Thermal dynamics such as cooling rate, solidification time, and peak temperature can be calculated from the thermal distribution captured by an IR camera. These properties are correlated to the microstructure, allowing the material properties to be predicted if thermal dynamics are monitored in real-time.

Vision and IR imaging has also been utilized with ML to monitor features that cannot be extracted solely from image processing. Both types of sensors have been used in conjunction with ML to monitor porosity and defects very effectively in real-time. Acoustic sensing and spectroscopy have also been able to predict the quality of thermal processing, though spectroscopy has been shown to have other uses as well in monitoring the composition of the HAZ.

Multi-sensor setups are used for in-situ monitoring of multiple parameters, such as a profilometer for geometry measurements and IR camera for microstructure monitoring used in [104]. The most critical properties monitored during thermal processing are geometry, microstructure, defect detection, and

porosity, since these properties are all directly related to the quality of the final produced part. Reviewing existing tools used in literature reveals that a limitation of current systems is in monitoring either geometry or thermal dynamics. A single tool capable of monitoring multiple features simultaneously is missing in literature and industry, typically multiple sensors are fitted to perform the desired measurements and calculations independently. Additionally, current tools are often limited to monitoring one thermal process.

Therefore, a generic monitoring system, for multiple thermal processes, must be capable of measuring relevant geometric and temperature data in real-time. This speculative monitoring system can be designed to use a vision camera to monitor the geometry of the melt pool and an IR camera to measure the thermal dynamics for predicting the microstructure. Furthermore, the combined sensor can be used to capture data to correlate visible-light and temperature data to create a temperature prediction model with only a vision camera, which would significantly reduce the cost of temperature measurements. Finally, the potential exists for monitoring defects and porosity with information from both cameras augmented with ML.

Chapter 3
Thermal Processing Real-Time Monitoring Apparatus

The development and validation of a real-time monitoring apparatus is detailed in this chapter. The design requirements are determined based on the parameters of similar systems and considerations of the processes. Such as the materials used in thermal processes and their respective temperatures. The presence of hazards must be considered in the design of the monitoring apparatus as well, such as spatter and powder. The chapter includes descriptions of the thermal processes used to validate the monitoring system. Validation was primarily conducted with the LMP system integrated at the Automated Laser Fabrication (ALFa) laboratory at the University of Waterloo. Further testing was conducted at the Centre for Advanced Material Joining (CAMJ) at the University of Waterloo to demonstrate the robustness of the monitoring apparatus. Challenges encountered during the design process are outlined at the conclusion of this chapter, including an explanation and solution for anomalies that were experienced.

3.1 Development and Design of Monitoring System

To monitor the key features of thermal processes, an appropriate camera was created with off-the-shelf components based on the size and temperature of the HAZ. As mentioned in Chapter 2, there are many sensors currently implemented in thermal processes to monitor key components. However, image-based sensing was found to be the most versatile for this branch of manufacturing, usually in the form of visible light, IR light, or x-rays. Imaging provides a non-contact means for monitoring the process, which allows the system to capture data without influencing the process. The imaging sensor can also be placed such that its relative position to the HAZ is constant at all times during the process. Imaging has been shown to effectively monitor the geometry of thermal processes and thermal imaging can be used to calculate thermal dynamics (peak temperature, heating rate, cooling rate, and solidification time), which is related to the material properties. Finally, imaging has also been used to detect porosity and other defects (voids, cracks, etc.) during AM showing that it can be used for a wide array of key features.

3.1.1 Monitoring System Design Requirements

The design requirements are guidelines used to define the scope of the monitoring system and outline the features that would characterize a feasible solution. The first consideration for designing the

monitoring system is the features to be measured in real-time. The geometry of the melt pool and material properties of the deposition have the largest influence on the quality of the manufactured part; therefore, these measurements must be known. Imaging can measure the geometry directly, and by monitoring the previously mentioned thermal dynamics, the material properties can be inferred from real-time measurements.

The selection of sensors is motivated by the required measurements, especially pertaining to the material properties and geometry. In the case where multiple sensors were found to offer suitable performance, the more cost-effective option was selected. While imaging is an effective tool in monitoring thermal processes, there are limitations due to the cost of the equipment and the availability of compatible parts. Sensors and optics in the visible spectrum tend to be the most cost-effective and have the most diverse parts due to the popularity. Moreover, these sensors typically have higher resolution and framerate compared to other wavelengths and more image capturing parameters, allowing for user defined settings to optimize captured images. These benefits make vision sensors preferred over x-ray imaging. However, the capability of temperature monitoring makes IR imaging an appealing consideration as well. Therefore, implementing both vision and IR imaging would be an effective, low-cost, array of sensors for thermal process monitoring. Though IR sensors are typically expensive, utilizing visible-light images to supplement the IR images allows for a more cost-effective selection of the IR sensor.

The high temperatures in thermal processes would also influence the choice of IR sensor, the HAZ of metals is typically hot enough to radiate in visible light, as explained through Planck's law; therefore, thermal monitoring can be achieved by a near-infrared (NIR) or short-wavelength infrared (SWIR) sensor [75]. Some visible light optics are also capable of working within the NIR and SWIR wavelengths, further reducing the cost of the monitoring system. Therefore, the monitoring system must include both a visible light sensor for high resolution geometry measurements and a NIR or SWIR sensor to measure the temperature distribution.

The monitoring system will be designed such that it is capable of monitoring with both a coaxial and lateral field of view (FOV), as these setups offer different performance. Positioning an IR camera to have a view that is coaxial to the laser allows the entire temperature distribution of the melt pool to be monitored. However, a lateral field of view is more effective for geometry measurements as the height cannot be determined from coaxial images. Hence, the flexibility to use both optical setups allows the

monitoring system to be used in the most optimal position for the thermal process being monitored. Moreover, the size of the HAZ must be accounted for as well since the entire HAZ should be within the FOV, without having an unreasonable resolution. The requirements are summarized as:

- Dual camera sensors with a similar FOV, one in the visible light spectrum and the other in either the NIR or SWIR spectrum.
- FOV should be between 5 mm × 5 mm and 100 mm × 100 mm to observe the entire melt pool and have the HAZ covered by enough pixels.
- Framerate of at least 10Hz for performance comparable other real-time monitoring in research [13, 47].
- To guarantee the compactness of the design the volume should be less than 1600 cm^3 which is approximately the combined volume of the previously used thermal and vision cameras at the ALFa laboratory in the University of Waterloo.
- Temperature range of 700°C – 1500°C to cover the phase changes of stainless steel [105] which is a commonly used material in LDED.

3.1.2 Monitoring System Alternative Designs

Using the above requirements, the proposed design was decided to feature a NIR sensor to capture the thermal dynamics (peak temperature, heating rate, and cooling rate of the HAZ). Additionally, a vision sensor for higher resolution geometry measurements of the melt pool. The Optris 08M was selected and the NIR sensor, which features narrow spectral response at 800nm resulting in a calibrated temperature range of 600°C – 1900°C [106]. The selected vision camera is the Photonfocus D1312, which is an HDR camera featuring a CMOS sensor [107]. However, the sensors needed to be arranged in an optimal fashion, to minimize the size of the housing and to ensure that the HAZ is in the FOV for both sensors during all possible thermal processes. Figure 3-1 shows the different enclosure designs featuring both sensors with specialized optics. Note that both designs (b) and (c) feature a cold mirror (dichroic filter) to allow for reflection and transmission into the desired sensors.

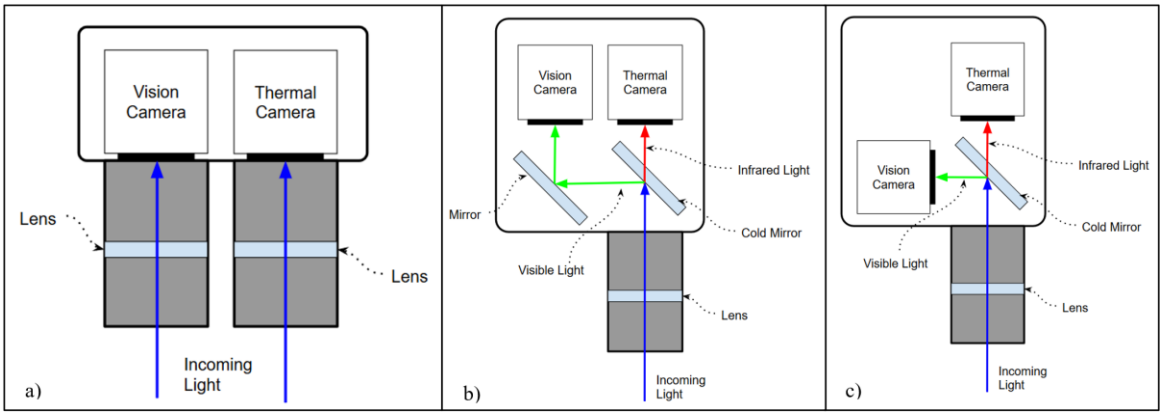

Figure 3-1 Conceptual designs for monitoring system featuring a) binocular cameras b) parallel cameras c) perpendicular cameras

The binocular arrangement shown in Figure 3-1a allows both camera sensors to have a specialized optical setup. Having the optics selected for each camera allows for the lenses to be selected for the specific sensor and therefore provide the ideal images. This also creates the most compact monitoring system since the enclosure only needs to fit the cameras themselves with no additional optical components.

However, to accommodate for the distance between the different lenses for each sensor, the FOV would need to be wider, which reduces the number of pixels that the HAZ occupies in the image. Alternatively, the lenses could be angled inward to ensure the HAZ in a similar location in each image, but this would result in a fixed working distance. Moreover, in this case the images would be distorted relative to one another.

To correct the different FOV, a single lens could be used with a beam splitter and series of mirrors to ensure light from the same source enters both sensors, which is featured in Figure 3-1b. Positioning both cameras at the back of the enclosure also allows for the connections to be accessed easily and since both cameras have the same orientation the images will be oriented in the same way as well. The reflected visible light from the cold mirror is reflected twice before entering the vision camera resulting in a properly aligned image.

Unfortunately, using one lens for both sensors limits the selection of lenses and sensors since the spectral response of all components must be compatible. Moreover, the focal length, which is the distance between the sensor and the lens, is different for each sensor in this arrangement, which means that both images cannot be in focus at the same time. An additional lens would need to be added to alter

the incoming rays of light to correct for the different focal length, which would result in visual deviations between the images.

The removal of the second mirror corrects the different focal lengths but the images in the vision camera will be reflected, which can be corrected with image processing. The main drawbacks of this design are that the connections for the vision camera, which are on the rear of the camera, must be considered, and the wasted space in the housing. The selection of the vision camera or manipulating the hardware may accommodate these drawbacks. This final design, with the optical optics is shown in Figure 3-1c.

3.1.3 Monitoring System Final Design

Based on the requirements and comparing the alternative designs the most optimal monitoring system was found to the perpendicular camera arrangement shown in Figure 3-1c. Using this framework, the CAD model and prototype shown in Figure 3-2 below were developed. The final design is referred to as the monitoring optimization and control (MOC) sensor because of its current and proposed future capabilities.

Figure 3-2 a) Final MOC sensor CAD model b) MOC sensor prototype c) Prototype mounted in the ALFa Laboratory

It is shown in Figure 3-2a that the electronics of the vision camera were split into two components, this allows for the design to remain compact and keeps all the connections at the back of the housing, addressing the concerns with this camera arrangement. Table 3-1 indicates sensor specifications of the MOC sensor; demonstrating that it has the foundation to be an effective tool for monitoring thermal processes.

Table 3-1 MOC Sensor specifications

Objective	Actual
FOV size	35mm × 35mm
Framerate	77Hz
Volume	1220cm^3
Temperature range	600°C – 1900°C

3.1.4 Optical Components

To select optical components, the working distance, object size, image distance, and wavelengths of light must be considered. The intent of this camera is to monitor thermal processes with an off-axis FOV, to allow for temperature and geometry measurements, though other FOVs are possible with different optics. The working distance was set to be from 250mm – 350mm since at this distance the monitoring system is far enough away from the HAZ that it will not be damaged by heat, powder, spatter, or other hazards, while not being too far that the image will be distorted or that the position of the MOC sensor may interfere with other process equipment. The object size refers to the size of the HAZ, which typically has a diameter of approximately 10mm, depending on the process. The image distance is the distance between the camera sensor and the lens, which must be positioned to produce focused images. These parameters were considered to select a lens with the optimal focal length for clear images. Finally, the wavelengths of light are determined by the camera sensors, which are 780nm – 820nm for the IR sensor [106] and 400nm – 900nm for the vision sensor [107]. The spectral responses of the sensors must be considered as well to ensure the light can pass through the necessary components and since different wavelengths of light correspond to different focal lengths. These constraints motivated the decision for the optical components highlighted below in Table 3-2.

Table 3-2 Optical Components Bill of Materials

Part	Substrate	Focal Length	Reflected Light	Transmitted Light	Quantity
Achromatic Lens	N-BK7/N-SF5	175mm	-	400nm – 1000nm	2
Cold Mirror	Borofloat	-	400nm – 690nm	750nm – 1200nm	1

As indicated in Table 3-2, the cold mirror reflects visible light and allows IR light to be transmitted through. Though a specially designed imaging lens is ideal for using with a camera, since the hardware is a custom design, a different approach was necessary. Using 2 achromatic lenses (which are simply labelled “lens” in Figure 3-1c) is a low-cost imaging option with minimal distortion while capturing images [108]. Finally, with the optical components selected, their performance can be modelled with light approximation software to position the sensors within the enclosure to ensure the images are in focus for each sensor at all working distances.

Finally, it should be noted that since the IR camera features an 800nm narrow bandpass filter and is calibrated specifically to be used with metals in laser applications. However, since the vision camera is not designed for this specific use case, the captured images will become saturated if used directly for monitoring. Therefore, MidOpt ND60 and ND120 filters are added between the cold mirror and vision sensor to result in approximately 1.56% transmission within the spectral range of the vision camera [109].

3.2 Laser Materials Processing Experimental Setup

Once the MOC sensor was developed for monitoring thermal processes, initial testing was conducted with LMP. Figure 3-3 below illustrates the experimental setup of the LMP system in the ALFa laboratory used to validate this research as a schematic diagram.

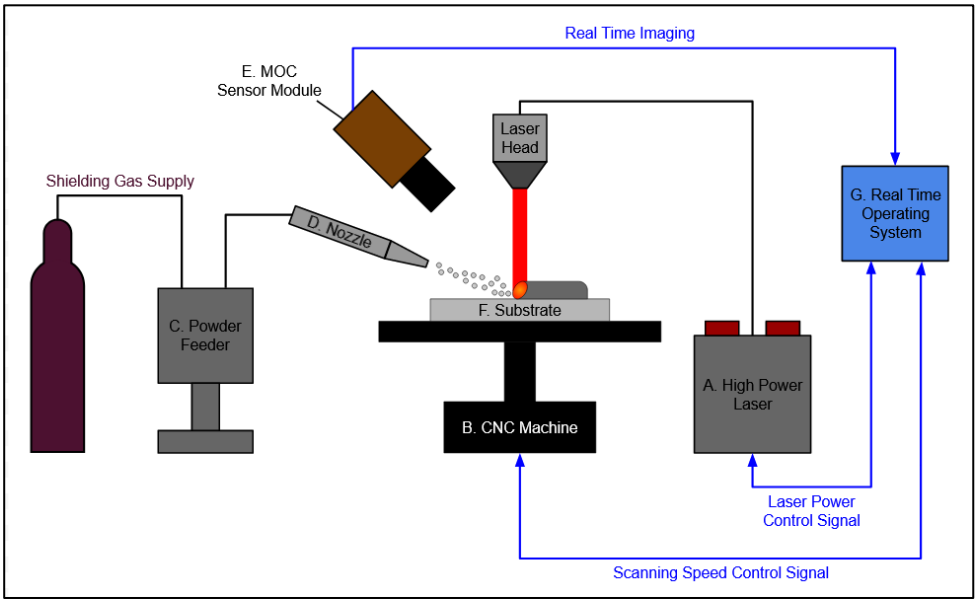

Figure 3-3 Schematic representation of the main components featured in LMP

The main components of the LMP system are briefly described below:

A. **High power laser:** The energy source used for experiments is an IPG fiber laser YLR-1000-IC operated in continuous mode with a maximum power of $1.1\ kW$. The fiber laser has an operating wavelength of $1070\ nm$ and a Gaussian beam intensity distribution.

B. **Powder feeder:** A Sulzer Metco TWIN 10-C powder feeder with two $1.5\ L$ hoppers is used to deliver the argon shielding gas, and to control the powder feed rate. The feed rate and flow rate are controlled manually and can accommodate a wide range of powders that can be sprayed at feed rates from 2 to $150\ g/min$.

C. **CNC machine:** A 3-axes Fadal VMC 3016 was modified by adding two additional rotational axes to produce a 5-axes CNC machine to be used as the positioning device. The travelling speed of the CNC is effectively the scanning speed of the laser during LMP.

D. **Nozzle:** The powder is fed through an off-axis nozzle onto the substrate with input diameter $1.6\ mm$ and output diameter $3.1\ mm$. The nozzle is installed on a mechanism with four degrees of freedom, providing good positioning for focusing the powder onto the laser beam spot.

E. **MOC Sensor Module:** The MOC sensor described in Section 3.1 features visible light and IR sensors to capture images during the LMP processes in real-time. Processing these raw images returns critical information regarding the current state of the HAZ, such as the thermal dynamics and geometry of the clad (in the case of LDED).

F. **Substrate Material:** The substrate material is the initial workpiece upon which the LMP process is applied, in the case of LDED, the initial layer is fused to the substrate. Hence, the substrate material must be selected to be compatible with the powder material, otherwise unintended alloys or defects may form when using dissimilar materials.

G. **Real-time operating system:** Data acquired from the MOC sensor is sent to the operating system via a National Instruments (NI) real-time platform and LabVIEW. CNC travelling speed, laser power and laser spot size are controlled using an NI PCI-7340. The operating system can run the process parameters at a set point or use the data from the MOC sensor to control the parameters in real-time.

This experimental setup was used to perform LMP experiments, which includes both LHT and LDED. NI LabVIEW was implemented to send the desired process settings to the Fadal CNC and laser controllers to ensure that the proper values were used during each experimental run. Most experiments

with this system were conducted with the MOC sensor positioned in a lateral FOV, as seen in Figure 3-4, which features the LMP setup used in the ALFa laboratory. This camera position allows for thermal dynamics and height to be monitored in real-time, thus was considered a reasonable setup to validate this system. For LMP experiments, the powder feeder is not connected to a controller and is not capable of sending automatic changes to the powder flow rate or gas pressure. Therefore, these values were manually set and remained constant throughout all experiments, where the process variables were the scanning speed and laser power, since these parameters can be controlled.

Figure 3-4 Image of the LMP setup used in the ALFa Lab to validate this research

The camera was positioned laterally at an angle of 45°, this position offers a reasonable compromise in the temperature distribution and geometry measurements since a position of 0° would allow for height to be measured with no projection, but an angle of 90° (coaxial imaging) would allow for the width and temperature distribution to be measured with no projection. Hence, 45° was selected as a reasonable compromise as it is the maximum of

$$f(\theta) = \sin\theta + cos\theta \quad \textbf{(3.1)}$$

Moreover, since the camera is mounted to the laser head, the relative position of the camera to the melt pool is known and constant as it was calibrated upon installation.

3.3 Laser Arc Hybrid Welding Experimental Setup

One of the objectives of this research is to demonstrate that this monitoring system is robust enough to work on various thermal processes. Therefore, experiments were also conducted in collaboration with CAMJ at the University of Waterloo. Specifically, a hybrid laser and arc welding system was used to capture data and augment the experiments that could be conducted in the ALFa laboratory. This setup differs from the LMP system described previously in three significant aspects. (1) A wire feedstock is used, as opposed to powder. (2) The laser is capable of a maximum power of 8kW. (3) The laser head can be swapped to feature different capabilities, such as using only the laser, or only an arc welding process, or a hybrid process in which both the laser and wire arc are present during manufacturing. The different material, feedstock form, and energy source show that this process is different from the LMP setup described above. Hence, validating the MOC sensor with this setup shows that the system can be utilized with different thermal processes. Figure 3-5 below highlights the key components of the hybrid laser arc experimental setup at CAMJ.

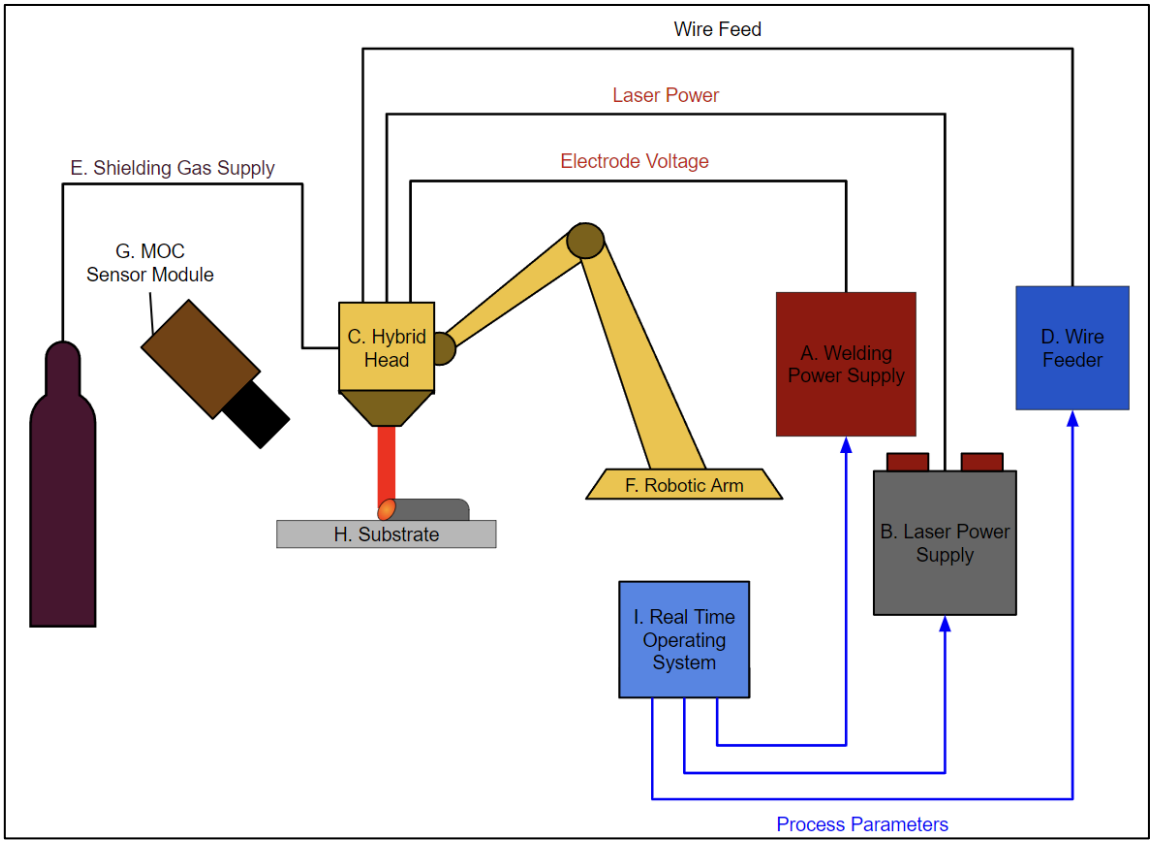

Figure 3-5 Schematic diagram of the hybrid laser arc process

The main components of the GMAW system are described as:

A. Welding Power Supply: Lincoln Electric Power Wave S500 advanced process welder provides the electrical energy required to create the welding arc, with the capability of different combinations of voltage and current depending on the application.

B. Laser Power Supply: An IPG YLS-8000 fiber laser operated in continuous mode with a maximum power of $8\,kW$, an operating wavelength of $1070\,nm$, and a Gaussian beam intensity distribution.

C. Hybrid Laser Arc Welding Head: Holds and guides consumable wire electrode, directs shielding gas flow, and positions laser spot to ensure the correct process settings. This head allows for flexible combination of laser and electric arc parameters for various manufacturing applications.

D. Wire Feeder: Lincoln Electric 4R220 AutoDrive wire feeder supplies the consumable wire electrode to the hybrid laser arc welding head at controlled rate based on the process parameters and selection of wire.

E. Shielding Gas Supply: Provides the appropriate mixture of CO_2 and argon gas to protect the melt pool from atmospheric contamination.

F. Robotic Arm: FANUC M-710ic is a 6-axis robotic arm which positions and moves the welding head to achieve the desired process path. The unit used in CAMJ is programmed to use 5 different heads during manufacturing.

G. MOC Sensor Module: The MOC sensor described in Section 3.1 is again used to capture visible light and IR images during the welding in real-time. Processing these raw images returns critical information regarding the current state of the HAZ, such as the thermal dynamics and geometry of the weld bead.

H. Substrate Material: The substrate material is the initial workpiece upon which the weld is fused to, the material must be selected such that it is compatible with the wire material.

I. Real-time operating system: Controls various parameters during welding such as welding current, voltage, voltage mode (whether continuous or pulsed), wire feed speed, and gas flow rate. Lincoln Electric provides control options with various preset modes, including continuous voltage and variations of pulsed volage options.

This setup can produce high quality welds with a high-powered laser and electric arc heat source. This system can adjust the laser power, welding voltage, voltage mode, and welding speed based on the material and desired process settings. However, these properties are set before starting the program, thus there is no potential to use this system with real-time control. Hence, it was used strictly to validate the monitoring capabilities of the MOC sensor. Figure 3-6 shows the MOC sensor mounted to robot arm for a lateral FOV of the melt pool during thermal process with this system.

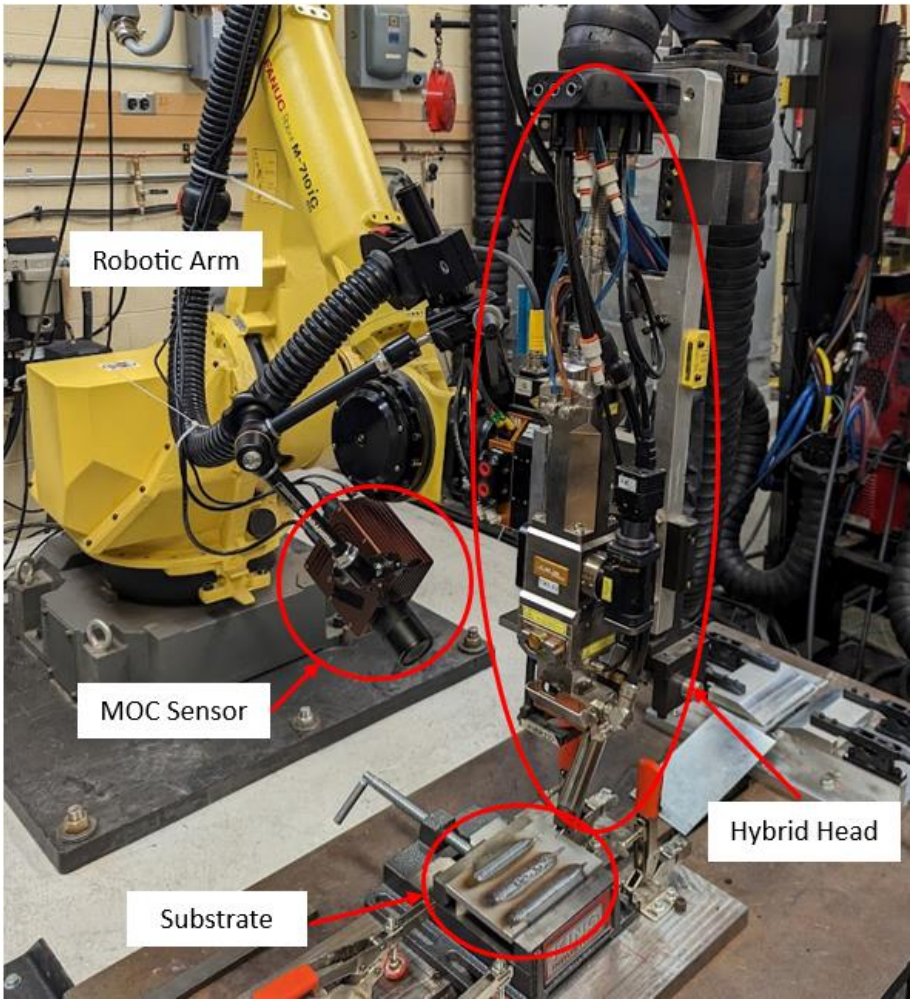

Figure 3-6 Image of the hybrid laser arc system used to validate this research at CAMJ

3.4 Image Evaluation

With the prototype MOC sensor developed and tested in the ALFa Laboratory, the quality of images must be evaluated, and any artifacts or other deviations present in the images must be explained and

corrected. One such unintended side effect of the cold mirror placed inside the optical system is the double images, an optical phenomenon also known as ghost images or ghosting, that are caused by internal reflections of light. These ghost images are visible with both camera sensors as described in Figure 3-7.

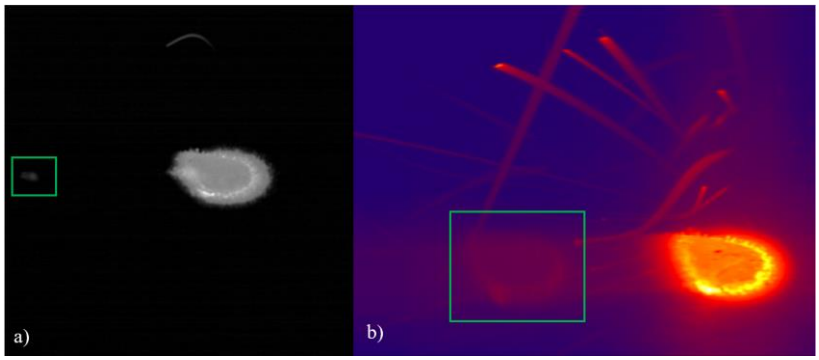

Figure 3-7 Internal reflections in a) vision images b) IR images

Figure 3-7a shows an image captured by the vision camera during LDED, though the internal reflections are not significant, artifacts are visible as a result, as outlined in green. Figure 3-7b demonstrates that during LDED the IR images clearly show the ghost image, as bounded by the green box. The ghost images are present in thermal processes because the light source is so bright that the reflected light is still visible to the sensor, despite only a 5-10% of the light being reflected internally according to the cold mirror manufacturer [110]. Figure 3-8 further illustrates how the internal reflections of the cold mirror result in the undesired ghost images.

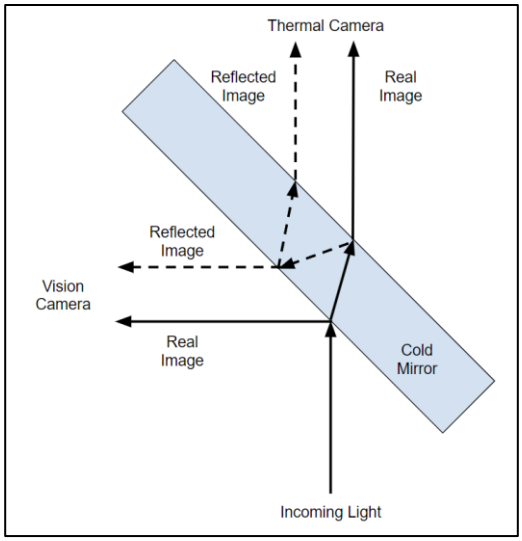

Figure 3-8 Diagram of internal reflection resulting in ghost images

To remove the artifacts caused by ghost images, the cold mirror was replaced with a pellicle beam splitter. The BP145B2 pellicle beam splitter was selected as it consists of a thin, semi-transparent nitrocellulose membrane, which virtually eliminates ghosting since the second surface reflection is superimposed onto the first one [111]. The reflectivity and transmissivity of the beam splitter is summarized in Figure 3-9.

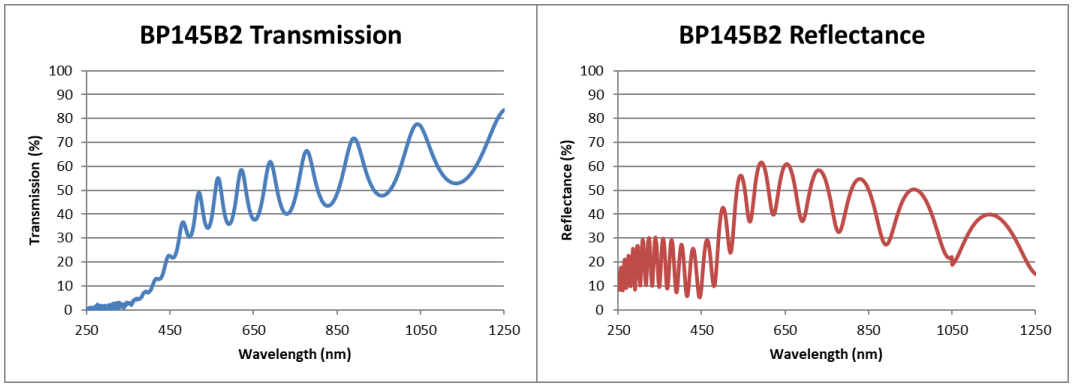

Figure 3-9 Transmission and reflectance of BP145B2 [111]

From Figure 3-9 it can be deduced that approximately 53.6% of 800nm light is transmitted into the IR camera sensor. Therefore, this optical solution eliminates the ghosting defects, but reduces the effective temperature range by reducing the amount of light entering the IR camera.

Furthermore, updates were made to the image filters in front of the vision camera. An ND60 filter, which allows 25% transmission, was incorporated, along with a narrow bandpass filter centered at 850nm. The pellicle beam splitter's performance, as shown in Figure 3-9, reflects 49.67% of light centered at 850nm into the vision camera. The selection of an 850nm filter was driven by various optical considerations for the MOC sensor and the LMP system used for its validation. To direct the laser towards the substrate, a 45° mirror reflected the laser beam, which is visible in Figure 3-4. The mirror's transmission curve, depicted in Figure 3-10, allowed light between 750nm and 975nm to pass through while reflecting 1070nm and 660nm. This ensures the correct positioning of the laser beam and guide laser without damaging other components. Additionally, since the IR camera selected has a spectral response around 800nm it can capture images coaxially since the mirror transmits that wavelength. Moreover, using a similar wavelength with the vision camera maintains similar emissivity values for temperature calculations. This principle aligns with two-color pyrometry, where two wavelengths of light are captured to determine temperature independent of emissivity, which is assumed constant for both wavelengths. Finally, using a narrow wavelength also reduces the deviations caused by changes

in emissivity and the different quantum efficiency of the camera sensor at different wavelengths. Therefore, the 850nm narrow bandpass filter is selected since it allows for coaxial imaging, sufficient light is reflected by the pellicle beam splitter, and the similar wavelength to the IR camera reduces deviation caused by the unknown emissivity.

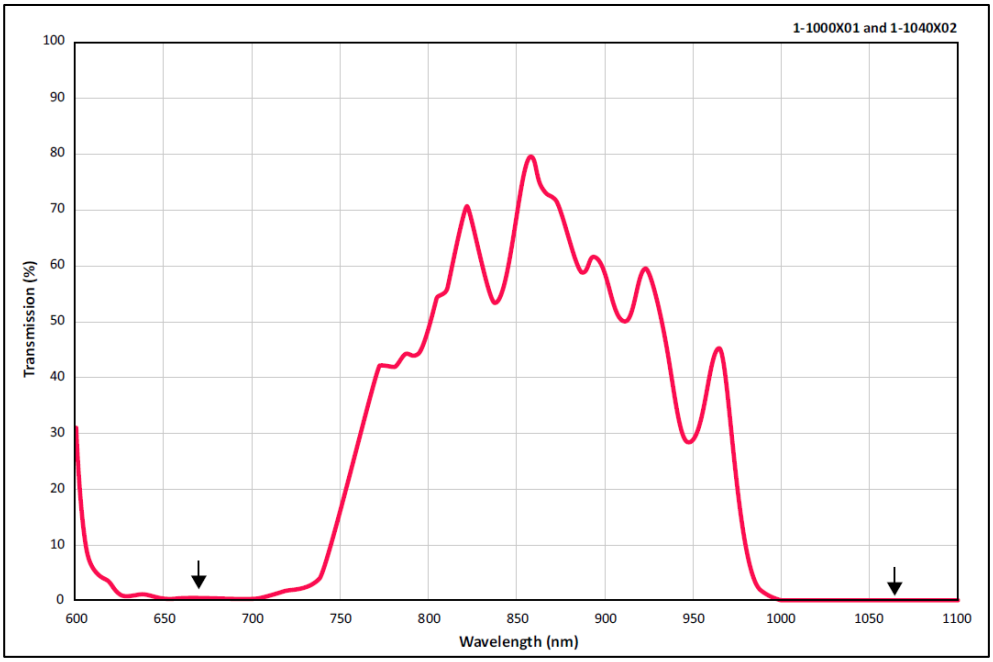

Figure 3-10 Typical curve of transmission for the mirror (1-1040X02). Transmission at 45° angle [112]

3.4.1 Intensity Distribution

The temperature distribution must be considered as well, as shown in Figure 3-11 there are higher measured temperatures at the periphery of the melt pool, though the center typically has the highest energy density in LDED; hence, this phenomenon is further explored. Higher intensities are measured around the melt pool in the vision camera as well, suggesting that this phenomenon is not exclusive to the camera sensor. This temperature distribution was also demonstrated in [113], where the authors claim the higher emissivity of the solid material at the periphery of the melt pool characterizes the distribution.

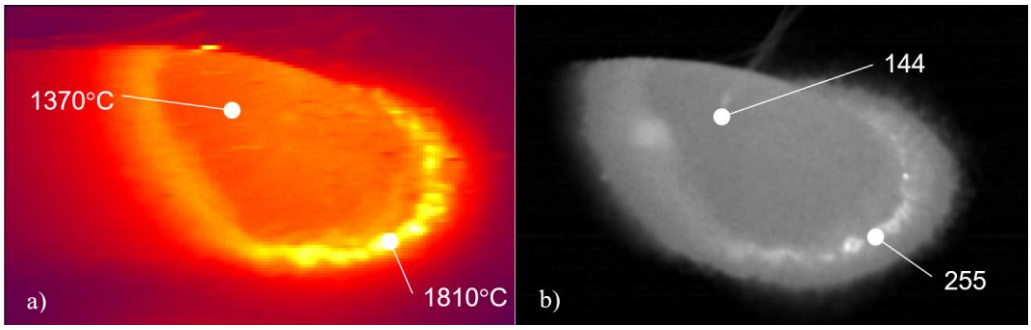

Figure 3-11 a) Typical temperature distribution during LDED b) Typical vision image during LDED

Since the laser is assumed to have a Gaussian distribution of intensity, the highest energy is at the center of the laser spot. This seems to be contradictory to the perceived temperature distribution of the melt pool since the edge of the melt pool registers the highest temperature. This discrepancy is likely caused by the different emissivity of steel at different temperatures and phases. Emissivity is the measure of an object's ability to emit light, which changes based on the wavelength of light and the object's material properties. Assuming that the emissivity of solid steel is higher than that of the molten steel then high temperature solid steel may be perceived as hotter than the molten steel. Since the IR camera is only capturing images in a narrow wavelength, it is more sensitive to emissivity changes. Since emissivity is dependent on the material, surface quality, wavelength of light and temperature of material it is difficult to know [114]. Thus, the experiment shown in Figure 3-12 was conducted to support the hypothesis that the temperature measurements are affected by the changing emissivity. The experiment featured a substrate of 1/4 in thick 410 stainless steel that was rinsed with ethanol and quenched in acetone for 10 seconds to ensure the substrate was clean and at room temperature. Stainless steel was selected because it is a commonly used material in LMP and the powder used in LDED is stainless steel, though other experiments featured cold rolled steel as the substrate material. The experiment consisted of a single LHT track with a constant scanning speed of 175 mm/min while the laser power increased linearly from 250W to 600W. Though the higher temperature periphery was observed in LDED, the hypothesis was tested with LHT to determine whether the powder influenced the temperature distribution.

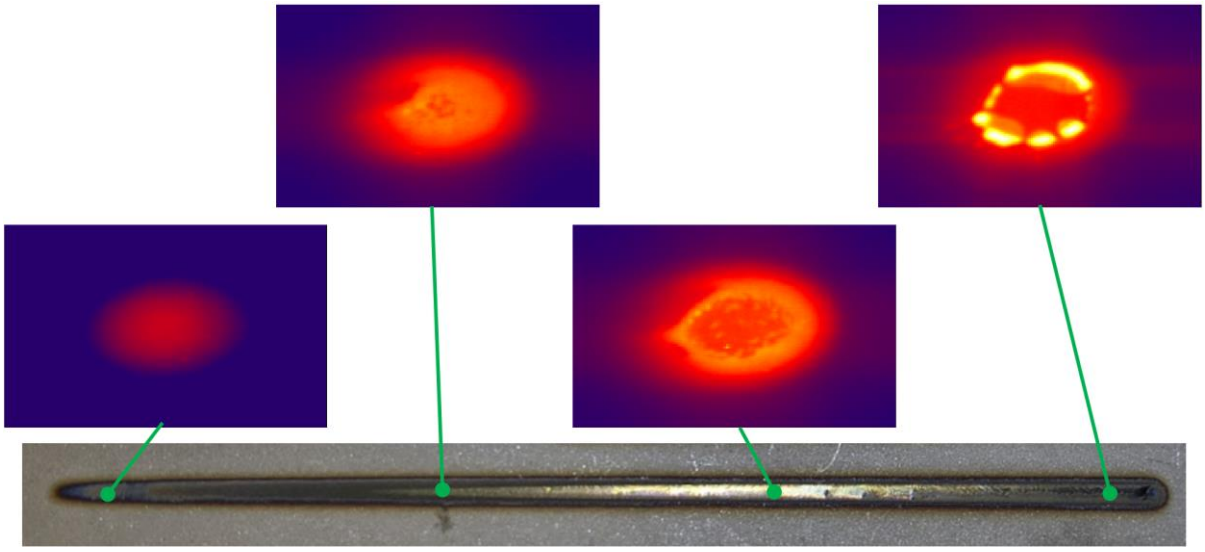

Figure 3-12 Evolution of temperature distribution during LHT power ramp

Since the high intensities at the periphery of the HAZ are shown in Figure 3-12 the distribution is not caused by the powder. Moreover, the peak temperature of the HAZ is in the center at the beginning of the track, which confirms that the center of the laser spot corresponds to the area with the highest energy flux. Therefore, the high temperature measurements at the periphery of the HAZ are not caused by the laser energy distribution either. At the end of the track is where there are high temperatures on the periphery of the HAZ. This corresponds to when the substrate begins to melt, as evidenced by its surface quality. Thus, the temperature distribution is likely a measurement error caused by the different emissivity of the solid and liquid phases of stainless steel. The results are further supported by Devesse et al. in [115] where a laser melting experiment was conducted on a stainless steel substrate demonstrating the emissivity varied from 0.2 to 1 across the melt pool due to the different material phases.

Finally, a similar result was shown by Altenburg et al., in which the effective emissivity distribution of the HAZ is plotted [116]. Where multispectral thermography was used in which the melt pool was captured in 8 different experiments with the same process parameters. The only variable across these experiments was the application of a 25nm narrow bandpass filter with central wavelength ranging from 1.2µm to 1.55µm with steps of 50nm. This allowed the relationship between emissivity and temperature to be found at each wavelength, which was used to map the emissivity across the entire melt pool shown below.

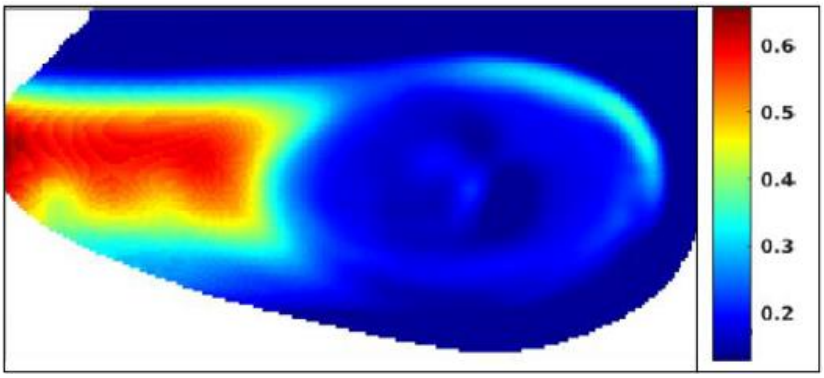

Figure 3-13 Rescaled relative effective emissivity distribution [116]

Though Figure 3-13 is a numerical approximation of the emissivity, it explains the temperature distribution that is observed in the images captured by the MOC sensor as well. Therefore, as shown in the experimental results summarized in Figure 3-12 and in supporting literature, the brighter region around the HAZ is caused by the material. Specifically, this region is characterized by rapid phase changes, differing degrees of oxidation, and temperature variation, all of which affect the emissivity. Since this phenomenon is caused by the material properties of the substrate and powder, not the camera sensor, this shows that the camera measurements are comparable to other sensors used in literature.

These preliminary images demonstrate that the MOC sensor has performance comparable to other imaging systems used to monitor thermal processes in literature. Additionally, it has been shown that the ghost images have been explained based on the optical components and corrected by selected new components. Furthermore, the unexpected temperature distribution is also explained based on the performance of other monitoring systems and justifications of similar phenomenon found in literature.

3.5 Summary

This chapter described the design of the MOC sensor, which is intended for real-time monitoring of thermal processes. The sensor features a CMOS visible-light camera to capture high resolution images at a high frame rate for geometry predictions and an IR camera sensor for thermal dynamics. The sensor is capable of capturing and processing images at a framerate of 20Hz, with temperature measurements between 600°C – 1900°C, this range is critical because it encompasses the melting point of steel alloys and other common materials used in thermal processes. Moreover, the FOV is approximately 35mm × 35mm, which allows for high resolution imaging of the melt pool and HAZ.

All the key components of the apparatuses used to conduct LMP, GMAW, and hybrid experiments were outlined in this chapter as well. Finally, the quality of captured images was evaluated, and two anomalies were noted. Firstly, a ghost image was visible in the captured frames of both the CMOS and IR cameras, this was caused by the cold mirror used to direct the light into the corresponding camera sensors. To correct the resulting artifacts, a pellicle filter was used instead, which features a thinner membrane to reduce the influence of ghost images. Another anomaly discovered by analyzing the images was the hotter temperatures captured around the center of the melt pool. Conducting experiments concluded that the higher temperature measurements are caused by rapidly changing emissivity corresponding to the changing phases of the HAZ. Consulting literature on this topic further supported this hypothesis.

Chapter 4
Real-Time Temperature Measurement Using a Pyrometer and CMOS Camera

In thermal processes, the thermal dynamics are directly related to the quality of the final product, having a direct relationship to the microstructure and other material properties. Thermal dynamics can be measured with an array of sensors, such as pyrometers, thermocouples, and thermal imaging. Pyrometry allows for temperatures to be measured accurately based on the black body radiation emitted from the desired subject. However, these measurements are typically limited to a small region and are susceptible to errors caused by changes in emissivity, which affects the radiation emitted by the subject. Thermocouples are capable of measuring a wide range of temperatures, however, since the sensor needs direct contact with the subject, they cannot be used to directly monitor the HAZ of the processed location. Finally, thermal imaging can be used to estimate the temperature distribution. This technique utilizes the same principles as pyrometry, which also makes it sensitive to emissivity changes. However, since a 2-dimensional temperature distribution is found, relative temperature measurements can be calculated across the HAZ, offering more information than single-point pyrometry.

Typically, thermal imaging is conducted with IR cameras. Though these tools offer calibrated temperature measurements, they may require specialized lenses and other optical components to work properly. Moreover, these cameras often offer lower framerate, resolution, and less customization while being more expensive than visible light cameras. Another technical specification that must also be considered is the effect of rolling or global shutter. A rolling shutter, which many IR cameras feature, results in fast moving objects in the frame becoming distorted as shown in Figure 4-1.

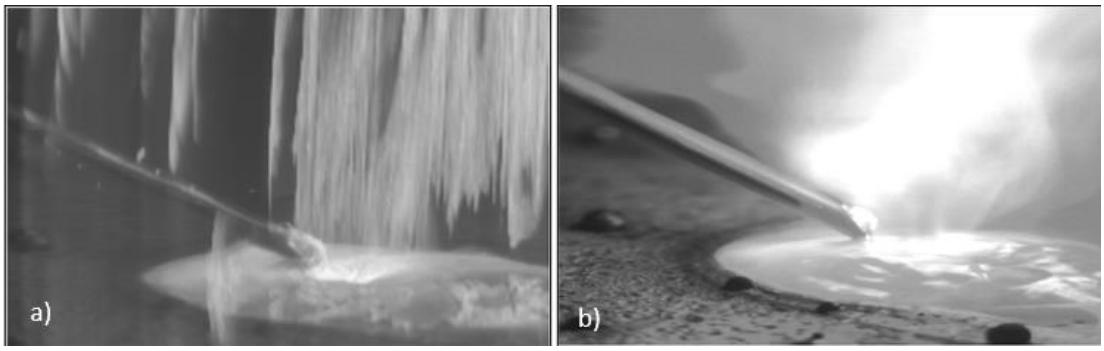

Figure 4-1 Images captured with a) IR camera featuring rolling shutter and b) visible light camera featuring global shutter

Ultimately, visible light cameras typically offer more flexibility in their applications and have better technical specifications than IR cameras. Therefore, this chapter discusses the implementation of a pyrometer and visible light camera used simultaneously to estimate the temperature distribution based on calibrated temperature measurements and images of the HAZ. This methodology allows for higher resolution temperature measurements with a more cost-effective sensor module than IR imaging.

4.1 Model Based Temperature Prediction

The model-based temperature prediction utilizes a pyrometer measurement at the center of the melt pool and boundary temperatures estimated through a combination of visible light imaging and machine learning. For this application, since a two-dimensional model is implemented, this is most appropriate for LHT, since the shape of the deposition does not need to be accounted for in the model. The model used to predict the intermediate temperatures is based on the three-dimensional heat conduction equation, as the other forms of heat transfer are assumed to be negligent. The three-dimensional heat conduction equation is taken as:

$$\frac{\partial^2 T}{\partial x^2} + \frac{\partial^2 T}{\partial y^2} + \frac{\partial^2 T}{\partial z^2} + \frac{1}{k}\dot{e} = \frac{1}{\alpha}\frac{\partial T}{\partial t} \tag{4.1}$$

in the xyz coordinate system. Where the respective time is t, T represents the temperature distribution, k is the thermal conductivity, $\dot{e}$ is the heat input over time per unit volume, and α is the thermal diffusivity, which is dependent on the conductivity, specific heat, and density of the material.

Since only the surface temperatures can be monitored with imaging systems, the heat conducted in the z-direction is neglected. Additionally, a new moving coordinate system must be implemented to consider the energy source as a moving point to account for the scanning speed. Applying these changes to Eq. (4.1) results in:

$$\frac{\partial^2 T}{\partial \xi^2} + \frac{\partial^2 T}{\partial y^2} + + \frac{1}{k}\dot{e} = \frac{1}{\alpha}\left(\frac{\partial T}{\partial t} - v\frac{\partial T}{\partial \xi}\right) \tag{4.2}$$

where ξ represents the moving coordinate system defined by $\xi = x - vt$, and v is the scanning speed of the laser. Eq. (4.2) features partial derivative terms, which are too computationally expensive to compute for real-time monitoring. Therefore, the HAZ is simplified as a nodal network, allowing this equation to be discretized using finite differences. Figure 4-2 shows a schematic of the nodal network

used to approximate the substrate. The discretized approximation of Eq. (4.2) was found by using finite differences to calculate the derivative values and is given as:

$$T_{m,n}(k+1) = Fo\left(T_{m+1,n} + T_{m-1,n} + T_{m,n+1} + T_{m,n-1}\right) + (1-4Fo)T_{m,n} + \frac{\alpha\Delta t}{(\Delta\xi)^2 k\Delta z}\dot{e} + \frac{\Delta t}{2\Delta\xi}\left(T_{m+1,n} + T_{m-1,n}\right)v \quad \textbf{(4.3)}$$

where $T_{m,n}$ is the temperature of a node, m, n represents the coordinates of the node, k is the current timestep, Fo is the Mesh Fourier Number $\left(Fo = \frac{\alpha\Delta t}{(\Delta\xi)^2}\right)$, and Δt is the length of each timestep. In LHT experiments the heat input, $\dot{e}$, is defined by the laser power, which is assumed to have a Gaussian distribution.

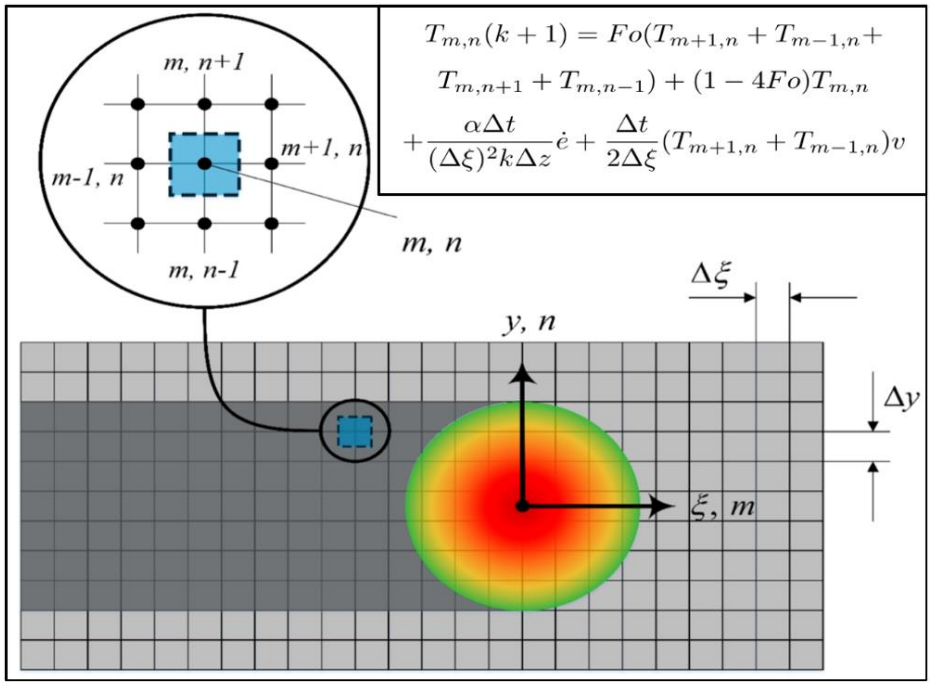

Figure 4-2 Visual representation of the substrate nodal network and the mathematical model used for calculating the intermediate temperatures [75].

With the temperature approximation model defined, boundary conditions must be established to ensure that the temperatures are solvable. In this case, certain temperatures of the nodal network are assumed to be known and the model was then implemented to calculate the intermediate node temperatures. During LHT, the HAZ was approximated to be a region of 20 × 11 pixels, with each pixel approximately 0.35 mm × 0.35 mm, as limited by the IR camera used to capture temperature data

(Jenoptik IR-TCM 384). The temperatures that are assumed to be known in this case are the peak temperature at the center of the melt pool, which is measured with a pyrometer and the temperatures around the melt pool, which are estimated by intensity measurements captured with a camera. Furthermore, the HAZ is assumed to be symmetric along the direction of travel to simply the boundary conditions. Figure 4-3 shows a diagram of the nodal network with the boundary conditions highlighted. The center of the melt pool is highlighted in green to represent the temperature measurement from the pyrometer and the nodes highlighted in blue represent the temperatures predicted by the visible light camera.

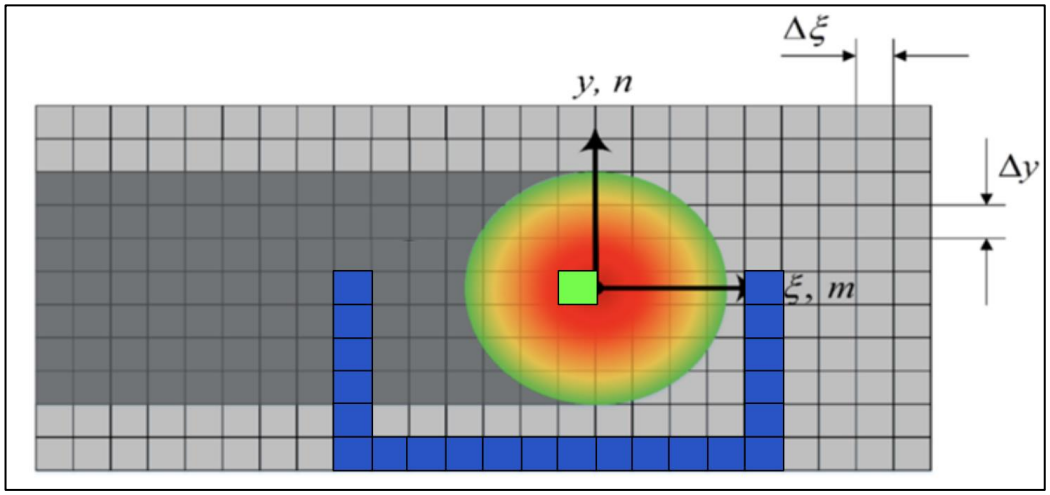

Figure 4-3 HAZ nodal network with highlighted boundary conditions

To estimate the temperatures of the nodes highlighted in blue in Figure 4-3 a DALSA Genie 1024 CCD camera was used to capture images in real-time. A sample of the quality of images captured with the Genie 1024 camera is visible in Figure 4-4 where the boundary nodes are highlighted in white.

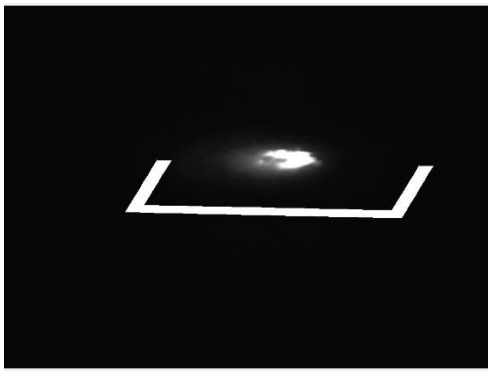

Figure 4-4 Sample image captured with DALSA Genie 1024 during LHT

Since this camera is not calibrated for temperature measurements, ML was implemented to utilize data extracted from these images and process parameters to predict the required temperature. LHT experiments were conducted using the experimental setup outlined in Section 3.2 to create datasets used to train, validate, and test the ML algorithm. However, a modification was implemented where the temperature distribution was captured with an IR camera (Jenoptik IR-TCM 384) simultaneously to the Genie 1024 images and pyrometer measurements of the center of the HAZ. Using this data, the temperature of the desired pixels of the HAZ were mapped to the corresponding pixels of the Genie 1024 images. The process parameters of these experiments are summarized in Table 4-1 and Table 4-2.

Table 4-1 Process Parameters for the training and validation set

	Training and Validation Data							
Laser Power	100	250	325	250	200	275	425	400
Scanning Speed	2.5	2.5	2.5	3.33	4.16	4.16	4.16	5

Table 4-2 Process Parameters for the test set

	Test Set			
Laser Power	175	400	350	200
Scanning Speed	2.5	3.33	4.16	5

The desired output of the ML algorithm is the temperature of each boundary pixel, referred to as the node temperature. To predict this temperature the following features are extracted from the Genie 1024 images: number of saturated pixels, average brightness of the entire image, and pixel brightness. Process parameters were also used to augment the temperature prediction, namely the scanning speed and laser power. The location of the node is necessary as well, described in xy coordinates and as the distance between the node and the center of the melt pool. Finally, the maximum temperature at the center of the melt pool measured with a pyrometer is used as an input as well. Figure 4-5 summarizes the featured used to predict the temperatures of the boundary nodes and the correlation between these features and the temperature of the boundary nodes.

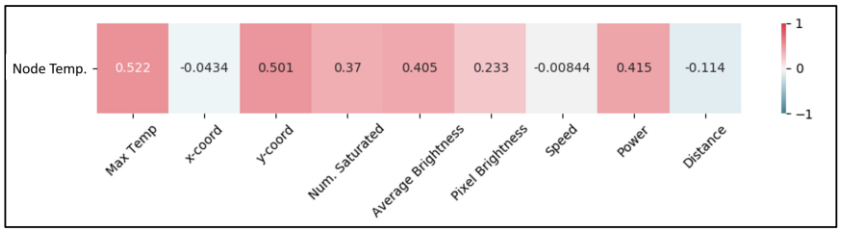

Figure 4-5 Correlation matrix between the pixel temperature and feature space

The ML algorithm used to predict the temperature of the boundary nodes was gradient boosted trees, which utilizes a combination of simple decision trees to make a prediction. Decision trees are classification or regression models with a tree-like architecture [117]. With Decision trees, the dataset is broken into smaller subsets, while at the same time a decision node is created. Each internal node of the tree represents a different pairwise comparison on a feature, whereas each branch represents the outcome of this comparison. Leaf nodes represent the final decision or prediction. The MAPE of the ML algorithm is shown in Figure 4-6, where the error has a normal distribution with a 0.7% MAPE and 3.6% standard deviation for the training set and a 7.3% MAPE and 5.0% standard deviation for the test set.

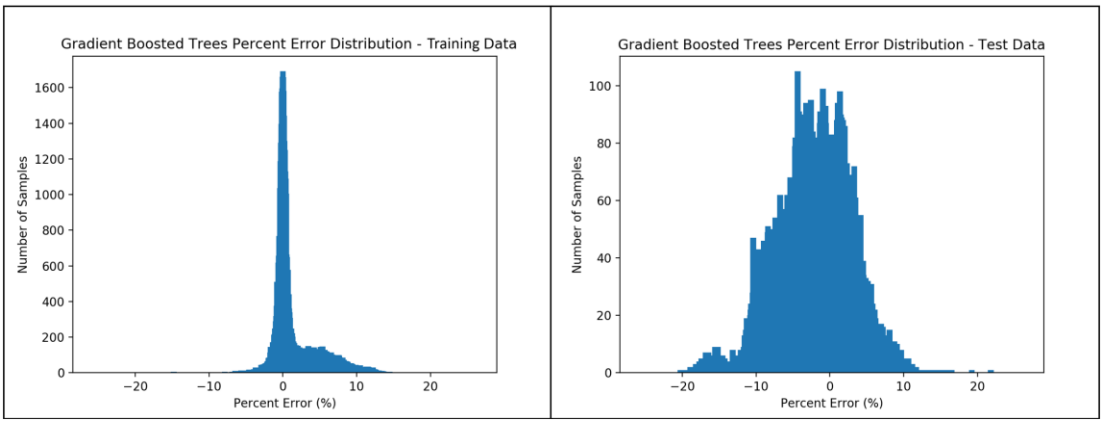

Figure 4-6 Percent error of temperature prediction algorithm

Once the boundary conditions are predicted, the numerical model was used to calculate the intermediate temperatures. The results of temperature prediction are shown in Figure 4-7 and Figure 4-8, where the boundary temperatures are predicted with a MAPE of 2.71%. The measured temperatures were captured with a Jenoptik IR-TCM 384 which returned calibrated temperature distribution of the HAZ. The combination of measured peak temperature, predicting the boundary temperatures, and calculating the internal temperatures of the distribution are shown in Figure 4-7b and Figure 4-8b while the real temperature distribution captured with the Jenoptik IR-TCM 384 is shown in Figure 4-7a and Figure 4-8a. Figure 4-8c shows the error between the predicted and measured temperature distributions.

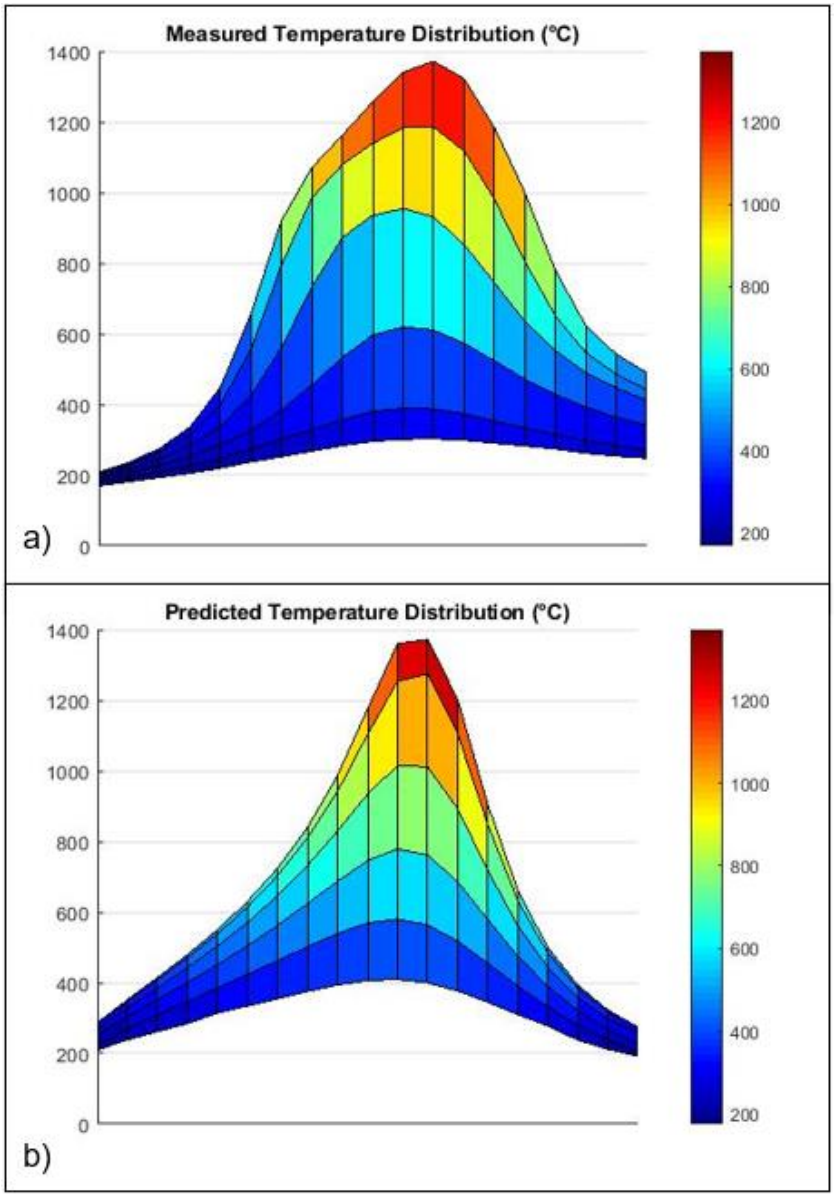

Figure 4-7 a) Temperature distribution measured by infrared camera b) Temperature distribution calculated via random forest boundary predictions and mathematical model. Note that the red arrow depicts the scanning direction of the laser.

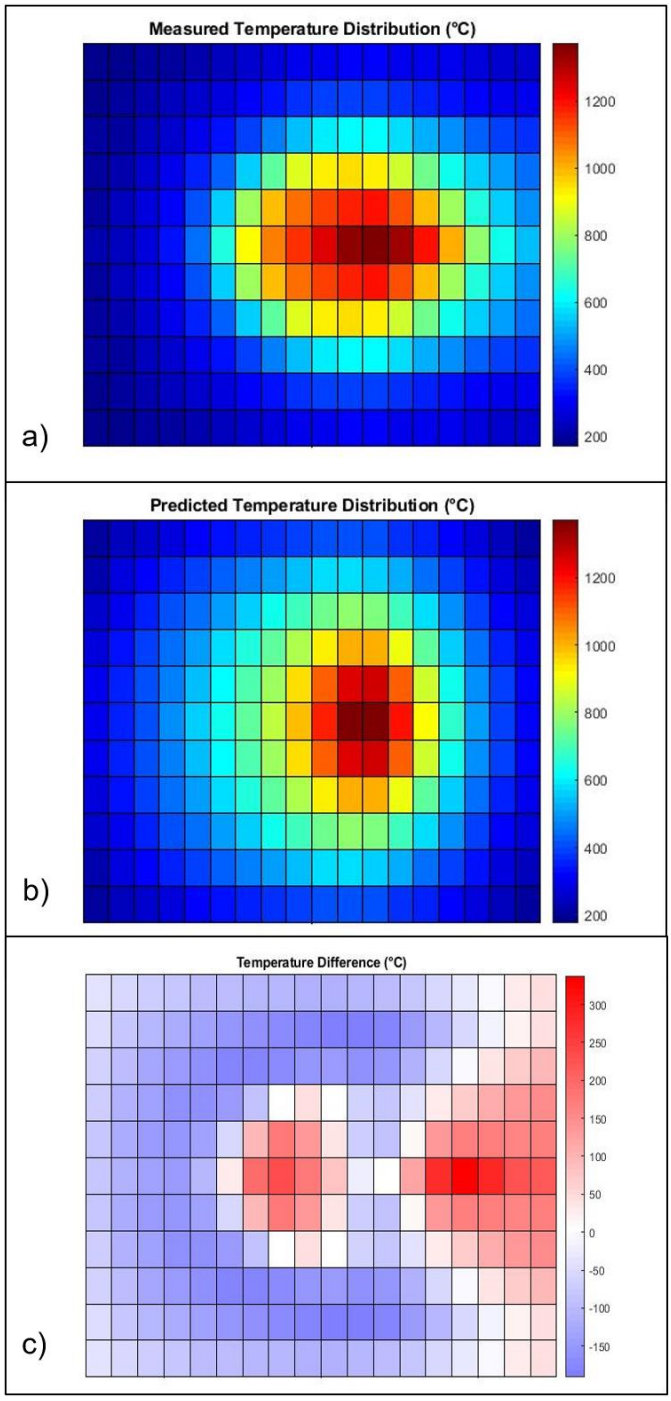

Figure 4-8 a) Heat map visualization of temperature distribution measured by infrared camera b) Heat map visualization of temperature distribution calculated via random forest boundary predictions and mathematical model, where the boundary pixels are the predicted temperatures c) difference between the measured and calculated temperature distributions. Note that the red arrow depicts the scanning direction of the laser.

During LHT the model-based temperature prediction of the HAZ results in a MAPE of approximately 11.3% for the test set shown in Table 4-2. This performance includes both the boundary conditions which are predicted with ML and the intermediate temperatures which are calculated based on the generalized heat conduction model. The error is assumed to be zero at the center of the melt pool as this temperature is based on the pyrometer measurement.

4.2 Numerically Predicting Temperature with High Dynamic Range Camera

A model-based approach is limited because of the necessity to use approximations to simplify the state of the system. It was previously discussed that the model assumes some temperatures are known and the intermediate temperatures are calculated through a conduction model. The conduction model itself is an assumption that neglects other forms of heat transfer. To calculate the intermediate temperatures, the thermal conductivity and specific heat capacity are assumed as well, which is another source of error since these values change with temperature. The energy input is assumed as well, which in the case of a laser energy source, neglects the reflectivity of the surface and assumes the laser has a perfect distribution. While other energy sources, such as electric arc, are more difficult to include in the conduction model. Moreover, since the temperature distribution is calculated over the surface of the HAZ, the model would need to account for the shape of the clad in thermal processes where material is deposited.

Therefore, a numerical approach that estimates the temperature based on the intensity captured by the visible light camera is a more suitable approach, since less assumptions need to be made and the model would not be dependent on the conduction properties of the material. This motivated the upgrade to the HDR Photonfocus camera and optical components detailed in Chapter 3.

4.2.1 Design of Experiments

To use a visible light camera to estimate the temperature distribution of the HAZ, the MOC sensor described in Chapter 3 was utilized to capture data during additive manufacturing (AM). This tool was vital in gathering data since it allows for thermal images and vision images to be captured simultaneously. Data was acquired during laser deposition of metal based on the AM layer-by-layer approach onto a 6.3 mm substrate of 1018 cold-rolled steel with a laser spot diameter of 3 mm. Three layers of a thin-walled cylinder were produced using 106 µm type 431 stainless steel powder with a flow rate of 3.25 g/min. Stainless Steel 431 (UNS S43100) is a martensitic stainless steel with

composition shown in Table 4-3. Since the camera is mounted to the laser head, the relative position of the camera and the HAZ remains consistent during all layers of deposition.

Table 4-3 Composition of type 431 stainless steel

Element	Fe	Cr	Ni	C
Weight %	Balance	17	2	0.18

Each layer had a diameter of 24 mm, and the process parameters were a laser power of 1 kW and a scanning speed of 1.5 mm/s. Figure 4-9 shows the final cylinder which was produced to generate the data for this section. A cylindrical part was developed to ensure greater variation in the captured images than with a linear clad.

Figure 4-9 Appearance of AM track used to generate temperature prediction

While the above cylinder was manufactured the MOC sensor was used to capture frames with the vision camera set to an exposure time of 3500 µs. It is critical to note the exposure time during these experiments since this property is directly related to the amount of light captured by the camera sensor, which affects the measured intensity. This principle is based on Planck's law, Eq. (4.4), which describes the relationship between a black body's temperature and the magnitude of radiation that the black body is emitting [118], and is given by:

$$B_v(v,T) = \frac{2hv^3}{c^2}\frac{1}{\exp\left(\frac{hv}{k_B T}\right) - 1} \tag{4.4}$$

where, B_v is the radiance of a body for a frequency of light, v, at absolute temperature, T, h is the Planck constant, k_B is the Boltzmann constant, and c is the speed of light in the medium, which is assumed to be air in this research. Planck's law shows when a body is at a given temperature, it will radiate a wide spectrum of light defined by Eq. (4.4), which is further demonstrated in Figure 4-10a.

This can be compared to the responsivity of the camera sensor Figure 4-10b. Since the responsivity of the camera is not uniform across all wavelengths of light, an integral would need to be performed to derive a relationship between the pixel intensity and temperature. This would reduce the computational efficiency of the algorithm and therefore an 850 nm narrow bandpass filter is added to the optical path. Additionally, this reduces the variability of emissivity, which is also dependent on wavelength. Furthermore, since the infrared sensor has an 800 nm filter [106], the emissivity values of both cameras would be comparable, which is a similar principle used in two-color pyrometry.

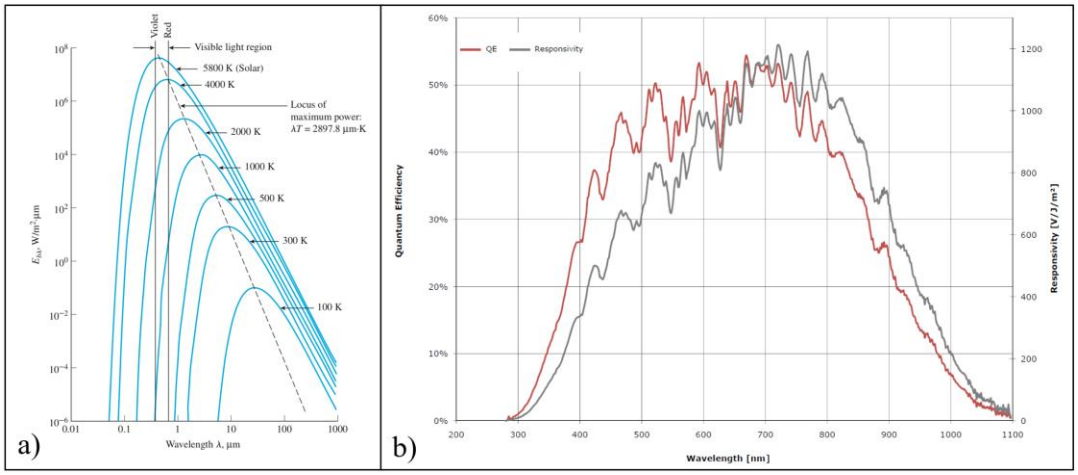

Figure 4-10 a) Visualization of Planck's law [118] b) Responsivity of A1312 CMOS sensor [107]

The emissivity of the HAZ is rapidly changing due to oxidation, phase changes, rapid temperature changes, etc., which makes it impossible to know the exact temperature of this region [115, 116]. Therefore, for the purposes of this study, it was assumed that the captured infrared images are accurate enough to approximate a temperature distribution based on its calibration. Moreover, when measuring the relative thermal dynamics, such as cooling rate, the exact temperature of the region has less of an impact on the calculation since the temperature difference is more critical [44]. Hence, the infrared camera captured images with the emissivity and transmissivity values of one to ensure that these properties did not affect the temperature measurements to derive a relationship between visible light intensity and approximate temperature that is independent of these properties. With these radiation parameters the infrared camera has a calibrated temperature measurement range of 625 to 1900 °C, which is the temperature range considered for this section. During this experiment, a total of 2264 frames were captured by each camera sensor, Figure 4-11 shows images from one timestep.

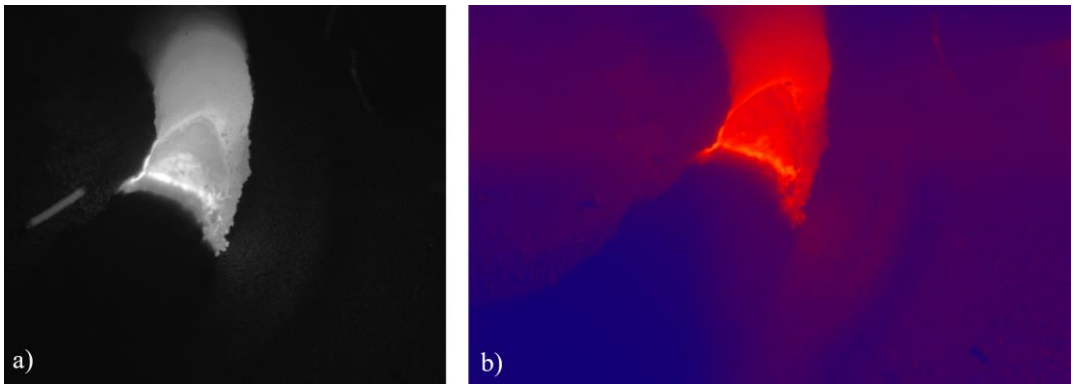

Figure 4-11 Sample images captured for temperature prediction from a) visible light camera and b) infrared camera

As demonstrated in Figure 4-11 each timestep has an image captured with the visible light camera and a corresponding temperature distribution captured with the infrared camera. Hence, this data can be used to determine the relationship between the intensity of visible light and the temperature of that region of the HAZ. The image captured in Figure 4-11a is saturated, this is due to the intensity of light emitted from the HAZ and the camera settings, most notably the exposure time of 3500 µs. Since this camera features an HDR sensor, different camera settings would compensate for the saturation, but a constant exposure time was used in this study for the simplicity of the temperature prediction model.

4.2.2 Temperature Prediction Algorithm

Since the position of each camera is fixed and known based on the design of the housing described in Chapter 3 a function was derived to map the two images onto one another. Mapping the visible light image to the reference frame of the IR camera allows the images to be directly compared. This is demonstrated in Figure 4-12 which shows the transformation performed on the visible light image.

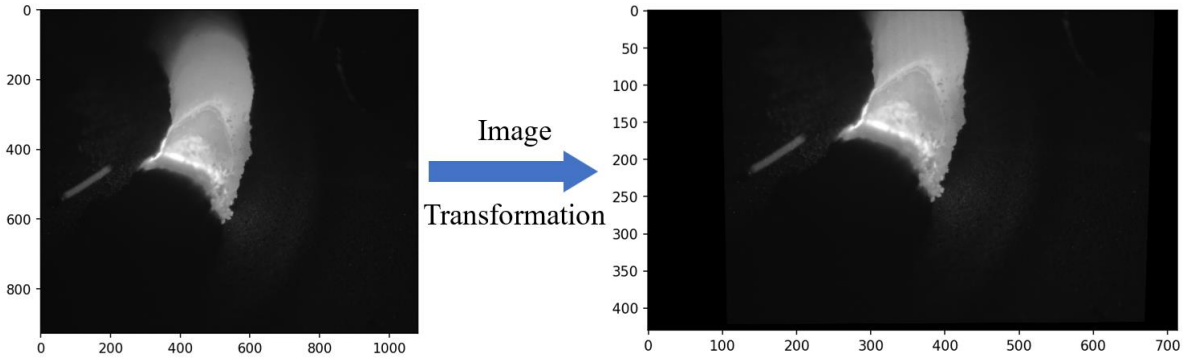

Figure 4-12 Image transformation mapping the visible light image to the reference frame of the infrared image

The image transformation shown in Figure 4-12 allows the visible light image to be directly compared to the temperature distribution measured by the infrared camera. An affine transformation was used in this case since it includes operations like scaling, rotation, translation, and shearing, preserving collinearity and parallelism in the transformed image. Interpolation was utilized to determine the intensity values of the newly mapped pixels. It is also noteworthy that the resolution of the image has changed to ensure the size of both images is identical. By overlaying both images a 3-dimensional matrix was formed, with the x and y dimensions of the matrix representing the size of the images. The z-axis had 2 elements which represent the intensity measured by the vision camera and the temperature distribution. Effectively, this matrix shows that for each pixel of the transformed vision image there is an intensity and corresponding temperature. Figure 4-13 shows the relationship between the intensity and temperature for the frame shown in Figure 4-11, where each data point of the scatter plot represents one pixel. Graphically demonstrating this relationship shows that a function was used to find the regression approximation of temperature based on the intensity measurements. Therefore, at each timestep this relationship was plotted, and a function was fit to approximate the temperature. This process was repeated for all 2264 timesteps and the average coefficients were calculated to create the piecewise regression model which is plotted below in red. While creating the regression models, a RANSAC model was used to reduce the influence of outliers.

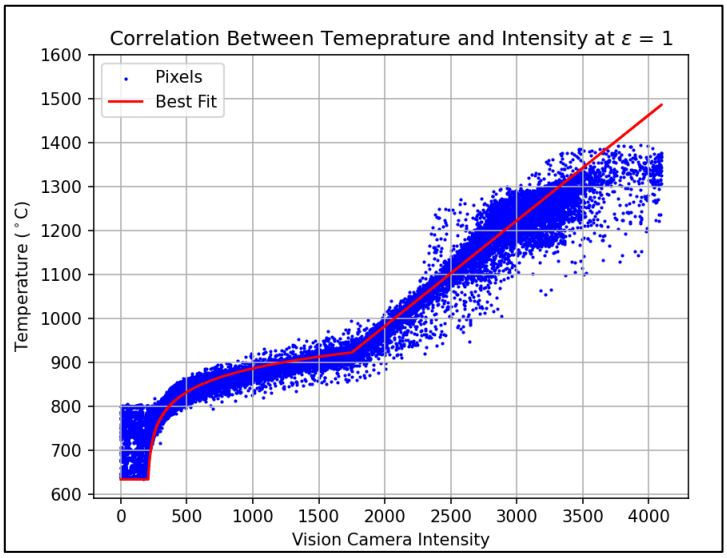

Figure 4-13 Relationship between visible light intensity and temperature

It is clear from the regression function in Figure 4-13 that there are 3 distinct regions used to approximate the temperature. These regions are determined by the performance of the visible light

camera sensor and Planck's law. To understand how Planck's law influences the intensity of light based on temperature, the radiance was plotted against temperature as in Figure 4-14 by using Eq. (4.4) with a wavelength of 850 nm, the bandpass filter used on the visible light camera, as explained in Section 3.4.

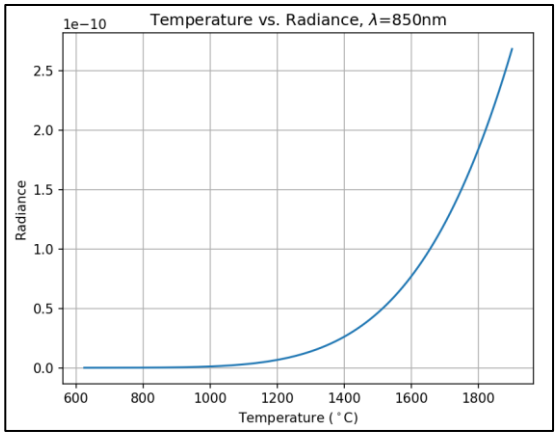

Figure 4-14 Temperature vs. Radiance, λ=850nm

The performance of the visible light sensor, produced by Photonfocus, is based on a proprietary function, known as LinLog, which increases the dynamic range of their camera sensors [107]. The LinLog technology from Photonfocus allows a logarithmic compression of high light intensities inside the pixel. At low intensities each pixel shows a linear response, while at high intensities the response changes to logarithmic compression. A diagram of the performance of this algorithm is provided in Figure 4-15.

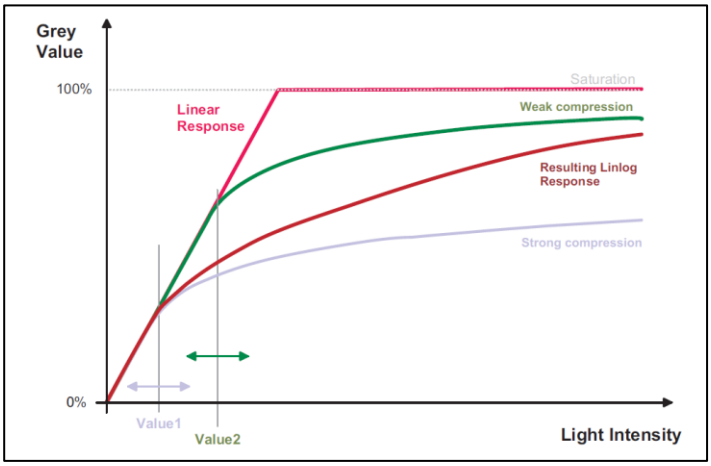

Figure 4-15 LinLog response curve to increase the dynamic range of CMOS camera sensor

Understanding the graphs in Figure 4-14 and Figure 4-15 explains the functions used to approximate the temperature based on camera intensity. Planck's law shows that intensity increases exponentially with temperature for the range that is studied in this research. At higher intensity values the response curve of the camera sensor is logarithmically related to the intensity of light. Hence, at higher intensities the function to map intensity to temperature is linear since the logarithm function and exponential function are inverses. However, for lower intensity regions, the camera sensor has a linear response, resulting in a logarithmic function being used to approximate temperatures, as it is the inverse of the exponential relationship shown in Figure 4-14. Finally, at intensities close to zero a constant temperature is assumed. This is related to the black level of the camera, which is the average image value at no light intensity.

Transforming the visible light images to the IR reference frame and then applying the piecewise function plotted in Figure 4-13 results in two temperature profiles with the same FOV. One profile from the IR camera, and the other from manipulating the visible light image. These images were directly compared and the MAPE was computed for all 2294 frames, resulting in a MAPE of 6.27% over the entire dataset.

4.2.3 Utilizing Pyrometer Measurements to Calibrate Temperature Distribution

To derive the previously obtained function, it was assumed that light emitted from the HAZ is captured by both camera sensors with perfect efficiency. Where the temperature measurements were captured from the Optris PI08M camera at 800 nm and the visible light images were captured with the Photonfocus D1312 sensor at 850nm as described in Section 3.4. The plot in Figure 4-13 represents the ratio between these wavelengths as captured by their respective sensor. However, radiation properties, such as transmissivity and emissivity affect the temperature measurements and should be accounted for. Furthermore, this method is not sufficiently accurate to be considered a robust calibration method. This motivates the addition of a pyrometer to be used to provide calibrated temperature measurements of a small region of the melt pool which are then used to scale the previously observed temperature distribution.

To account for the effect of the radiation parameters (emissivity and transmissivity) the experiment was repeated in which laser deposition of metal based on the AM layer-by-layer approach was applied onto a 6.3 mm substrate of 1018 cold-rolled steel with a laser spot diameter of 3 mm. Three layers of a thin-walled cylinder were produced using 106 μm type 431 stainless steel powder with a flow rate of

3.25 g/min. Each layer had a diameter of 24 mm, and the process parameters were a laser power of 1 kW and a scanning speed of 1.5 mm/s. In this experiment, the IR camera captured images with an emissivity value of 0.2 since this resulted in a maximum temperature in the HAZ of 1474 °C which is approximately the melting point of 431 stainless steel [119].

To account for the radiation parameters in the visible light temperature prediction, Planck's law is implemented to determine the relationship between the predicted temperatures from the 850 nm camera sensor and the actual temperatures of the HAZ. When working with short wavelengths of light, the Wien approximation, Eq. (4.5), can be used to improve the computational efficiency of implementing Planck's law.

$$I(v,T) = \frac{2hv^3}{c^2}\exp\left(-\frac{hv}{k_B T}\right) \tag{4.5}$$

Where I is the amount of energy emitted per unit surface area per unit time for a frequency of light, v, at absolute temperature, T. Calculating the percent error between Planck's law and the Wien approximation with a wavelength of 850 nm over the temperature range of 625 to 1900 °C results in an average percent error of 0.00733%. Since the accuracy of the infrared camera is reported to be 1% [106], the implementation of this approximation is found to be reasonable. Thus, to improve the computational time of the radiation efficiency approximation the Wien approximation is used for all future calculations. The Wien approximation can be further modified into Eq. (4.6) by accounting for the radiation efficiency:

$$I(v,T) = \varphi(v,T)\frac{2hv^3}{c^2}\exp\left(-\frac{hv}{k_B T}\right) \tag{4.6}$$

where φ, the radiation efficiency, is defined as the product of emissivity, ϵ, and transmissivity, τ, since these terms reduce the amount of light captured by the sensor:

$$\varphi(v,T) = \epsilon(v,T) \times \tau(v,T). \tag{4.7}$$

To account for the radiation efficiency, suppose that the true temperature of a region is known, then the approximate temperature calculated in Section 4.2.2 can be related to the true temperature with:

$$\frac{2hv^3}{c^2}\exp\left(-\frac{hv}{k_B T_{approx}}\right) = \varphi(v,T)\frac{2hv^3}{c^2}\exp\left(-\frac{hv}{k_B T_{real}}\right). \tag{4.8}$$

Where T_{approx} is the absolute temperature of some region based on the intensity measurements of the visible light camera and T_{real} is the real temperature of that region. Only the radiation efficiency at

850nm, φ_{850}, must be considered because of the narrow bandpass filter in the optical path; hence, Eq. (4.8) becomes:

$$\exp\left(-\frac{hv_{850}}{k_B T_{approx}}\right) = \varphi_{850} \exp\left(-\frac{hv_{850}}{k_B T_{real}}\right). \quad \textbf{(4.9)}$$

Finally, isolating for the radiation efficiency yields the following:

$$\varphi_{850} = \exp\left(\frac{hv_{850}}{k_B}\right) \times \exp\left(\frac{1}{T_{real}} - \frac{1}{T_{approx}}\right). \quad \textbf{(4.10)}$$

Utilizing a small region of the infrared camera measurements and approximating that as the area of a pyrometer can be used to provide calibrated measurements, representing T_{real}. Since the transformation matrix between the two camera sensors is known, it is trivial to find the corresponding region of the vision camera image. Figure 4-16a shows a temperature profile found from the infrared camera sensor, captured with an emissivity of 0.1 and transmissivity of 1, and Figure 4-16b shows the vision image captured simultaneously.

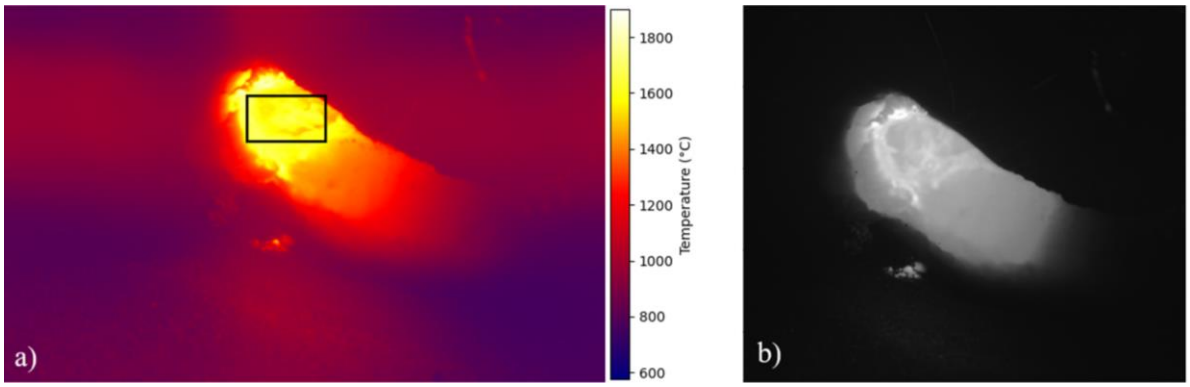

Figure 4-16 Simultaneously captured images to validate pyrometry calibration method a) temperature distribution from infrared camera with $\varphi = 0.1$ b) vision camera image

Implementing the algorithm derived in Section 4.2.2 results in the temperature distribution shown in Figure 4-17 from the image Figure 4-16b. Where the corresponding location of the pyrometer is shown in Figure 4-17. The location of the pyrometer was selected to be the center of the melt pool since the center is the only reliable location in the cylindrical tool path. However, in other tool paths it may be optimal to position the pyrometer in a different location.

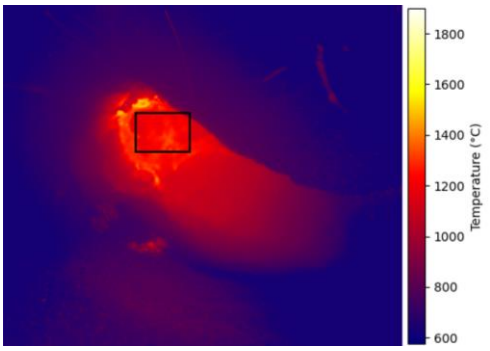

Figure 4-17 Implementation of temperature prediction algorithm

To determine the radiation efficiency, a region of the infrared image is selected to act as an approximated pyrometer, which is outlined in Figure 4-16a. Using the image transformation, the corresponding region can be found in the vision image coordinate system, which is outlined in Figure 4-17. T_{real} is assumed to be the average temperature of this region as calculated by the calibrated infrared image, which would perform similarly to a pyrometer. Therefore, T_{approx} is the average temperature of the corresponding region of the vision image after the temperature prediction algorithm is applied. With these values, Eq. (4.7) is then implemented to determine the radiation efficiency, a calculation that can be used at every timestep to monitor how the radiant properties are changing during the process, assuming the pyrometer measurements are accurate. For the specific timestep shown in Figure 4-16 these results are summarized in Table 4-4

Table 4-4 Radiation property comparison between temperature measurement and prediction

Variable Name	Value
T_{real}	1573.3 °C
T_{approx}	1226.5 °C
φ_{850}	0.11998

Rearranging Eq. (4.9) allows for T_{new} to be isolated, which is the temperature prediction from the vision camera image scaled based on the radiation efficiency φ_{850}:

$$T_{new} = \frac{1}{\frac{k_B}{hv_{850}}\ln(\varphi_{850}) + \frac{1}{T_{approx}}} \tag{4.11}$$

Inputting Figure 4-17 into Eq. (4.11) yields the new temperature distribution below.

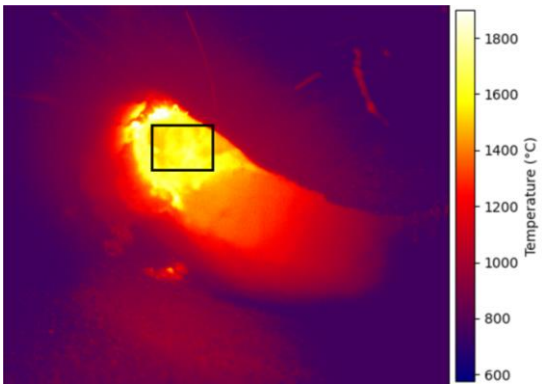

Figure 4-18 Temperature distribution scaled by calibrated pyrometry measurements

Examining Figure 4-18, T_{new} has an average temperature of 1573.9 °C over the area used to approximate the location of the pyrometer, which is outlined in the figure.

To validate the temperature prediction algorithm, the predicted temperature distribution, as shown in Figure 4-18 is transformed to the reference frame of the IR camera. The difference between the images was then computed to determine the error in the prediction algorithm. A visual representation of the error between the measured and predicted temperatures for this frame can be seen in Figure 4-19.

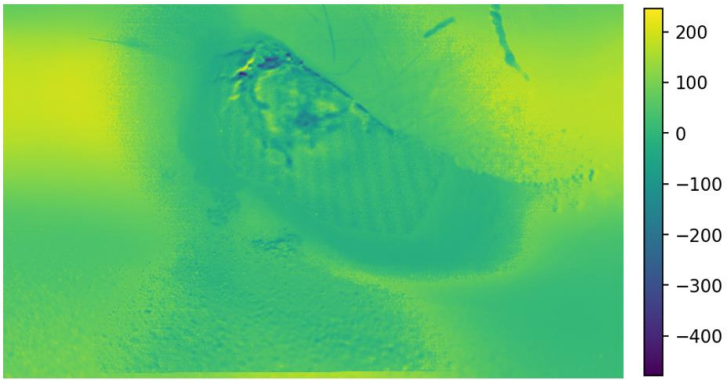

Figure 4-19 Error between measured and predicted temperature distribution

Figure 4-19 corresponds to a MAPE of 6.47%, calculating the error against this entire data set reveals the performance of the temperature prediction algorithm, which is a MAPE of 6.71%.

The phase changes of stainless steel, which influence the material properties, are dependent on the solidification of the clad. Hence, the most critical temperatures to monitor are below 1400 °C since this would correspond to solid region of the HAZ. At lower temperatures, the light radiated from the HAZ is insignificant compared to the light reflected from higher temperature regions. This is due to the

performance of the camera sensor; therefore, measured temperatures below 800 °C are likely caused by reflected light and not radiation. The portion of the HAZ that is within the range 800 to 1400 °C is highlighted in green below in Figure 4-20.

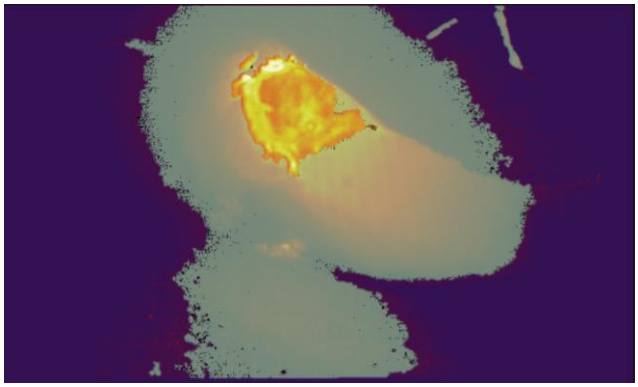

Figure 4-20 HAZ with the 800 to 1400 °C temperature region highlighted

Analyzing this temperature range results in a MAPE of 1.01% at this current timestep and a MAPE of for the entire dataset. A summary comparing the performance of temperature prediction for the entire image and the temperature range from 800 to 1400 °C is displayed in Table 4-5.

Table 4-5 MAPE of temperature prediction for type 431 stainless steel

	Entire Image	**800 to 1400 °C**
Current Timestep	6.47	1.01
Entire Dataset	6.71	1.05

The difference in performance of the different temperature ranges demonstrates that the temperature prediction algorithm is less capable of calculating the extreme temperatures of the HAZ but is accurate at the intermediate temperature values. At higher temperatures, a higher deviation may be caused by the rapid changes in emissivity and the amount of oxidation present as the material solidifies. While the deviation at lower temperatures may be caused by the limitations of the camera sensor, such as the lens flare that is visible in the IR sensor, as shown in Figure 4-16a. Lens flare occurs when light enters the lens at an angle that is outside the desired path, resulting in reflections, internal scattering and unwanted artifacts. In this case, these reflections are caused by the brightness of the melt pool, in contrast to the dark surrounding area.

4.2.4 Estimating Temperature Distribution of Different Materials

To verify that the temperature prediction algorithm is capable of measuring temperatures of different materials, LDED experiments were conducted with Inconel 625 powder. Inconel Alloy 625 (UNS N06625) is a nickel-based superalloy that possesses high strength properties and resistance to elevated temperatures, with composition shown in Table 4-6. Since 431 stainless steel is an iron-based alloy and Inconel 625 is a nickel-based alloy, demonstrating that the temperature prediction is accurate for these different materials shows that the algorithm is invariant to material properties.

Table 4-6 Composition of Inconel 625

Element	Weight %
Ni	58.0 min.
Cr	20.0 - 23.0
Fe	5.0 max.
Mo	8.0 - 10.0
Nb (+ Ta)	3.15 - 4.15
C	0.10 max.
Mn	0.50 max.
Si	0.50 max.
P	0.015 max.
S	0.015 max.
Al	0.40 max.
Ti	0.40 max.
Co	1.0 max.

During these experiments, data was acquired during laser deposition of metal based on the AM layer-by-layer approach onto a 6.3 mm substrate of 1018 cold-rolled steel with a laser spot diameter of 3 mm. Three layers of a thin-walled cylinder were produced using 60 µm Inconel 625 powder with a flow rate of 3.5 g/min. Each layer had a diameter of 24 mm, and the process parameters were a laser power of 1 kW and a scanning speed of 1.5 mm/s. A cylindrical part was developed to ensure greater variation in the captured images than with a linear clad and is consistent with the experiments conducted with type 431 stainless steel powder. Inconel 625 was selected as a different material to test since it is a nickel-based alloy and therefore has different material properties than the previously tested 431 stainless steel powder, while still having a melting point of approximately 1300 °C, which is within the measurement range of the MOC sensor. During this experiment the emissivity of the IR camera was set to 0.15 to adjust the temperatures to the desired range.

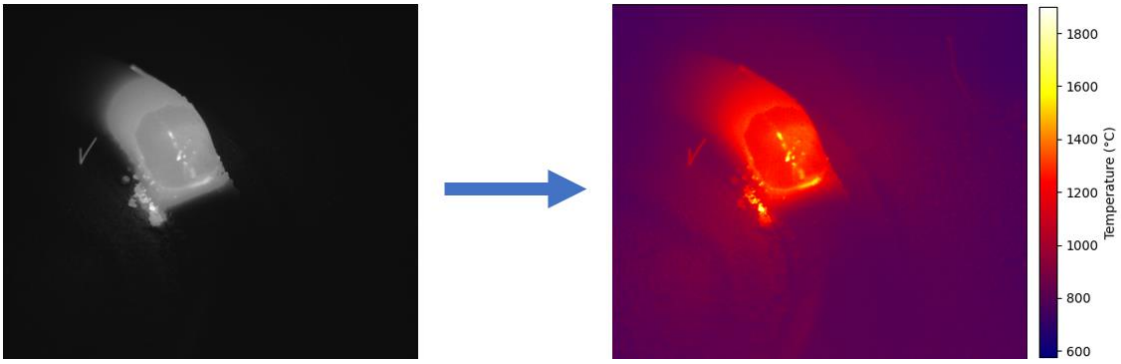

Figure 4-21 Visible light image captured during LDED with Inconel 625 and transformed to predict temperature

Comparing the temperature distribution captured with the IR camera and the predicted temperatures from the visible light with Inconel 625 powder results in a MAPE of 2.91% over the entire image and 0.90% for temperatures from 800 to 1300 °C. Where 1300 °C was selected as the upper limit of this range since it is approximately the melting point of Inconel 625.

4.2.5 Estimating Temperature Distribution with a Coaxial Field of View

To demonstrate the capabilities of temperature prediction with a different optical setup, LDED experiments were conducted with Inconel 625 powder. During these experiments, data was acquired during laser deposition of metal based on the AM layer-by-layer approach onto a 6.3 mm substrate of 1018 cold-rolled steel with a laser spot diameter of 3 mm. Three layers of a thin-walled cylinder were produced using 60 µm Inconel 625 powder with a flow rate of 3.5 g/min. Each layer had a diameter of 24 mm, and the process parameters were a laser power of 1 kW and a scanning speed of 1.5 mm/s. Figure 4-22 shows the MOC sensor attached to the LMP apparatus in the ALFa laboratory positioned with a coaxial FOV. With this setup the lens was changed to a 125mm focal length achromatic lens to compensate for the different optical path. Again, in this experiment a cylindrical laser path was chosen to be consistent with the previous runs. The emissivity value of the IR camera was set to 0.15, just as in the previous experiment and the transmissivity was set to 0.5 to account for the laser mirror, with transmission properties shown previously in Figure 3-10.

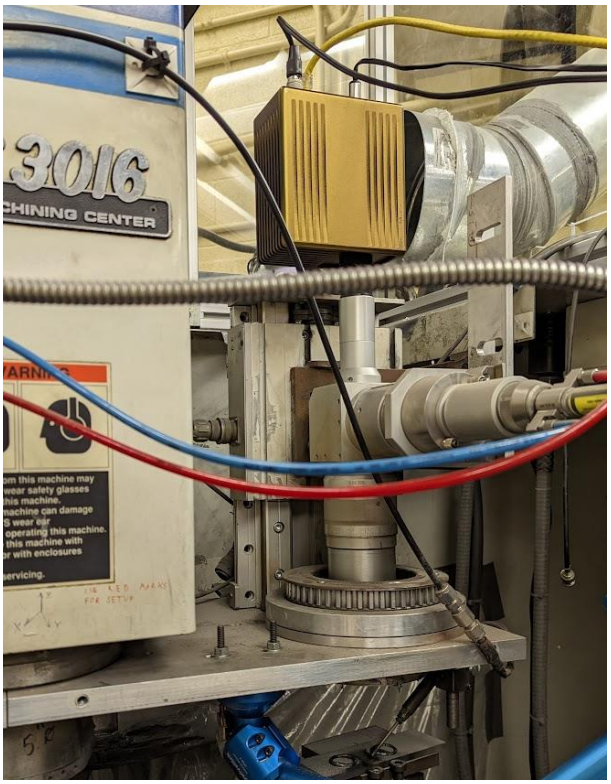

Figure 4-22 MOC sensor positioned in the ALFa laboratory with a coaxial field of view

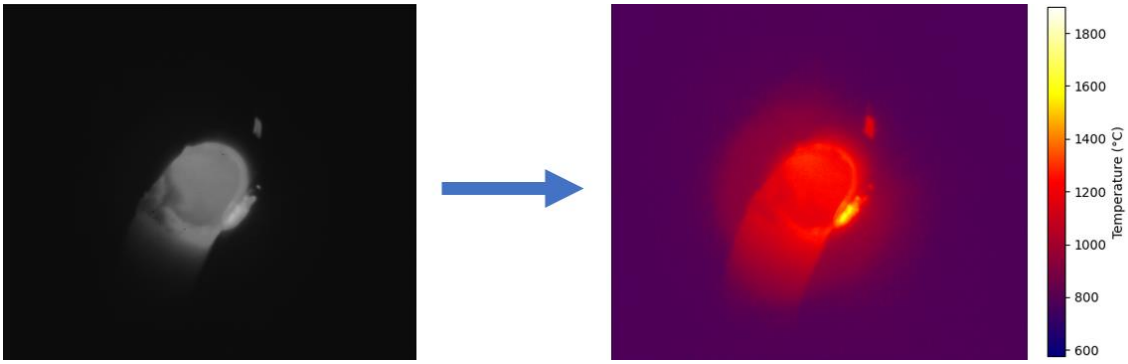

Figure 4-23 Visible light image captured coaxially during LDED with Inconel 625 and transformed to predict temperature

Figure 4-23 shows the original visible light image and the temperature distribution found after applying the transformation for one frame of the coaxial Inconel 625 data. Comparing the temperature distribution captured with the IR camera and the predicted temperatures from the visible light with Inconel 625 powder results in a MAPE of 3.13% over the entire image and 0.75% for temperatures from 800 to 1300 °C.

4.3 Summary

This chapter discussed two algorithms used to estimate the temperature of the HAZ during thermal processes in real time with an uncalibrated CMOS camera and a pyrometer. The first algorithm utilizes a discrete difference model of the HAZ derived from the generalized heat conduction equation. The model approximates the HAZ as a nodal network where conduction between each node is calculated based on assumed material properties. Data from the CMOS images and process parameters (the laser power and scanning speed) were used as inputs to a gradient boosted trees ML algorithm to estimate the temperature of the outer most nodes of the HAZ. While the pyrometer measurement at the center of the melt pool was another boundary condition used to solve for the intermediate temperatures of the HAZ. This model was able to estimate temperatures with a MAPE of 11.3%. However, many approximations were made to create the model used in this calculation and since the material properties and input energy are used in the calculations, this model cannot be used liberally in thermal processes.

To improve the temperature predictions, an HDR CMOS camera was used to capture the intensity of a larger area of the HAZ without oversaturating the sensor. With the higher dynamic range, a dataset was developed during LAM that featured images captured with a CMOS camera and IR camera. This allowed a regression model to fit the intensity values captured by the CMOS camera to the corresponding temperature measurements. Moreover, using the temperature of the center of the melt pool captured by the IR camera simulated the performance of a pyrometer fixed to that location. Integrating these real-time pyrometer measurements to the temperature distribution found by the regression model allowed for the temperatures distribution to be adjusted based on the calibrated measurements from the pyrometer. Therefore, this created a model that estimated temperature that is invariant to material properties and input energy. Furthermore, this model was validated with both 431 stainless steel and Inconel 625 to prove its effectiveness at predicting the temperature distribution of materials with different thermal characteristics and with lateral and coaxial FOVs to demonstrate the effectiveness with different optics. Ultimately the temperature predictions resulted in a MAPE of less than 7% when compared to temperatures measured with an IR camera. Moreover, the error of temperature measurements in the critical transformation ranges was shown to be < 2%, which is more accurate than the models described in Section 2.3.2, which reported approximately 3% error.

Chapter 5
Imaging Based Geometry Measurements

Geometry is an important feature in thermal processes, which directly impacts the quality, functionality, and performance of the final part. Deviations in geometry can lead to dimensional inaccuracies, structural weakness, thermal warpage, and other defects that may affect the integrity of the component. Moreover, monitoring the geometry provides valuable feedback for process optimization by identifying areas of improvement and determining if process parameters should be adjusted. Therefore, monitoring and controlling the geometry throughout the process is essential in ensuring the final product meets the required specifications. The geometry monitoring methodologies described in this chapter serve as the foundation upon which geometry control and quality assurance tools can be implemented.

5.1 Single-Track Deposition Geometry

In thermal processes, the geometry of the deposited material (clad) is directly related to the quality of the final part. Unlike subtractive manufacturing techniques, the geometry is susceptible to process variation and cannot be directly controlled. Consequently, these products must be verified after manufacturing to determine if the geometry is within specifications. To enhance quality assurance in LDED, there is a need for an in-situ monitoring system capable of real-time measurement of clad geometry. Therefore, this methodology describes how the MOC system was used to measure the geometry of the clad in real-time during LDED.

5.1.1 Geometry Prediction Algorithm

In manufacturing a single clad, the geometry is defined by the height and width of the single track. A lateral orientation of the MOC sensor allows for the height and width of the deposited material to be measured, however these features cannot be observed directly, as shown in Figure 5-1. Only the measurement *d* shown in the image can be directly observed, therefore, the exact geometry of the clad must be calculated based on this observed measurement and assumptions regarding the shape of the deposition. Figure 5-1 also demonstrates the position of the camera relative to the deposition, where the displacement between the laser spot and the camera remains constant and the direction of deposition must be perpendicular to the page.

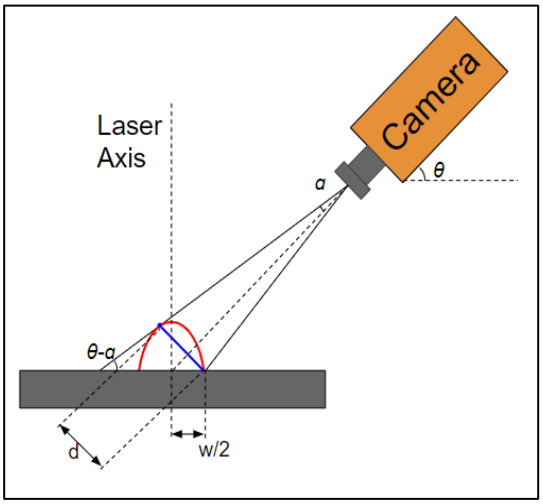

Figure 5-1 Schematic of the camera field of view, in this figure the scanning direction is perpendicular to the page and the camera has a side view of the melt pool.

The assumptions necessary to determine the geometry of the clad are:

1. The center location of the laser is always known, since the camera is fixed to the laser head the location of the center of the laser is fixed in the camera's FOV. The MOC sensor should be mounted at a fixed location relative to the thermal processing machine and calibrated to ensure the center of the heat source is known within the FOV.
2. The clad is symmetric about the laser axis and since the location of the center of the laser is known, and the bottom of the clad is found via image thresholding, *w/2* can be determined from the location of the camera. Assuming ideal powder flow and a symmetric laser power distribution, then the clad should form symmetrically as well since this algorithm is for single-track depositions.

The slope of the tangent of the upper edge of the clad is parallel to the angle of the center axis of the camera's FOV. Visually, this is represented in Figure 5-1

3. Figure 5-1 as $\theta + \alpha \approx \theta$, which is valid because the camera is positioned approximately 250mm from the melt pool and the melt pool is approximately 2mm wide, the angle $\alpha \approx 0.3°$
4. Two measurements are observable, the distance *d* and *w/2*, which are further discussed below.
5. The general shape of the clad is a circular arc, which was shown experimentally in [120]. While in the liquid phase, the surface tension of the melt pool conforms to this shape to reduce the surface area. If there is sufficient power to melt the powder, then the cross-section of the deposition should approach a circular arc.

6. The direction of deposition is always perpendicular to the center axis of the camera's FOV. This is also shown in Figure 5-1, where the direction of travel is perpendicular to the page.

The critical measurements of *d* and *w/2* are extracted from both the vision camera and IR camera, since each sensor has a different spectral response, different features can be observed. Moreover, utilizing both measurements would reduce the influence of outliers and errors observed by one sensor. Figure 5-2 shows an image from the same time frame of LDED captured by each camera, the IR camera captures a larger dynamic range, while the vision camera has a higher resolution. The melt pool below has an area of approximately 18842 pixels in the vision image and 5102 pixels in the IR image.

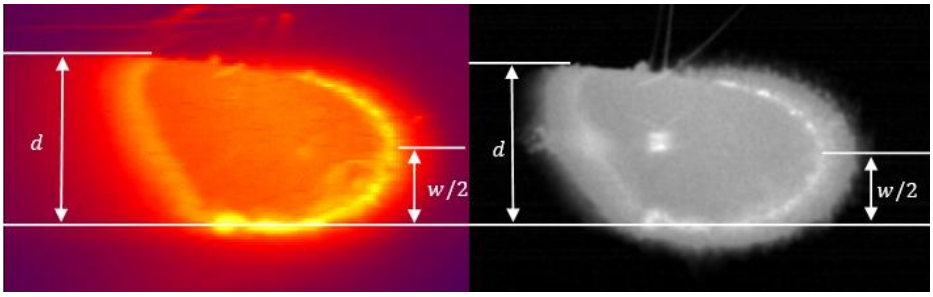

Figure 5-2 Typical images captured during LDED, with labels corresponding to the measurements needed to calculate the geometry of the clad

In Figure 5-3 below, the order of image processing steps is shown to demonstrate how the measurement for distance *d* is extracted from the vision camera image.

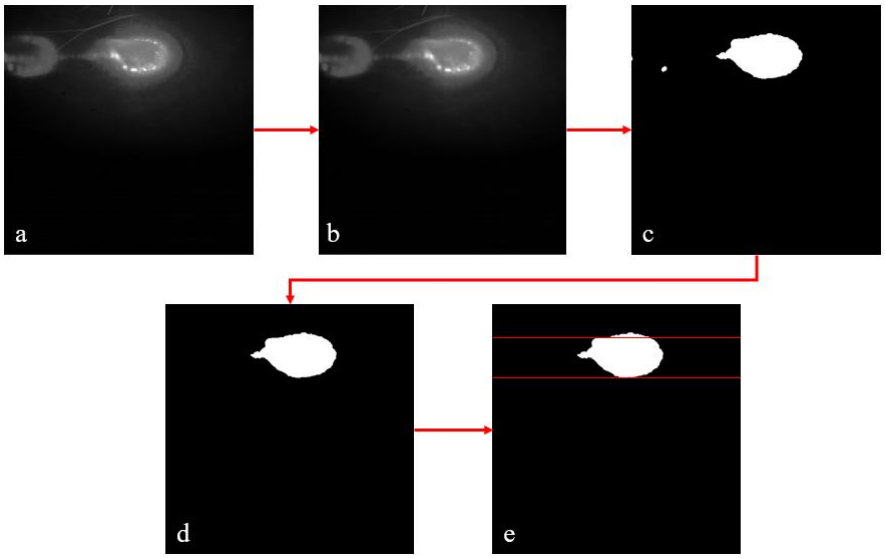

Figure 5-3 Image processing order of operations. (a) raw image, (b) box filter, (c) image thresholding, (d) remove artifacts, and (e) measure the distance *d*

Figure 5-3 depicts images captured by the vision camera; however, the same order of operations is conducted on the IR images as well and the results are averaged to improve performance. The first step of image processing is shown in Figure 5-3b, which depicts a box filter applied to reduce the noise. Applying a box filter reduces the noise captured by the camera sensors and reduces the impact of outliers of pixel intensity. Figure 5-3c demonstrates the effect of thresholding the image, where a technique devised by Ranefall thresholds objects based on their size [121]. The final image processing step is shown in Figure 5-3d, where any undesired artifacts, which may be caused by spatter or internal reflections, are removed from the image since the largest object is assumed to be the true melt pool. Finally, applying these processes allows for the top and bottom edges of the melt pool to be observed as shown in Figure 5-3e. Where the distance between these lines is d and was converted from pixels into millimeters based on the camera's working distance and optics.

The cross-section of the deposition is shown in Figure 5-4, where the clad is outlined in blue and is approximated by a circular cross section as in [120] and the green line corresponds to the distance d. The laser, which is highlighted in red is assumed to be at the middle of the deposition, because of the symmetric assumption and the x-axis of the diagram corresponds to the surface of the substrate. P1 is the location where the slope of the clad is equal to the angle of the MOC system and P2 corresponds to where the edge of the clad meets the substrate. Therefore, with the assumed shape of the deposition, the distance d found from the process outlined in Figure 5-3, and the angle of the MOC sensor, θ, known, the points P1 and P2 can be found to determine the approximate cross-section of the clad.

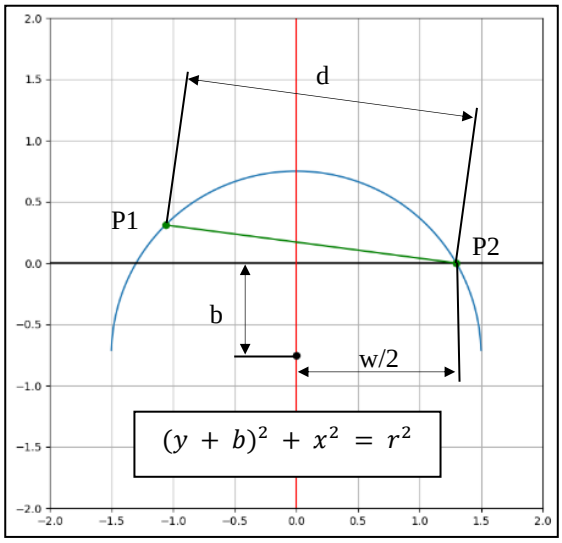

Figure 5-4 Assumed cross-section of the deposition

Since the location of the laser center is known, the width of the clad can be measured directly based on the angle of the camera, θ, and the distance, d_w, shown in the schematic diagram Figure 5-5. Additionally, Figure 5-6 shows a sample of how the distance, d_w, is measured from a captured frame. Moreover, the working distance of the camera and the optics allow this measurement to be converted from pixels into millimeters, which is more appropriate for real time melt pool measurements.

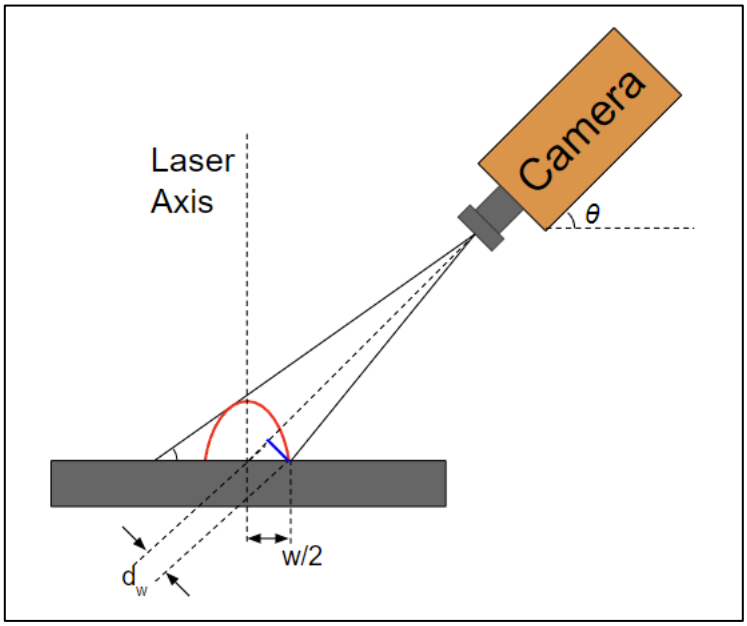

Figure 5-5 Schematic diagram showing width of the melt pool relative to the center position of the laser

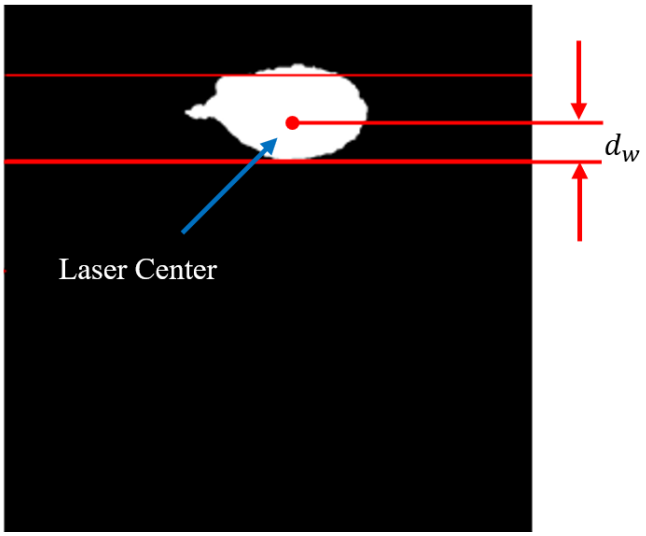

Figure 5-6 Width of the melt pool relative to the center position of the laser

Therefore, the relationship between this measured distance (d_w), the camera angle, and the width of the melt pool is:

$$\frac{w}{2} = \frac{d_w}{sin\theta} \tag{5.1}$$

This relationship is also related to the location of P2, shown in Figure 5-4, which is given as:

$$P2\ \left(\frac{w}{2}, 0\right) \tag{5.2}$$

To determine the other variables, the equation shown in Figure 5-4 was rearranged into a function, such that all x values in its domain correspond to one y value:

$$y = +\sqrt{r^2 - x^2} - b \tag{5.3}$$

where x is the independent variable, y is the dependent variable, r is the radius of the circle, and b is the y-coordinate of the center of the circle. The coordinates of P2, shown in Eq. (5.2), and the general equation of a circle can be used to form the following relationship between b and r:

$$b = \sqrt{r^2 - \left(\frac{w}{2}\right)^2} \tag{5.4}$$

P1 was analyzed to determine another, independent, equation that also relates the values of b and r. Thus, with two independent equations these values were computed. The tangent line of point P1 must be equal to angle of the camera, since P1 is the highest observable point of the melt pool, as shown in Figure 5-1. Hence, to determine the coordinates of this point, the derivative of Eq. (5.4) must be found, which is given by:

$$\frac{dy}{dx} = -\frac{x}{\sqrt{r^2 - x^2}} \tag{5.5}$$

Eq. (5.5) is related to the angle of the camera, with the following relationship:

$$-\frac{x}{\sqrt{r^2 - x^2}} = tan\theta \tag{5.6}$$

Rearranging to find the x-coordinate of P1 results in the following equation:

$$x = \sqrt{\frac{r^2}{1 + \tan^2\theta}} \tag{5.7}$$

Substituting the x-coordinate in Eq. (5.7) into the general equation of the circle, Eq. (5.3), yields the y-coordinate of P1. Therefore, the coordinates of point P1, shown in Figure 5-4 are given by:

$$\text{P1}\left(\sqrt{\frac{r^2}{1+\tan^2\theta}}, \sqrt{\frac{r^2\tan^2\theta}{1+\tan^2\theta}} - b\right) \tag{5.8}$$

With the locations of P1 and P2 known, Pythagorean theorem was implemented to relate these parameters to the distance d, which was directly measured from the camera.

$$\sqrt{\left[\left(\frac{w}{2} + \sqrt{\frac{r^2}{1 + \tan^2\theta}}\right)^2 + \left(\sqrt{\frac{r^2\tan^2\theta}{1 + \tan^2\theta}} - b\right)^2\right]} = d \tag{5.9}$$

Finally, with the equation of the cross-section of the clad found with the above relationships, the height of the clad can be calculated with the following equation:

$$h = r - b \tag{5.10}$$

These equations can be used at any timestep to calculate the corresponding height and width of the clad by assuming the general shape of the cross-section to be a circle and using measurements directly captured with the camera. However, with this methodology, there are boundary conditions shown in Figure 5-7 that must be considered as well, to demonstrate the limitations of this geometry prediction.

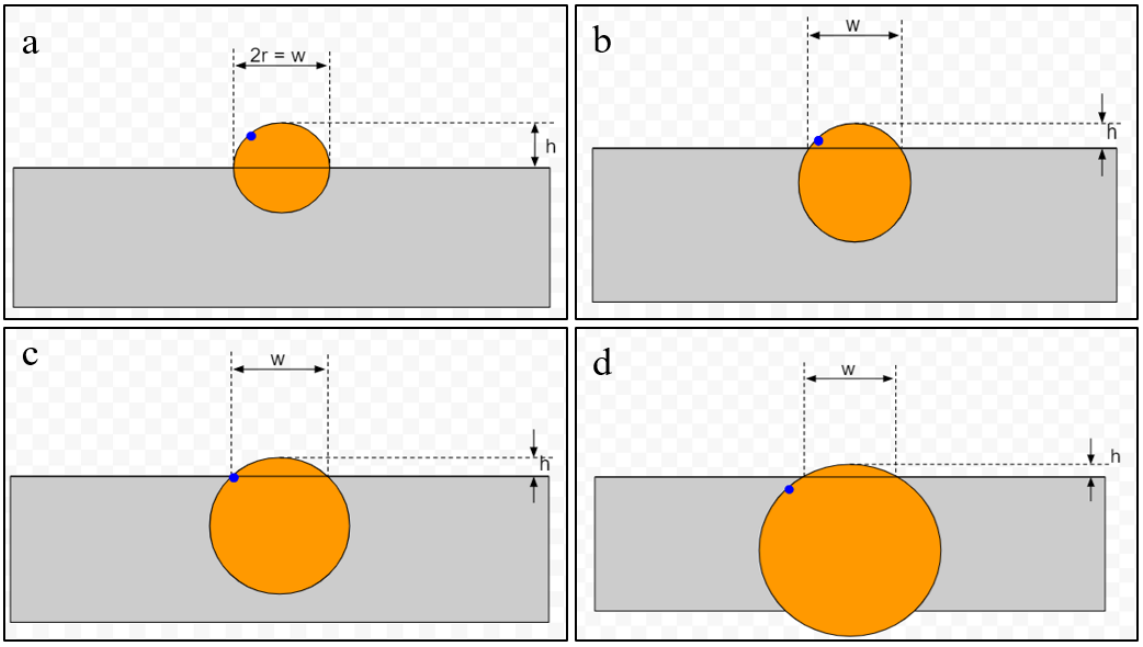

Figure 5-7 Clad cross-section boundary conditions (a) maximum height, (b) intermediate height, (c) minimum height, and (d) height too small to measure

Assuming a constant width, Figure 5-7 demonstrates four cases that must be considered when implementing this prediction. The orange circle represents the circular cross-section of the clad, the gray rectangle is the substrate, and the blue point is the point where the slope is parallel to the camera angle (P2 from Figure 5-4). The maximum height observable corresponds to when the center of the circular cross-section coincides with the surface of the substrate as shown in Figure 5-7a, in this case,

$$h = r = \frac{w}{2}. \tag{5.11}$$

Figure 5-7c represents the minimum measurable height; this occurs when the point on the circular arc that is tangent to the camera is coincident to the surface of the substrate. The intermediate case Figure 5-7b is between these boundary conditions and is when the height can be computed directly. The height in the last case, Figure 5-7d, is not observable because the point where the tangent slope of the circular cross-section that is parallel to the center axis of the camera's FOV is below the surface of the substrate, in this case the height of the substrate is assumed to be the same as in (c), the lowest measurable height.

5.1.2 Evaluation of Single-Track Geometry Prediction

Nine experiments were conducted with various combinations of laser power and scanning speed to ensure that the geometry measurements remain accurate for all reasonable clad geometries during LDED. The experiments were conducted on a substrate of 6.3 mm 1018 cold-rolled steel with a laser spot diameter of 3 mm using 150 µm 316L stainless steel powder at a feed rate of 3g/min. Alloy 316L (UNS S31603) is a chromium-nickel molybdenum austenitic stainless steel with composition shown in Table 5-1.

Table 5-1 Composition of 316L stainless steel

Element	Fe	C	Si	Mn	P	S	Cr	Ni	N	Mo
Weight %	Balance	0.03	1.0	2.0	0.045	0.016	16.5 - 18.5	10.0 - 13.0	0.1	2.0 - 2.5

The process parameters for this set of experiments are outlined in Table 5-2 below.

Table 5-2 Details of experiments used to validate geometry measurements

Experiment Number	**Laser Power (W)**	**Scanning Speed (mm/min)**
1	950 (const.)	110 (const.)
2	850 – 1050 (ramp)	110 (const.)
3	850 – 950 – 1050 (step)	110 (const.)
4	950 (const.)	140 – 80 (ramp)
5	950 (const.)	140 – 110 – 80 (step)
6	850 – 1050 (ramp)	110 (const.)
7	850 – 950 – 1050 (step)	110 (const.)
8	950 (const.)	140 – 80 (ramp)
9	950 (const.)	140 – 110 – 80 (step)

Figure 5-8 demonstrates the performance of the geometry predictions, which are calculate using the methodology shown in Section 5.1.1, against the geometry measurements obtained through macro imaging of the deposition after manufacturing for experiment 1 in Table 5-2. Note the significant deviation in clad height despite the constant process parameters. The variation in geometry is also visible in the photograph taken of the clad after the process shown in Figure 5-9.

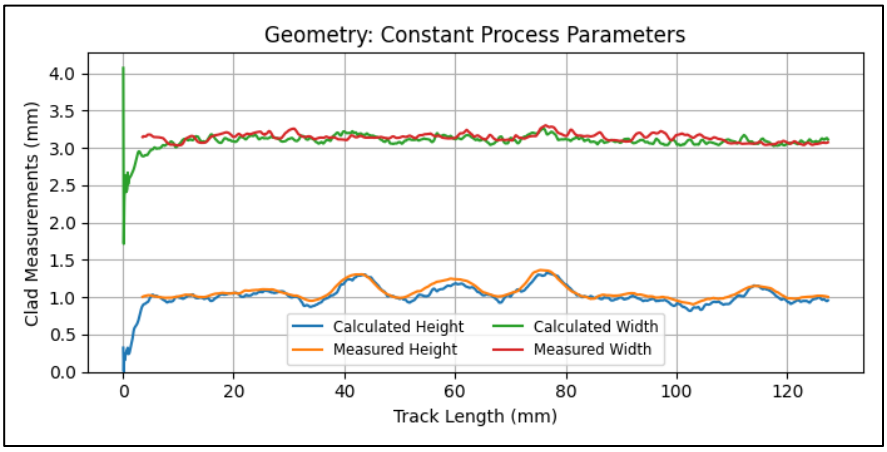

Figure 5-8 Demonstration of measured and calculated geometry for experiment 1

Figure 5-9 Photograph of the clad from experiment 1

Figure 5-10 show real-time data regarding the speed step experiment 5 outlined in Table 5-2 and Figure 5-11 shows a corresponding image of the clad. Note that the changes in height are visible in Figure 5-11 and the length of each section is not equal due to the changing speed, as the time for each section was kept constant.

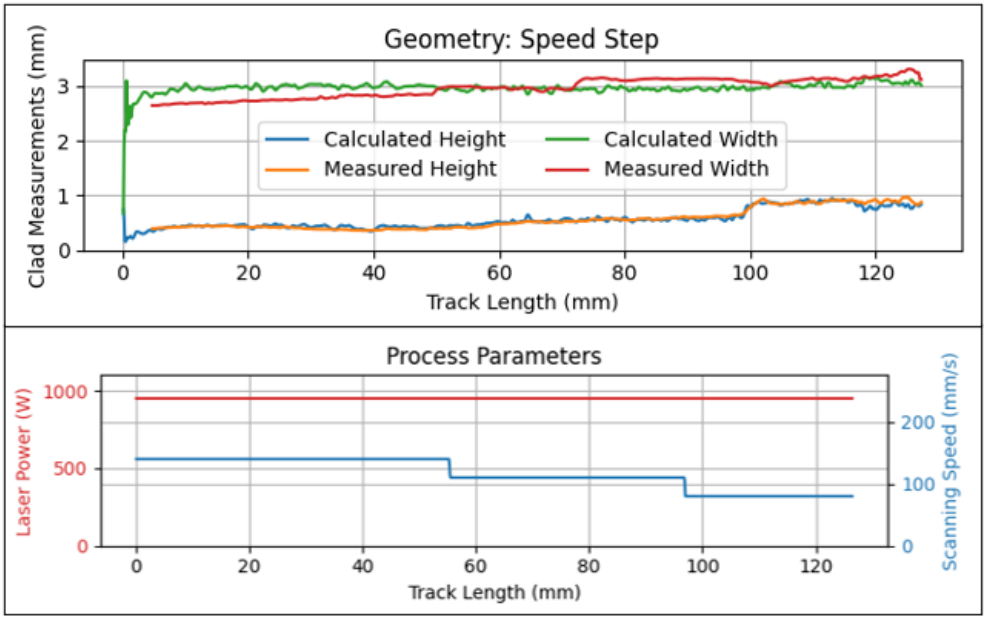

Figure 5-10 Predicted and measured geometry against process parameters for experiment 5

Figure 5-11 Photograph of the clad from experiment 5

Plotting the percent error of the predicted geometry is shown in Figure 5-12. The error of the height and width were shown to follow a normal distribution with a mean of 0.67% and standard deviation of 4.26% for the width calculation and mean of 3.06% and standard deviation of 8.49% for the height calculation. The MAPE for the features are 3.48% for the width and 6.58% for the height, respectively. Moreover, since there is more variation in the height calculation the R-squared value for the height was calculated to be 0.944, which indicates that the calculated height is strongly correlated to the measured height and is visualized in Figure 5-12c.

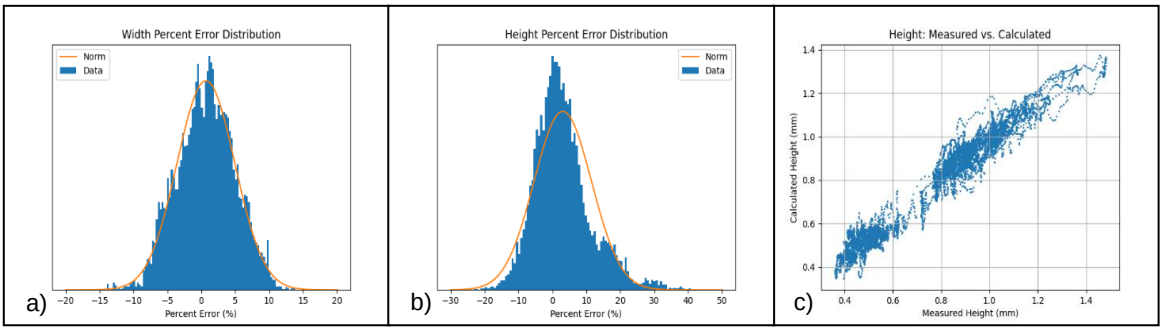

Figure 5-12 Error distribution of calculated geometry a) width error b) height error c) visualization of height estimation r-squared

5.2 Geometry Prediction of Thin-Walled Components Using Machine Learning

The previous geometry prediction is dependent on the shape of the clad and is limited to single-track experiments, which is relevant in welding and some laser cladding applications. However, AM requires multiple layers to be considered to have accurate geometry measurements during the entire process. In thin-walled components, where multiple layers are built directly on previous layers, the shape of the clad for each layer is different since it is influenced by the geometry of the previous layers. The difference in appearance of the clad captured with the visible-light sensor based on the layer is highlighted in Figure 5-13.

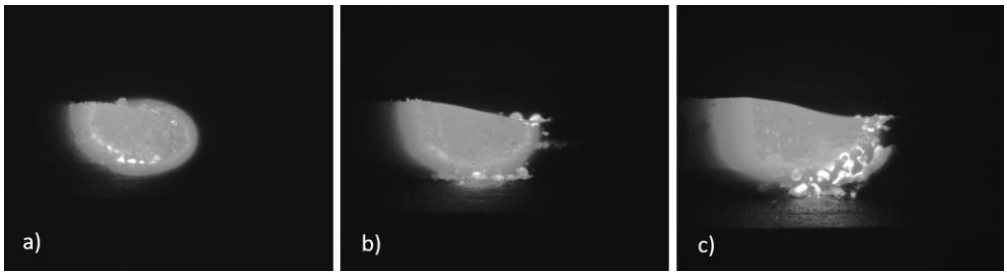

Figure 5-13 Visible light image captured in a) first layer, b) second layer, and c) third layer

This makes the previous approach difficult since assuming the shape of the clad breaks down for each layer. Therefore, an ML approach was used to compensate for the different appearance of each layer in thin-walled components. A convolutional neural network (CNN) was created to predict the height and width of the clad during thin-walled LDED in real-time using images captured by a vision camera and infrared camera. Training a CNN to solve this challenge removed the need to determine a direct relationship between the captured images and clad geometry which may differ based on the LDED system and materials used. Furthermore, a CNN is an appropriate choice for this application due to their efficiency at processing images and CNNs have already been used in literature to monitor various features in thermal processes.

5.2.1 Thin-Walled Geometry Prediction Algorithm

To predict the geometry (height and width) the CNN uses both the visible light and IR images captured with the MOC sensor and process parameters as inputs. Figure 5-14a shows a typical image of the clad captured with the visible-light sensor. Since the clad is only visible in a section of the image it is reasonable to crop the images to remove the background information, which has no indication of the geometry of the clad. Removing this background information also reduces the size of the dataset, which improves computational efficiency without sacrificing performance.

To reduce the size of the images the procedure shown in Figure 5-14 was followed. First, the image was thresholded to determine the approximate location of the center of the clad, which is shown in red in Figure 5-14b. After thresholding, the largest object in the frame (which should be the clad) is isolated to remove artifacts caused by spatter and other hazards. Based on this location, the image could be cropped to a reduced size of 254×254 pixels. Finally, to further reduce the size, the images were scaled to 128×128 pixels by averaging intensity values.

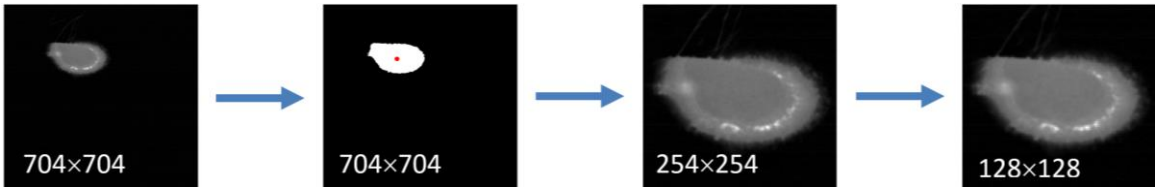

Figure 5-14 Series of pre-processing steps conducted on the vision images

The same procedure outlined in Figure 5-14 was used to reduce the size of the infrared images, except for scaling the images, since IR images were captured at a lower resolution. Therefore, once the location of the clad was approximated, the images were cropped directly into 128 × 128 as shown in Figure 5-15. Both images were also normalized to ensure that the intensity values of the pixels were at the same scale as the process parameters to improve the performance of the ML algorithm.

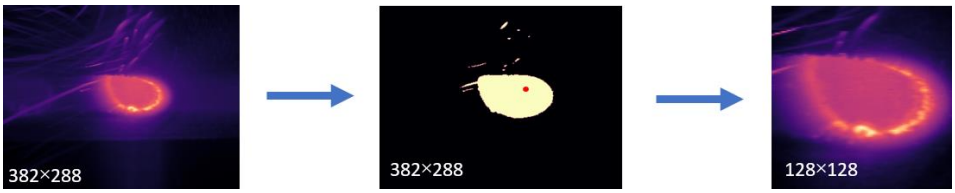

Figure 5-15 Series of pre-processing steps conducted on the IR images

The developed CNN was designed to predict the clad height and width from the 128×128 visible-light and IR images and process inputs of a laser cladding process. The process inputs used to augment the prediction are the laser power, scanning speed, and layer number, since these parameters all influence the geometry of the deposited material. The CNN was trained to minimize the mean squared error (MSE) between the predicted and actual clad geometry. The architecture of the CNN is shown in Figure 5-16.

This CNN architecture is made of two deep network branches, in which the IR images are the input for the first branch and the visible-light images are the input of the second branch. Each branch consists of four blocks of two conv layers with batch normalization and relu activation, and a maxpooling layer. After these four blocks, the branch output is flattened into a 1-dimensional array. After that, both branches are combined with the process laser power, process scanning speed, and the layer number. This combined layer is fed through two fully connected layers followed by a linear activation. The linear activation outputs the prediction of the clad height and width.

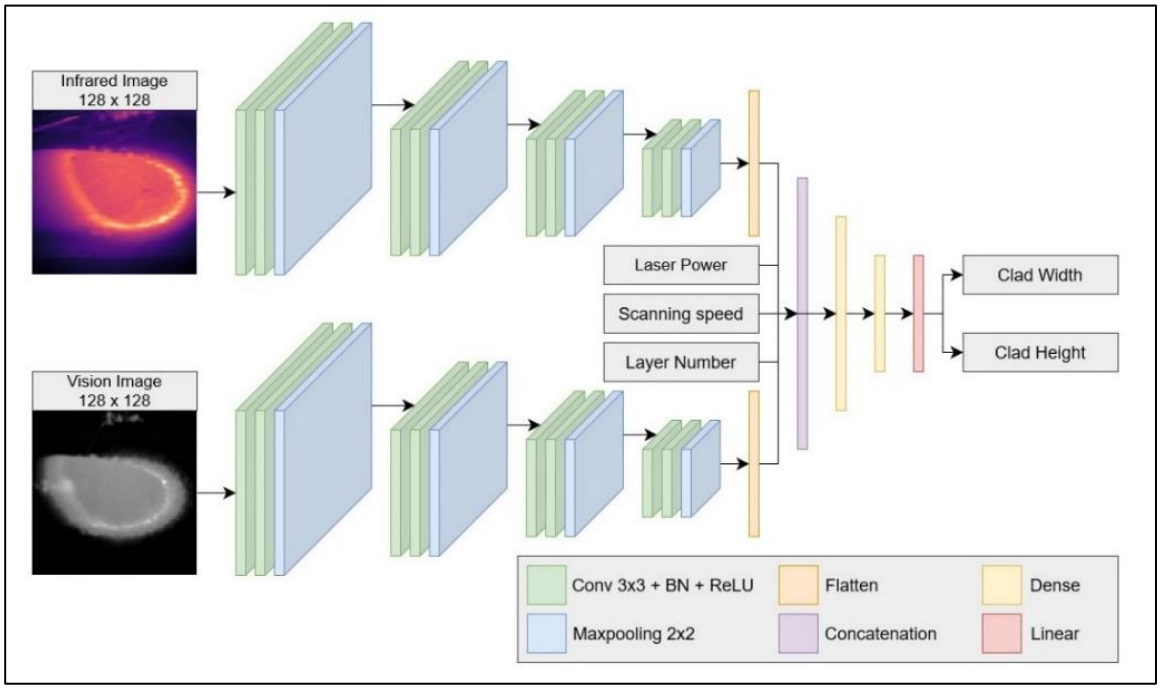

Figure 5-16: CNN architecture used to predict the clad with and clad height.

An important consideration when initializing the CNN is the loss function. The loss function calculates the prediction error, and this prediction error is used to update the weights of the CNN during training. Because the developed CNN is used for regression, the mean squared error (MSE) is used as a loss function. The MSE is the mean of the squared differences between the predicted and actual values, which is calculated by:

$$MSE = \frac{1}{p}\sum_{i=1}^{p}\left(\hat{y}^i - y^i\right)^2 \tag{5.12}$$

where p is the number of data samples, i is the sample's index, $\hat{y}$ is a vector with the predicted clad height and width, and y is a vector with the actual clad height and width. To evaluate the performance of the developed CNN quantitatively, the mean absolute percentage error (MAPE) is calculated. MAPE is a measure of average error between the LDED process measurements and CNN predictions. Additionally, the MAPE is easy to understand because the error is calculated in terms of percentages. The MAPE is calculated by:

$$MAPE = \frac{1}{p}\sum_{i=1}^{p}\left|\frac{\hat{y}^i - y^i}{\hat{y}^i}\right| \quad \textbf{(5.13)}$$

where again, p is the number of data samples, i is the sample's index, $\hat{y}$ is a vector with the predicted clad height and width, and y is a vector with the actual clad height and width.

5.2.2 Thin-Walled Geometry Prediction Performance

To create a CNN a dataset must be created which includes the desired inputs to the algorithm and the correct outputs. For this research, the desired inputs of the system are IR images, visible-light images, scanning speed, laser power, and layer number. Using these inputs, the CNN was trained to estimate the clad height and width. To create the dataset, 6 experiments were conducted in total, which are outlined in Table 5-3. Each experiment features 5 layers of a single 80mm track with a 0.5mm increase in the z-direction between each layer. A fixture was used to secure the substrate to ensure the tracks are aligned directly above the previous layer. Figure 5-17 shows the clad formed in experiment 1 to demonstrate the print path of the experiments.

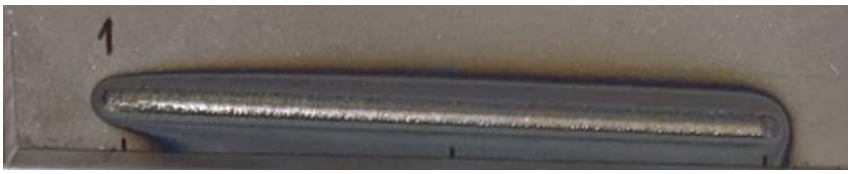

Figure 5-17: Clad created from first layer of experiment 1

During these experiments, images were captured using both camera sensors, and the process parameters, laser power, and scanning speed, were recorded by the system. This data was then used to form the dataset. Once the completed dataset was created data from experiments 2 to 6 were shuffled and split into 60% - training, 20% - validation, and 20% - testing. These subsets of the data are used to train and test the CNN.

Table 5-3: Details of experiments used to create the dataset used for training, testing, and validating the CNN

Experiment Number	Laser Power (W)	Scanning Speed (mm/s)
1	950	1.67
2	950	1.67
3	950	2.0
4	950	1.33
5	850	1.67
6	1050	1.67

Experiment 1 was used to demonstrate the performance of the CNN against a dataset that was not involved in training. Experiments 1 and 2 have the same process parameters to ensure that the data from experiment 1 was not seen by the CNN, but similar data was used in training.

To create the outputs for the dataset, the true geometry must be known, so the CNN is trained with the correct information. The height and width of the clad are measured after the process using macro-imaging, which allows a zoomed-in image of the clad to be taken. These images were then segmented to differentiate the clad from the background and knowing the scale of the image the geometry can be extracted. A visualization of the segmentation is illustrated in Figure 5-18a where the clad is highlighted in yellow. In Figure 5-18b the segmentation of the second layer is shown, where since the height of the first layer was measured, the difference was calculated to determine the height that was added during this pass.

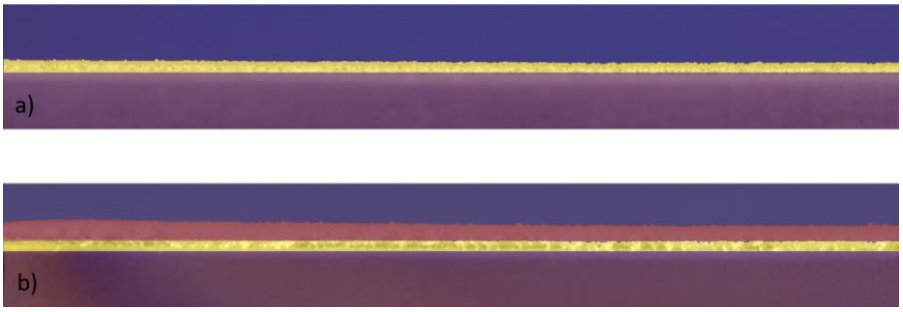

Figure 5-18 Macro imaging and segmentation used to measure the real clad geometry. a) first layer of deposition, with clad highlighted in yellow and substrate in red. b) second layer of deposition with the height of the first layer highlighted in yellow to demonstrate the difference, which is the added material.

Hence, the true geometry was measured for each layer, and a fixture on the CNC ensured that the substrate had the same starting location for all subsequent layers. With the true geometry measured, the

framerate of the images being recorded in real-time was used to align the real-time captured data to the true geometry measurements.

After training the CNN for 200 epochs, the performance of the CNN was analyzed on the original dataset. The developed CNN resulted in an MSE of less than 0.0006 and MAPE of less than 2.05%. These values show that the CNN established a highly accurate correlation between the images with process inputs and the clad dimensions. To further analyze the overall accuracy of the CNN on the original dataset, the clad geometry predictions were compared to the actual clad width and clad height values. This comparison is shown in Figure 5-19 and shows that the CNN fits to the data well. With small deviations between the actual values, during multi-track LDED, and the CNN predictions. The CNN features an average computational time of approximately 0.037 seconds per timestep, allowing for the geometry to be predicted at a frequency of 27Hz. It should be noted that the actual and predicted measurements are both present on the below chart, but since the deviation is small, the difference is difficult to see.

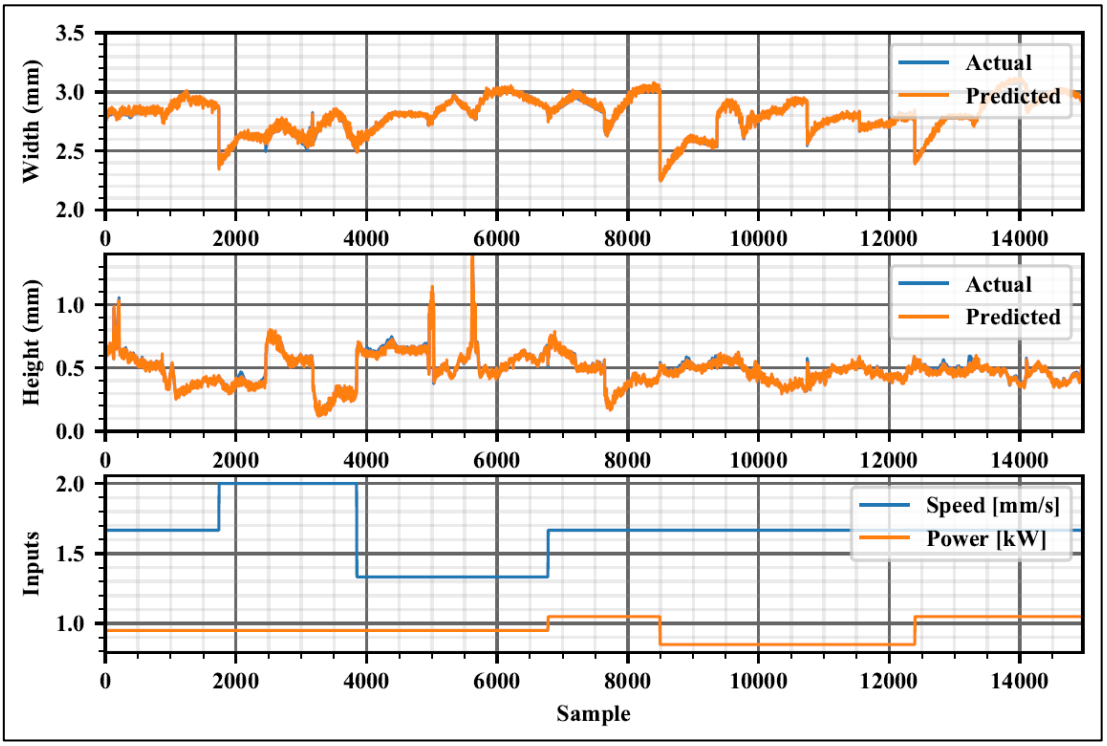

Figure 5-19: CNN predictions compared with the actual measurements when using the original dataset. Note that for the combined data set comprised of the training, validation, and test sets the predictions are sufficient such that the actual measurements are barely visible on this graph.

To further quantify the performance of the CNN on the original dataset, the coefficient of determination (R^2) between the predicted and actual clad width and clad height is calculated. The coefficient of determination is a quantitative indicator of the CNN accuracy and is computed with:

$$R^2 = 1 - \frac{\sum_{i=1}^{p}\left(y^i - \hat{y}^i\right)^2}{\sum_{i=1}^{p}(y^i - \bar{y})^2} \tag{5.14}$$

where p is the number of data samples, i is the sample's index, $\hat{y}$ is a vector with the predicted clad height and width, y is a vector with the actual clad height and width, $\bar{y}$ represents the mean measured clad height and width. The calculated clad width R^2 value is 0.981 and the calculated clad height R^2 value is 0.969, which shows there is a very good correlation between the predictions and the actual values of the clad geometry. The R^2 is visualized in Figure 5-20, which compared the data (blue dots) to the regression line (black). As shown in this figure, the CNN fits the data well. However, this figure shows that there are a few outliers, which could be caused by noise in the data or overfitting of the CNN.

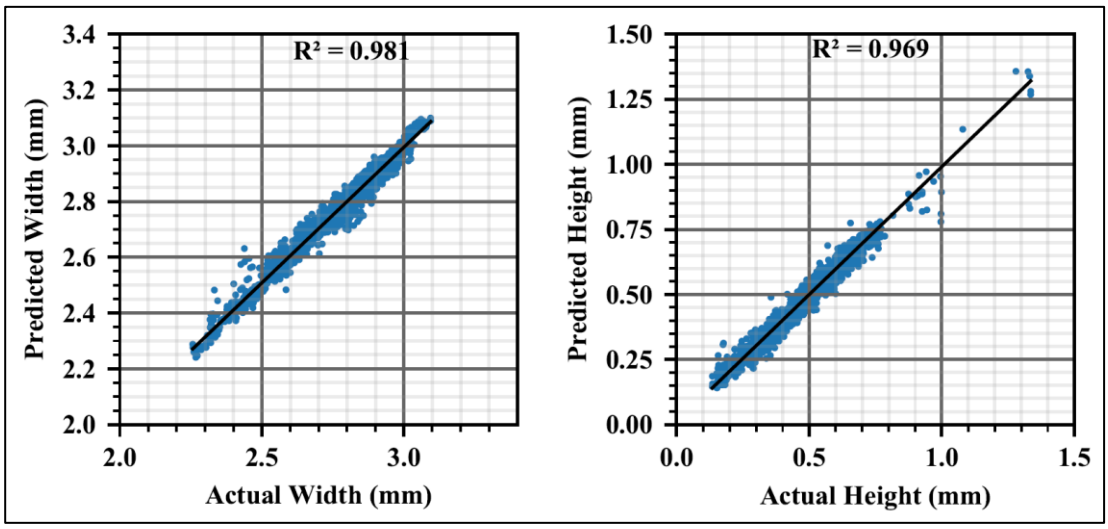

Figure 5-20: Coefficient of determination between the actual and predicted geometry, generated from the test set.

To demonstrate the approximate real-time performance, the data from experiment 1 was entered into the trained CNN to compare the actual measurements against the predictions. As mentioned previously, experiment 1 from Table 5-3 was not used in the training, validation, or test sets and therefore demonstrates the performance of the CNN against unseen data. When only considering experiment 1,

the MSE corresponded to approximately 0.016, while the MAPE was approximately 12.41%. This performance is quantified in Figure 5-21, where the calculated clad width R^2 value is 0.205 and the calculated clad height R^2 value is 0.486.

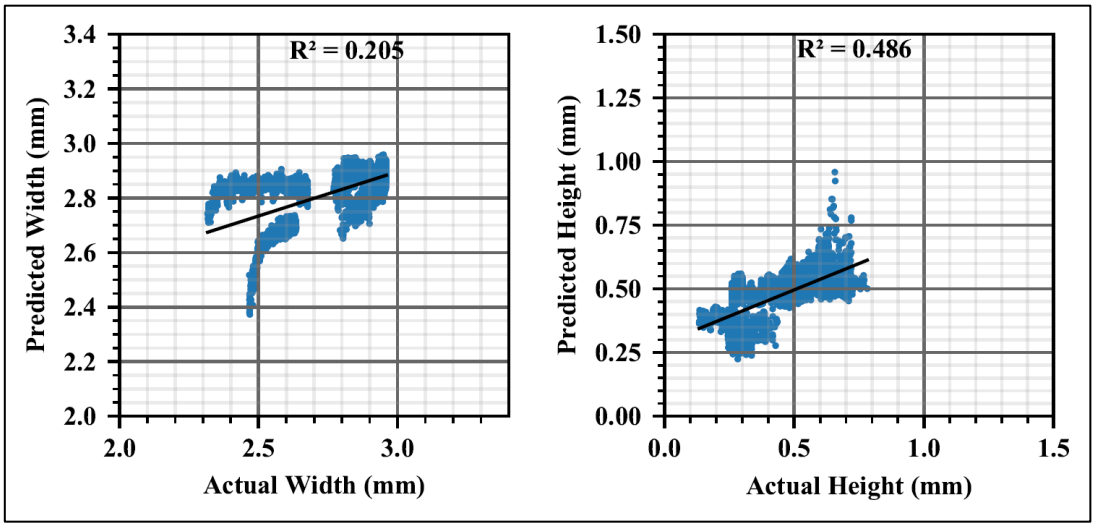

Figure 5-21: Coefficient of determination between the actual and predicted geometry, generated from the unseen set.

In Figure 5-21, the coefficient of determination is lower because the width of the clad is strongly correlated to the laser spot diameter, which was not considered in this algorithm, while the height is strongly dependant on the laser scanning speed. To better quantify the data. the graph shown in Figure 5-22 features the height predictions of all 5 layers added to show the accumulated error. This figure demonstrates that despite the relatively low coefficient of determination the CNN was able to predict the height of the clad in a dataset not included in training or validation.

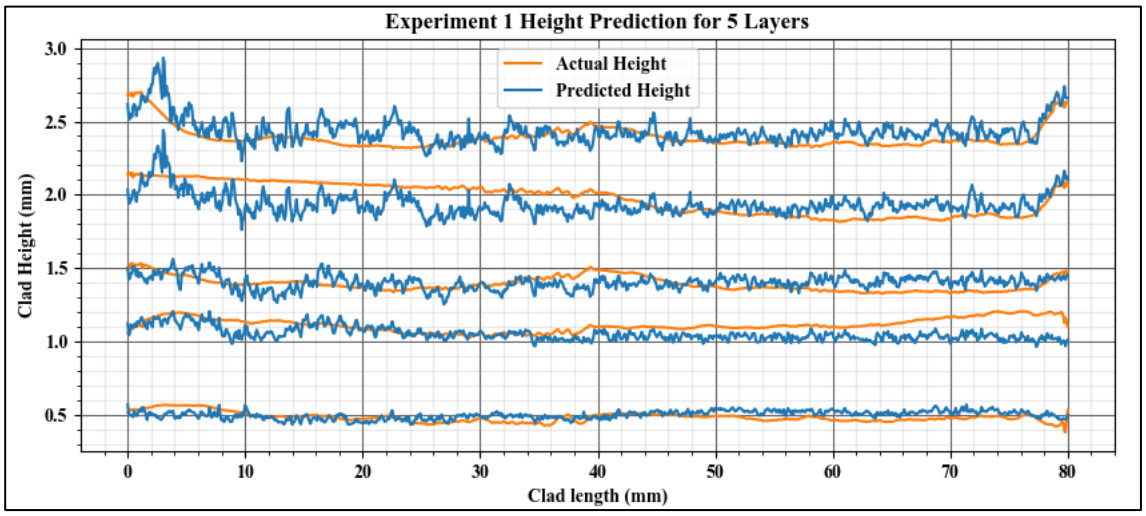

Figure 5-22: Height prediction for each layer in experiment 1 to demonstrate the accumulated error.

The data summarized in Figure 5-22 indicates that cumulative errors are not a significant concern when using this CNN. Demonstrating the cumulative height predictions of experiment 2, shows even less accumulation of error, as seen in Figure 5-23. However, it should be noted that approximately 60% of this data was included in the training set and 20% in the validation set, as mentioned previously.

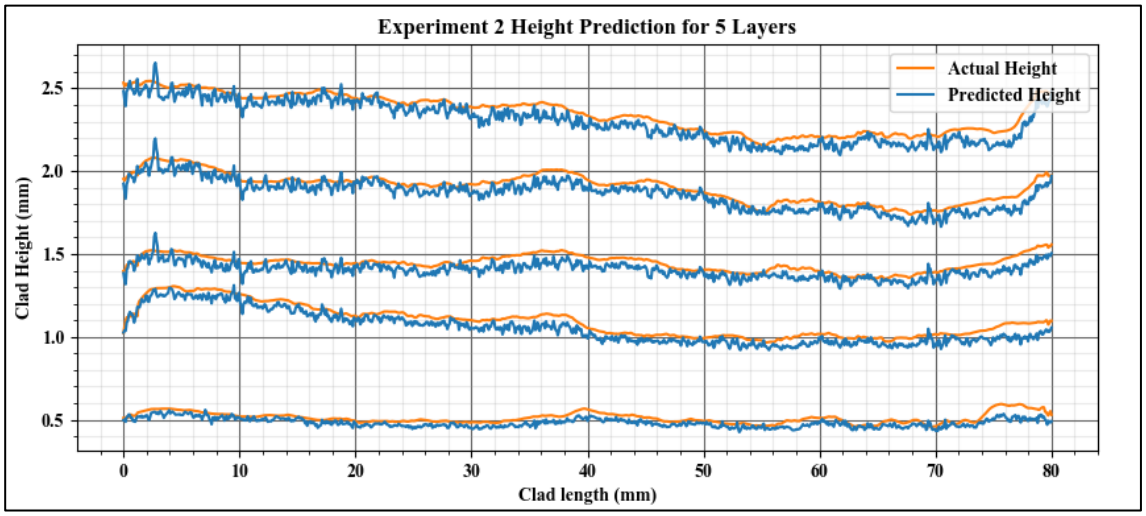

Figure 5-23: Height prediction for each layer in experiment 2 to demonstrate the accumulated error.

5.3 Multi-Track Geometry Prediction with Machine Learning

A limitation of the previous height prediction algorithm is that it neglects the scenario in which clads are deposited adjacent to one another. Moreover, it was found that the width of the clad is most significantly controlled by the laser spot diameter, while the height has more variation. Therefore, an updated ML algorithm is discussed in this section with the potential to monitor the height in multi-layer LAM. Additionally, only stainless-steel alloys were used to develop and validate the previous geometry prediction algorithms. Therefore, experiments were conducted with Inconel 625 powder as the feedstock experiment to demonstrate that this methodology is suitable for a range of materials with different properties.

5.3.1 Design of Experiments

The MOC sensor described in Chapter 3 was utilized to capture data during LAM to create the dataset used to train, validate, and test the geometry prediction. Experiments were conducted using a substrate of 9.5 mm 1018 hot-rolled steel with a laser spot diameter of 3 mm. This set of experiments used to validate the geometry predictions featured two different feedstocks, 106 µm type 431 stainless steel powder with a flow rate of 3.25 g/min or 60 µm Inconel 625 powder with a flow rate of 3.5 g/min. The experiments were further divided into two tool paths, one in which 6 layers were used to create a thin-walled component, and the other toolpath featured adjacent layers to create a cuboid (rectangular prism). Figure 5-24 shows schematically the different geometries used to create the necessary dataset for multi-track geometry measurements.

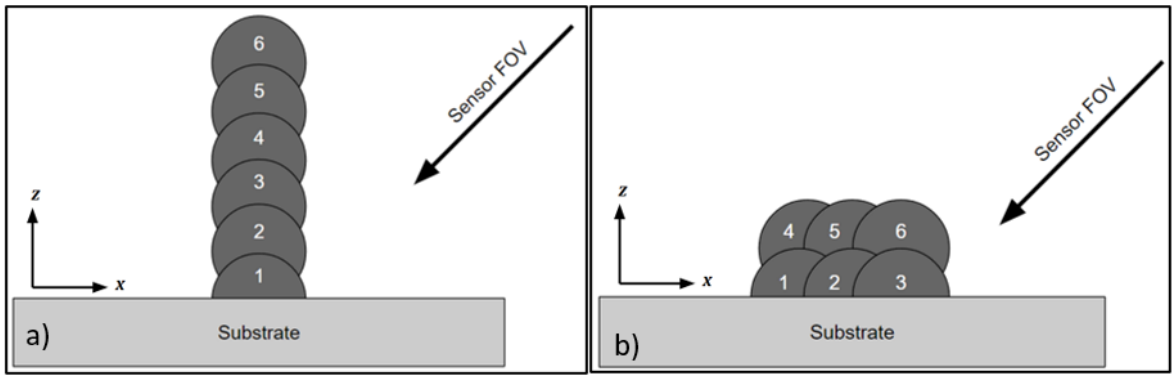

Figure 5-24 Experiments conducted for multi-track geometry measurements with the tool path a) thin wall and b) cuboid

The diagrams in Figure 5-24 show that both the thin-wall and cuboid parts featured 6 layers to ensure the dataset does not have a bias to one particular tool path. The layers are labelled in the diagrams according to their order of manufacture. Furthermore, the MOC sensor was positioned to always have the melt pool unobstructed in the FOV. Table 5-4 describes the scanning speed, feedstock material, and part geometry of all the experiments used to create this dataset.

Table 5-4 Process parameters for multi-track geometry measurement dataset

Experiment Number	Scanning Speed	Material	Part Geometry
1	1.0 mm/s	431 stainless-steel	Thin wall
2	2.0 mm/s	431 stainless-steel	Thin wall
3	3.0 mm/s	431 stainless-steel	Thin wall
4	1.0 mm/s	431 stainless-steel	Cuboid
5	2.0 mm/s	431 stainless-steel	Cuboid
6	3.0 mm/s	431 stainless-steel	Cuboid
7	1.0 mm/s	Inconel 625	Thin wall
8	2.0 mm/s	Inconel 625	Thin wall
9	3.0 mm/s	Inconel 625	Thin wall
10	1.0 mm/s	Inconel 625	Cuboid
11	2.0 mm/s	Inconel 625	Cuboid
12	3.0 mm/s	Inconel 625	Cuboid

While Table 5-4 describes the scanning speed of each experiment, the laser power was set to a constant 1 kW, since the scanning speed has a more significant influence on the height of the clad. Each experiment consisted of 6 deposition layers, as highlighted in Figure 5-24, with a length of 50 mm. The z-coordinate was adjusted between each track based on the height of the previous experiment, and the displacement in the x-coordinate for the cuboid tracks was 1.2 mm since this would correspond to 60% overlap for a 3mm laser spot, which is cited as the optimal overlap for adjacent clads in DED [122]. Therefore, images were captured over a total of 72 tracks to create this dataset. Pictures captured after the last deposition of experiments labelled 1, 4, 7, and 10 are featured in Figure 5-25.

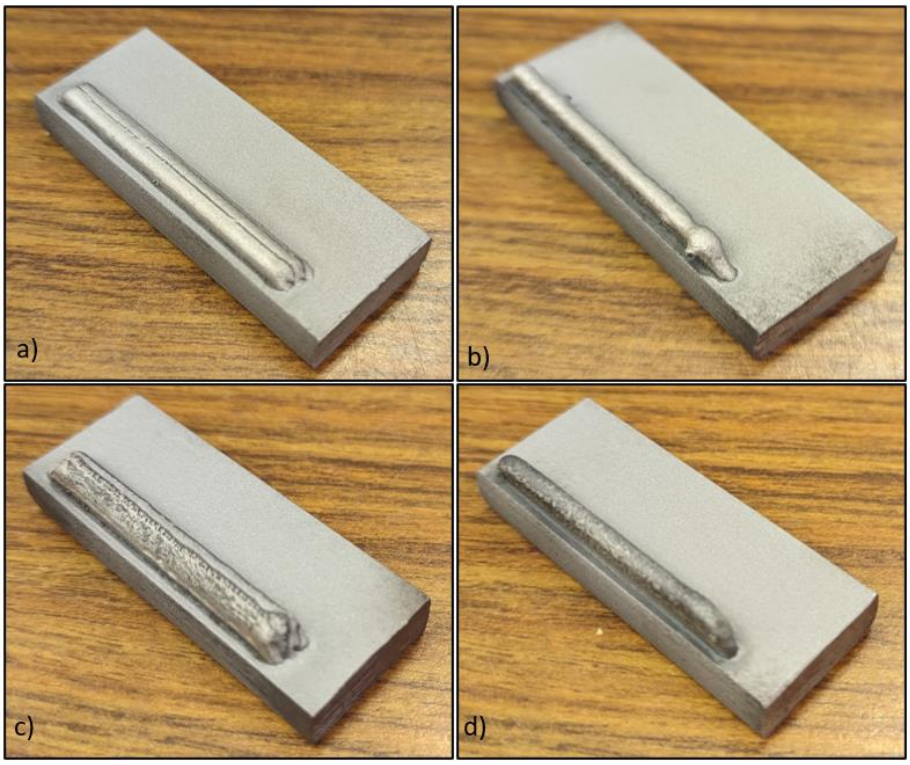

Figure 5-25 Images captured after the final deposition of a) experiment 1 b) experiment 4 c) experiment 7 and d) experiment 10

The height of each deposition was measured using macro-imaging of the clad between each track with the same method described in Section 5.2.2. Additionally, a jig was used to guarantee the substrate was placed at the same reference position after the height was measured, ensuring all tracks were deposited at the correct locations. Finally, since the experiments featured different scanning speeds, more images were captured during the experiments with slower speeds. To prevent the ML algorithm from becoming biased towards the experiments that featured more data, the dataset was limited to 500 frames of each track, therefore the total dataset featured 36000 frames, comprised of 500 frames of the 72 tracks.

5.3.2 Multi-Track Geometry Prediction Algorithm

The CNN described in Section 5.2.1 was updated to create a new algorithm capable of measuring geometry in multi-track experiments that was invariant to process parameters and materials. A CNN was still used a suitable ML algorithm for this task because CNNs are efficient at processing images and their use in thermal processing as discussed in Chapter 2. Thus, the input parameters to the CNN

were modified to only utilize features that could be extracted from images. Moreover, since methodology was discussed in Chapter 4 to predict temperature measurements with the visible light camera, IR images were excluded from this algorithm.

Before implementing the CNN, the images captured from the CMOS camera are processed to extract key features related to the height of the clad. These features are referred to as the apparent height, d, which is a distance measurable directly from the camera, and the area of the melt pool. Additionally, the image is cropped to remove the unnecessary pixels surrounding the melt pool that are too dark to convey any useful information. The images are then scaled to a size of 64 × 64 pixels, having a constant size allows the CNN to process the images more efficiently since each iteration has the same sized image. The first step in image processing is to threshold the image, this allows for the area of the melt pool to be measured as shown in Figure 5-26. The distance of the MOC sensor from the melt pool and the focal point of its lens allows the area to be converted from squared pixels to squared millimeters.

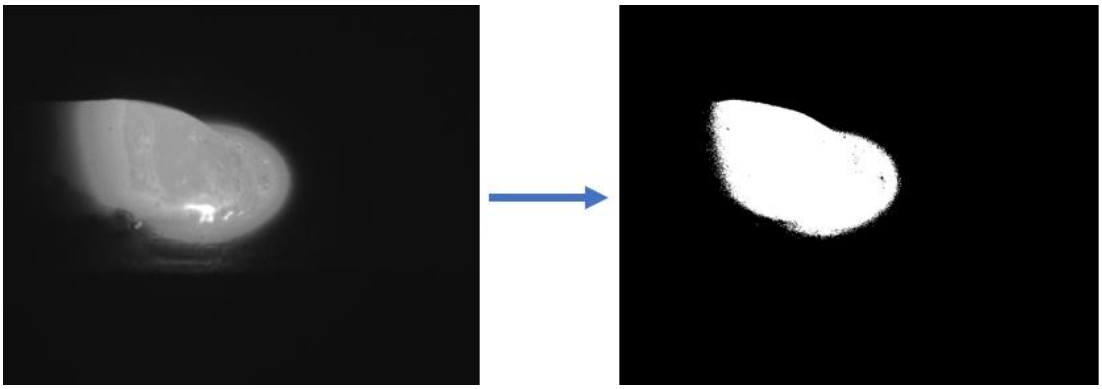

Figure 5-26 Thresholding the image to determine the melt pool area

Once the image was thresholded, the apparent height, d, can be measured in the same methodology described in Section 5.1.1. Figure 5-27 summarizes how this distance is measured from the thresholded image as well. Since the location of the laser spot is known, the apparent height is calculated based on the solidified region of the clad; which excludes some of the light at the center of the laser spot, as shown in Figure 5-27b.

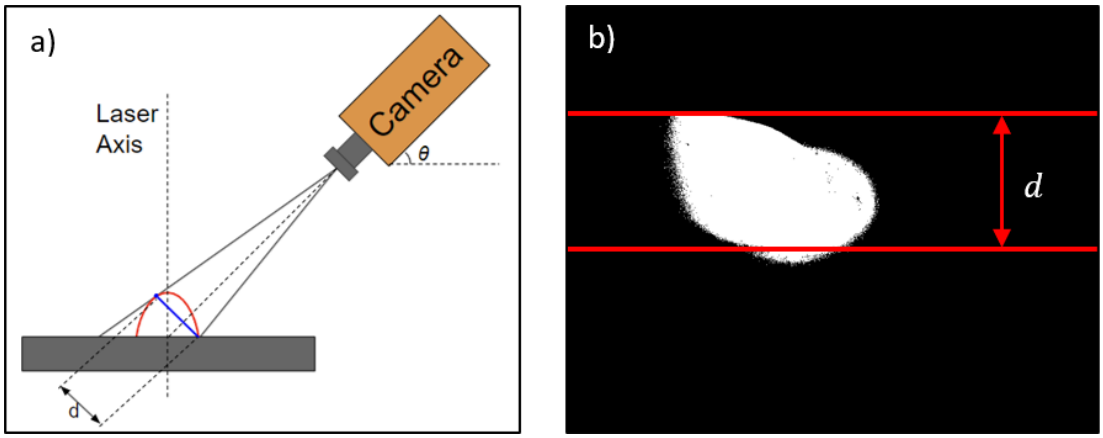

Figure 5-27 a) Diagram illustrating the distance, *d*, also referred to as the apparent height. b) The apparent height, *d*, as extracted from the thresholded image.

The area of the melt pool was used to crop and scale the originally captured image, which was reduced to 64 × 64 pixels, as shown below in Figure 5-28. Once the size of the image was reduced, the image was normalized so every pixel had an intensity from 0 – 1, this ensures that the intensity values are in the same scale as the other features, which prevents the CNN from being disproportionately weighing these features. Therefore, the features used to predict the height were the melt pool area, the apparent height, *d*, and the normalized image. Using these features, a CNN was created with the architecture shown in Figure 5-29. It is shown that the CNN predicted height measurements from the captured image and features extracted from the image as well, so predictions are not biased by process parameters.

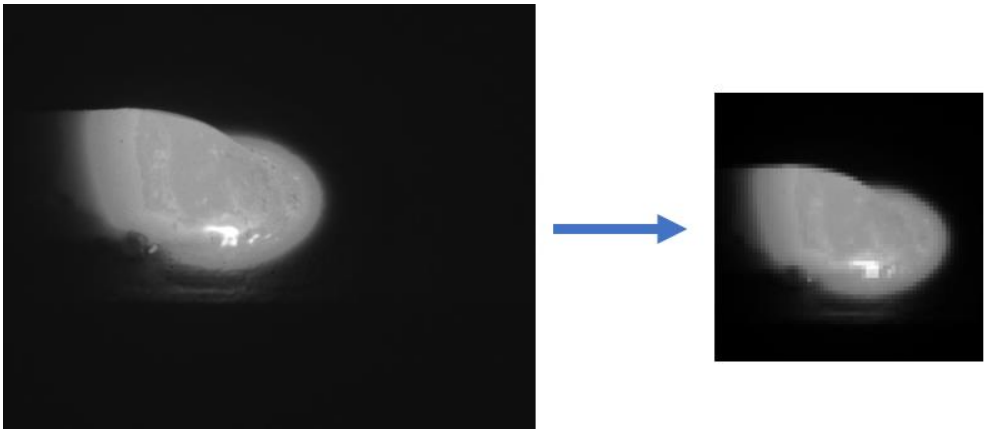

Figure 5-28 Image processing from the original image to a 64 × 64 pixel image of only the melt pool

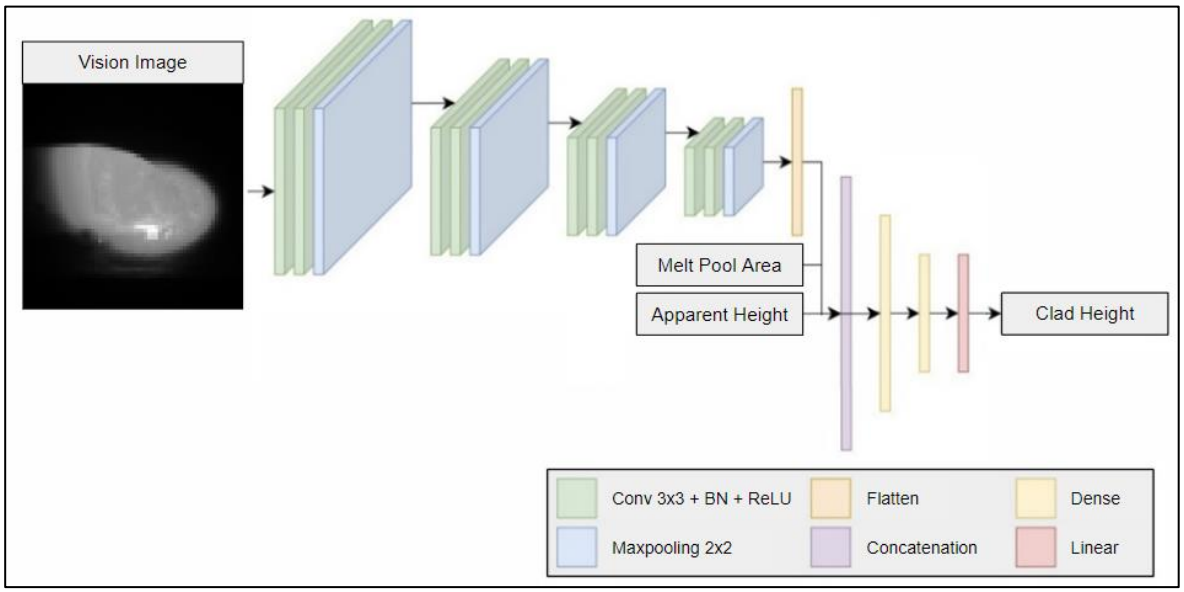

Figure 5-29 CNN architecture used for real-time height prediction of multi-track thermal processes

The CNN for multi-track height prediction was trained using MSE, Eq. (5.12), as its loss function with the dataset described in Section 5.3.1 divided such that 50% of the data was used as the training set, 30% as the validation set, and the remaining 20% as the test set. A validation set is used to reduce the impact of overfitting the data to the training set. The CNN is trained with the training set, but the accuracy is measured against the validation set, which is data the model has not seen before. Therefore, the model's accuracy as measured against the validation set is more similar to the expected performance of the model. The model was trained with a batch size of 256 for 100 epochs, where the MSE and mean absolute error (MAE) were calculated after each epoch. The MAE is calculated by:

$$MAE = \frac{1}{p}\sum_{i=1}^{p}\left|\hat{y}^i - y^i\right| \tag{5.15}$$

where p is the number of data samples, i is the sample's index, $\hat{y}$ is a vector with the predicted clad height and width, and y is a vector with the actual clad height and width. Once training was completed, the coefficient of determination was calculated with Eq. (5.14) to determine the performance of the CNN against the test set. Against the test set, the coefficient of determination was found to be 0.983 as shown in Figure 5-30.

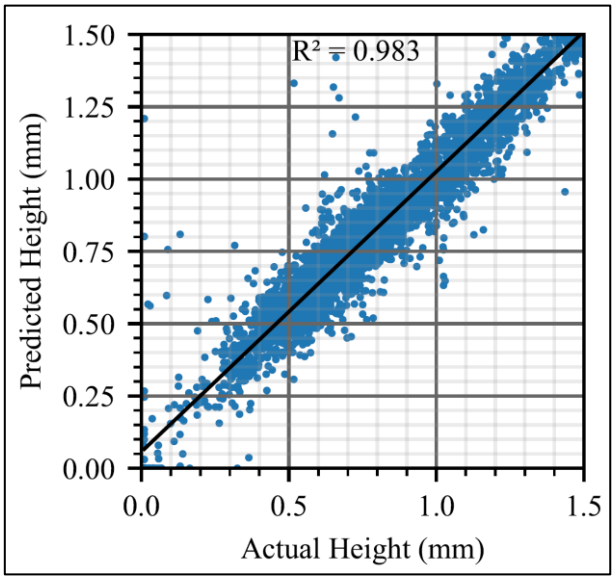

Figure 5-30 Coefficient of determination between the actual and predicted height of the test set

5.4 Summary

Initially, the geometry (height and width) of the clad was monitored during LAM in real-time using a model-based approach. In this approach the cross-section of the clad was assumed to be a circular arc, which is formed from the surface tension of the melt pool. This approximation, and observable features captured with real-time imaging allowed for the height and width of the clad to be calculated at every time step. Furthermore, this algorithm was found to be sufficient in measuring the height and width in real-time with a MAPE of 6.58% and 3.48%. However, the approximate shape of the clad assumes a flat substrate; therefore, this algorithm is limited to single-track depositions.

The single-track limitation motivated the shift towards using ML to estimate the geometry of the clad in real-time. Utilizing ML allows for the geometry of the clad to be predicted without any assumptions of the shape of the cross-section of the clad. Therefore, using a training dataset that featured a sufficient amount of data with various combinations of process parameters a CNN was created to estimate the height and width of the clad in real time. The CNN used both visible-light and IR images captured during the process, as well as process parameters such as laser power, scanning speed, and layer number to determine the height and width of the clad in real-time. After training, the CNN was able to predict the geometry of the clad with a MAPE of 12.4%.

To utilize ML more effectively, another CNN was developed to predict the height of the clad in real time using only features from the visible-light camera sensor. While the width was not directly

measured with this algorithm, the width is strongly correlated to the laser spot size, and therefore, monitoring height was deemed more critical. The motivation behind implementing this change was to monitor the height in scenarios where process parameters may not be within the scope of the training set. Moreover, this dataset featured both thin-walled and overlapping adjacent tracks with 431 stainless steel and Inconel 625 to ensure the CNN was trained with multiple different cases.

Chapter 6
Results and Discussion

This chapter discusses the performance of the developed monitoring system in measuring geometry and material properties of thermal processes in real-time. The framework for monitoring material properties with thermal dynamics is outlined, with a detailed description of how the thermal dynamics are extracted from captured image. How thermal dynamics impact the final material properties is explored for multiple materials to demonstrate the flexibility of this approach. Different processes are explored as well with LHT experiments conducted in open-loop and with closed-loop control utilizing thermal dynamics measurements. The effectiveness of geometry monitoring and control during LDED is explored based on the techniques described in Chapter 5. Finally, the effectiveness of monitoring geometry and thermal dynamics in GMAW is explored to exhibit monitoring of thermal processes with a different heat source.

6.1 Prediction of Material Properties Using Thermal Dynamics

Thermal dynamics have a significant influence on the microstructure and material properties of metals. In thermal processes, the concentrated heat source rapidly heats and cools the metal, with some processes creating a melt pool, all these effects influence material properties. When the melt pool cools and solidifies, its microstructure is formed. The cooling rate and thermal gradients during solidification impact the nucleation and growth of crystals, which determine the grain structure of the metal. Slower cooling rates generally promote the formation of larger grains, while faster cooling rates result in finer grain structures. Heating and cooling processes can also induce phase transformations in metals, such as the transition from austenite to ferrite or martensite. These phase transformations affect the microstructure, resulting in changes in grain size, crystallographic structure, and the presence of different phases within the metal. Thermal processes can also trigger recrystallization and grain growth in metals. Recrystallization replaces the deformed grains with new strain-free grains, while grain growth leads to an increase in grain size. Therefore, understanding the thermal dynamics and their influence on microstructure is crucial for controlling and optimizing thermal processes.

6.1.1 Thermal Dynamics Measurements

The temperature distribution is used to measure the thermal dynamics of the HAZ in real-time. Figure 6-1 shows typical temperature distributions captured during LHT and LDED.

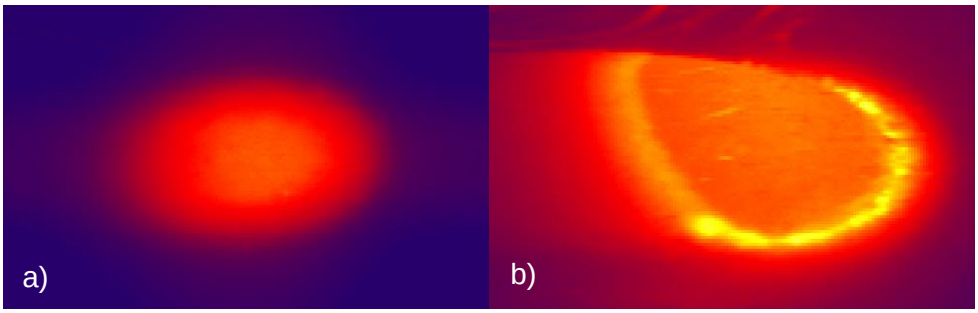

Figure 6-1 Typical temperature distribution for a) LHT and b) LDED

Note that the temperature distributions in Figure 6-1 are shown with the images cropped to remove excess data and a box filter applied to reduce noise. LHT experiments were used to derive and validate thermal dynamics measurements to remove the effect of powder flow from the experiments and since the temperature distribution is simpler; though these properties are present in other thermal processes and are calculated in the same way.

It has been shown in [43] - [51] that cooling rate or solidification time can be measured to predict the microstructure of an LMP part. Cooling rate is defined as the rate for the temperature of the HAZ to reduce from the peak temperature to a critical, lower temperature where a phase change occurs. The phase change temperature is selected to be within a measurable range and corresponds to a phase change in the working material. As an example, for 1018 cold rolled steel that temperature can be set to 727°C since that corresponds to a phase change [105]. Therefore, the cooling rate can be defined as:

$$\Delta\dot{T} = \frac{T_{Peak} - T_{Phase}}{t_{solidification}} \tag{6.1}$$

where the cooling rate, $\Delta\dot{T}$ is calculated by the difference between the peak temperature T_{Peak} and the temperature in which a phase change occurs T_{Phase}, divided by the time taken to cool from the peak temperature to the phase change temperature, $t_{solidification}$. Furthermore, solidification time can be defined generally using the formula:

$$t_{solidification} = t_{Phase} - t_{Peak} \tag{6.2}$$

where t_{Phase} refers to the time that the HAZ reaches T_{Phase} and t_{Peak} is the time at which the HAZ has a temperature of T_{Peak}.

Since the thermal distribution is dependent on the framerate of the camera sensor, the continuous formulae, Eq. (6.1) and (6.2), must be modified to accommodate the discrete measurements of the

equipment. To calculate the cooling rate, the value and location of the peak temperature for each frame are saved; then, based on the framerate of the camera sensor and the scanning speed of the CNC, that pixel is tracked in all future frames until its temperature is less than or equal to T_{Phase}. In Figure 6-2 a set of frames from the IR camera are shown which demonstrate pixel tracking, with the tracked pixel highlighted in green. Since the framerate of the camera and scanning speed of the laser are known, the pixels are tracked by calculating its displacement between captured frames. In this example, images were captured with the MOC sensor mounted with a lateral FOV and the scanning direction is to the right.

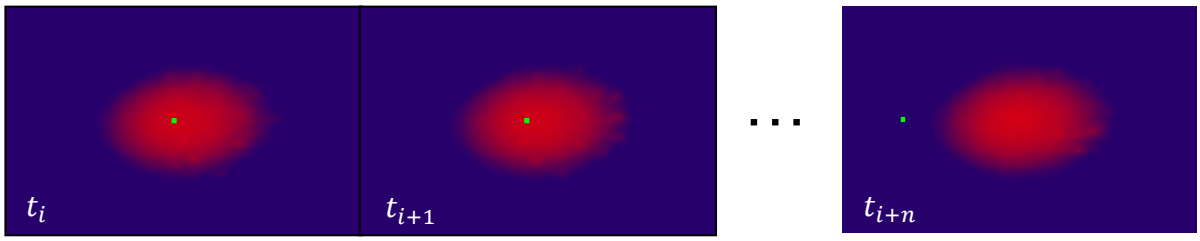

Figure 6-2 Visualization of pixel tracking, where the tracked pixel is highlighted in green

Figure 6-2 visualizes the tracked pixel, which is highlighted in green, the subscript refers to the frame of the camera. Here the cooling rate calculation starts at some frame *i* and is tracked for *n* frames, until the pixel reaches the desired temperature. Using this discretization, the thermal dynamics can be approximated with the following formulae,

$$t_{solidification} = nf \tag{6.3}$$

$$\Delta\dot{T} = \frac{T_{Peak} - T_{Phase}}{nf} \tag{6.4}$$

where n is the number of frames taken for the center pixel to cool from T_{Peak} to T_{Phase} and f refers to the framerate of the temperature distribution measurements. Alternatively, if we assume the process is at steady state, we can calculate the solidification time using only the temperature distribution of the current timestep, which is computationally faster and removes the delay of waiting multiple frames for the pixel to cool. This assumption is based on the quasi-stationary condition, which states that if the substrate is sufficiently large compared to the heat transfer field, then the distribution of the heat source becomes independent of time [123]. Assuming that the quasi-stationary condition is valid, the new solidification time and cooling rate formulae are:

$$t_{sol.,ss} = \frac{\Delta x}{v} \tag{6.5}$$

$$\Delta \dot{T}_{SS} = \frac{(T_{Peak} - T_{Phase})v}{\Delta x} \tag{6.6}$$

where Δx is the distance between the peak temperature location and the location of the HAZ with a temperature equal to the set point as seen in Figure 6-3 and v is the laser scanning speed.

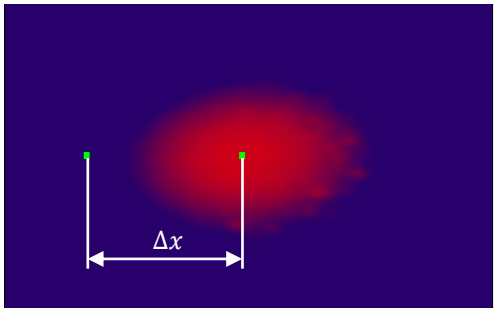

Figure 6-3 Visual representation of Δx, used to calculate the cooling rate

Literature has shown that cooling rate is closely tied to material properties of parts produced in thermal processes. However, a similar calculation can be performed to compute the heating rate in real time as well, which offers more insight into the thermal dynamics of the process. Therefore, the heating rate can be calculated with

$$\Delta \dot{T}_{heat} = \frac{(T_{Peak} - T_{Phase})v}{\Delta x_2} \tag{6.7}$$

where the distance Δx_2 is the distance between the peak temperature and the first pixel to reach the phase transformation temperature in front of the laser's path. Figure 6-4 shows Δx_2 when the scanning direction is to the right; hence, the heating rate is using the distance in front of the laser's path.

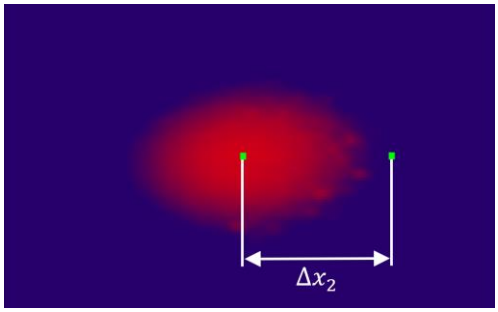

Figure 6-4 Visual representation of Δx_2, used to calculate the heating rate

Though the thermal dynamics measurements were described with LHT experiments with images captured from a lateral FOV. The same calculation can be conducted with a coaxial field of view assuming the center location of the laser spot and direction of travel are still known. Similarly, this methodology can also be expanded to LAM, GMAW, and other thermal processes assuming the location of the melt pool's center is known, and within the FOV of the MOC sensor, and scanning speed and direction are known.

6.1.2 Correlation of Thermal Dynamics to 431 Stainless Steel Material Properties

A series of experiments were conducted to validate the cooling rate calculations described in the previous section as an effective metric for microstructure monitoring. Eight experiments were conducted, which are depicted in Figure 6-5. This set of experiments were performed on substrates of 6.3 mm thick 1018 cold-rolled steel with a laser spot diameter of 3mm using 150 µm 431 stainless steel powder at a feed rate of 3g/min. All eight, 75 mm long tracks feature a constant laser power of 1kW, while a constant scanning speed between 1.0 – 4.5 mm/s as highlighted in Table 6-1. Between each track the specimen was allowed to cool to room temperature to eliminate the effect of heat accumulation on the final microstructure.

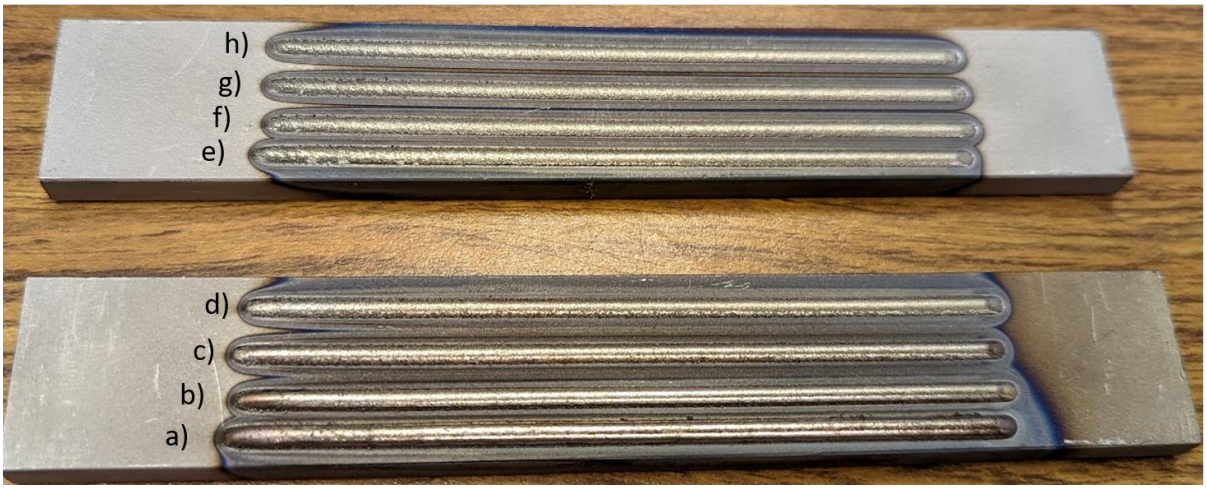

Figure 6-5 Single track LDED experiments to correlate cooling rate to microstructure of 431 stainless steel

The scanning speeds of this set of experiments and the corresponding average cooling rate and hardness measurements are reported in Table 6-1. Where the hardness was measured by averaging at least 5 indentations at the center of the deposition with a Clemex microhardness tester using a load of

1 kg. The cooling rate was measured for each track using data collected in real-time with the MOC sensor module. The cooling rate calculation was described in Section 6.1.1 with temperatures predicted as described in Section 4.2. In this experiment, the cooling rate was measured from the temperature at the center of the melt pool to 900 °C.

Table 6-1 Correlation of cooling rate and material properties of LDED 431 stainless steel

Track Label	Scanning Speed	Average Cooling Rate	Average Hardness (HV)	Hardness (HV) Standard Deviation
a	1.0 mm/s	93.6 °C/s	504	20.7
b	1.5 mm/s	179.3 °C/s	513	11.3
c	2.0 mm/s	265.2 °C/s	525	13.1
d	2.5 mm/s	327.8 °C/s	576	14.5
e	3.0 mm/s	390.6 °C/s	547	18.5
f	3.5 mm/s	477.1 °C/s	567	9.6
g	4.0 mm/s	559.7 °C/s	571	20.5
h	4.5 mm/s	598.5 °C/s	605	30.6

The average cooling rate for each experiment was noted in Table 6-1, while the real-time cooling rate throughout the track is reported in Figure 6-6. At the beginning of the deposition, the cooling rate spikes because the substrate is at ambient temperature, but quickly the process reaches steady-state due to the accumulated heat. Additionally, a Butterworth filter was used to reduce the high frequency noise while having as flat of a response as possible in the passband.

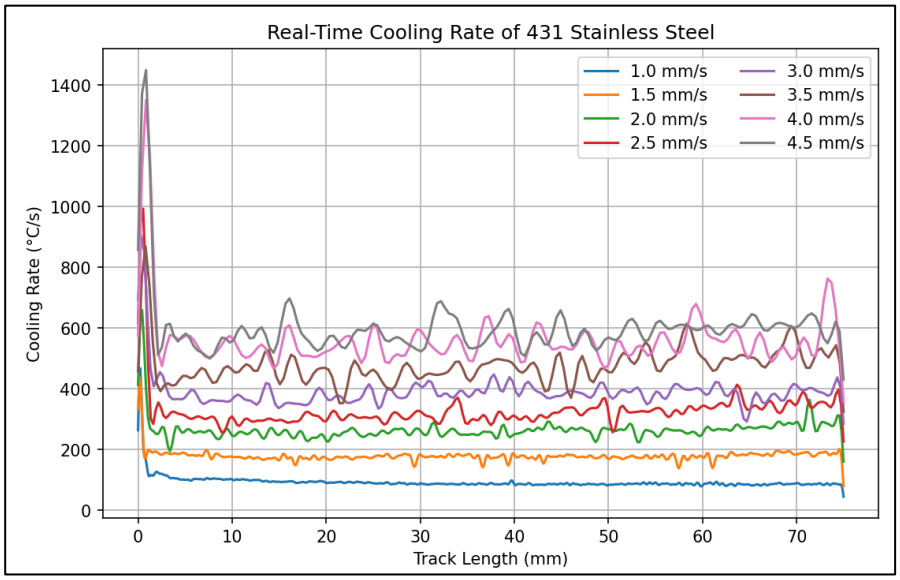

Figure 6-6 Cooling rate of 431 stainless steel at various scanning speeds

The material properties of the clads were determined after manufacturing. The center of the specimen was cut to analyze the microstructure and material properties and polished with 0.05 µm Alumina powder to allow for the microhardness to be measured and for microscopy to capture the microstructure of each track. The cut specimens are visible in Figure 6-7 with images of the corresponding microscopy images are shown in Figure 6-8. Etching was performed with Kalling's reagent number 2 to make the microstructure more visible, where the reagent was added to the surface of the polished specimen for 5 seconds. The composition of Kalling's reagent number 2 is shown in Table 6-2.

Figure 6-7 Cut and polished specimens with 431 stainless steel depositions

Table 6-2 Chemical composition of Kalling's Reagent No. 2

Chemical	Ethyl Alcohol	Copper (II) Chloride	Hydrogen Chloride	Methyl Alcohol	Isopropyl Alcohol
% Present	85 – 95	0.5 - 5	2 - 7	1 - 5	1 - 5

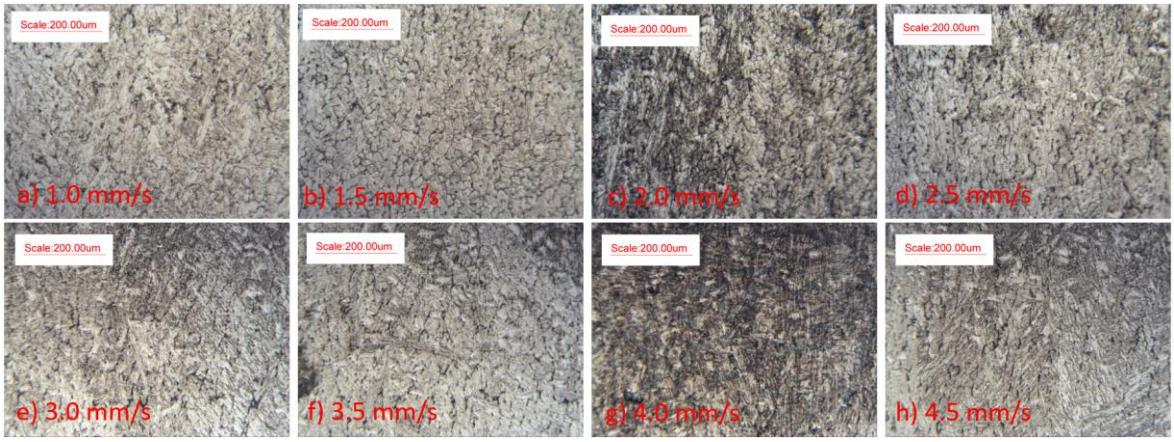

Figure 6-8 Microstructure of 431 stainless steel created with various cooling rates with 20x magnification

Figure 6-8 shows the microstructure of the 431 stainless steel depositions captured with 20x magnification. However, since the martensite packets were small 100x magnification images are shown below in Figure 6-10. The microstructures shown in Figure 6-10 feature a mostly martensitic

appearance with very little austenite between the laths, which is to be expected with a 400 series stainless steel. Another observation of the microstructure is the direction of cell growth between the top and center of the deposition, which is exaggerated in the 4.5 mm/s depositions, since the higher speed corresponds to the lowest height and fastest cooling rate. The difference in microstructure throughout the clad is visible in Figure 6-9 where the top of the clad features cell growth that is parallel to the direction of travel (which was perpendicular to the page). Meanwhile, the martensite packets are perpendicular to travel in the middle of the clad, this is because the cell growth follows the direction of heat flow. Where cells at the top of the clad are influenced by the laser and accumulation of heat, while cells at the bottom of the clad are influenced by heat conducting into the substrate.

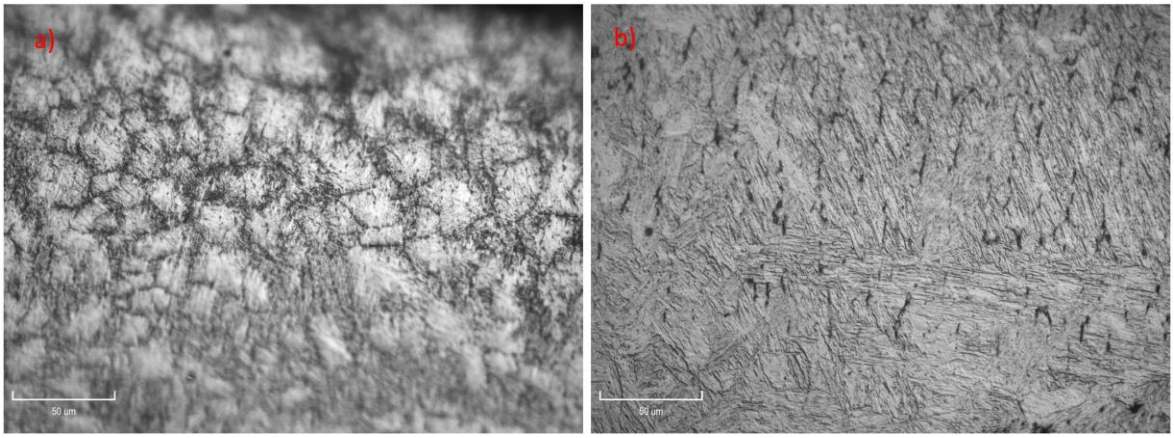

Figure 6-9 Microstructure of 431 stainless steel deposition with scanning speed of 4.5 mm/s a) top of the clad b) bottom of the clad

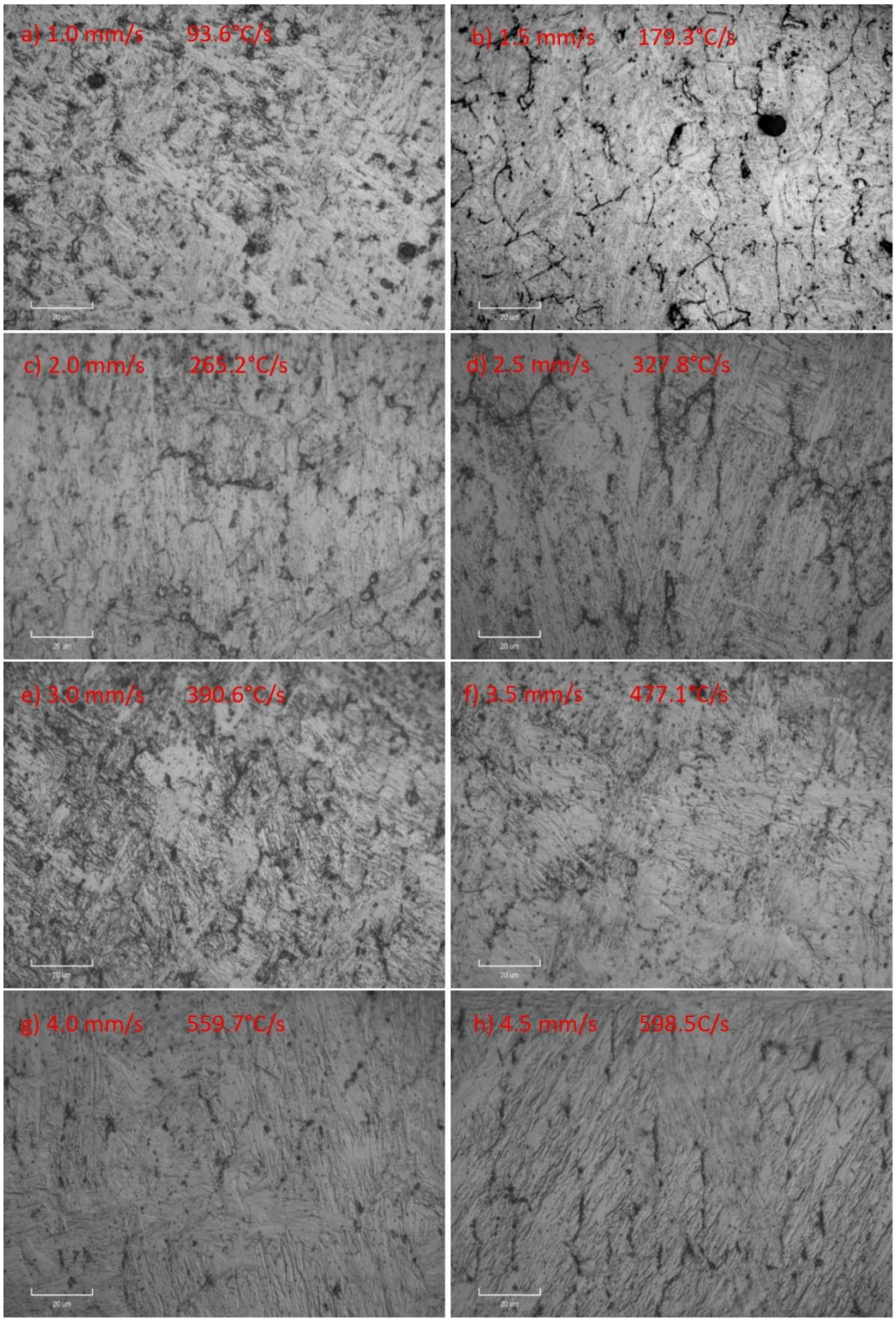

Figure 6-10 Microstructure of 431 stainless steel created with corresponding cooling rates 100x magnification

The relationship between scanning speed and calculated cooling rate of Inconel 625 is summarized in Figure 6-11. The cooling rate calculation Eq. (6.6) shows that scanning speed and cooling rate are proportional, which is confirmed in the below graph.

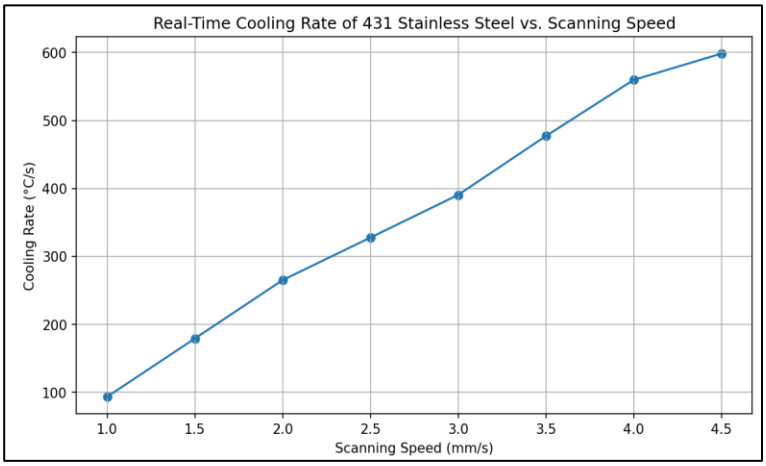

Figure 6-11 Relationship between scanning speed and cooling rate in 431 stainless steel

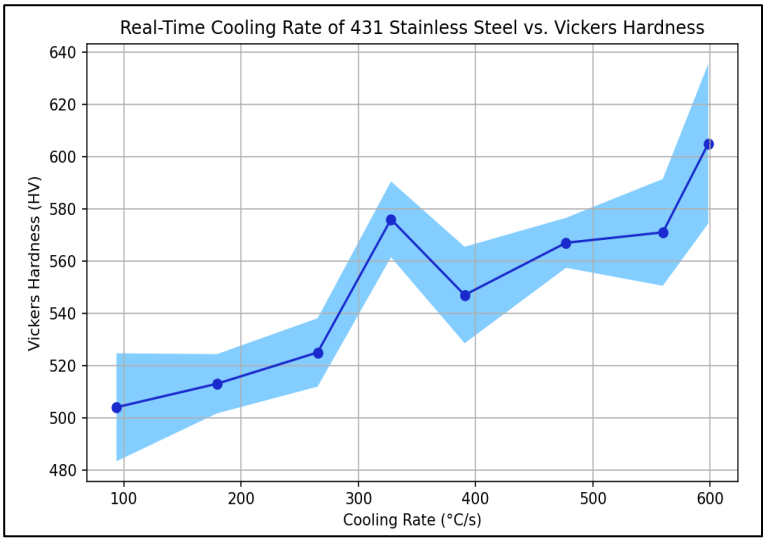

Figure 6-12 Relationship between cooling rate and Vickers hardness in 431 stainless steel

Figure 6-12 shows the relationship between the measured Vickers hardness and calculated cooling rate for the stainless steel clads. Where the solid line refers to the mean hardness values and the highlighted region is the standard deviation of hardness measurements. It is also evident that there is a proportional relationship between the calculated cooling rate and Vickers hardness of the deposition. This is due to the spacing of the martensite laths, at higher cooling rates the martensite forms tighter

packets, which results in higher hardness. However, there is an outlier at approximately 300 °C/s, the unexpected hardness may be caused by the cooling material passing through a specific location of the phase diagram, resulting in a higher density of second-phase particles than in the other cooling paths. Examining the Schaeffler diagram in Figure 6-13 shows that the stable phase for 431 stainless steel is a mixture of martensite, austenite and ferrite, the specific proportion of these phases would influence the final microstructure and hardness of the depositions highlighted in Table 6-1.

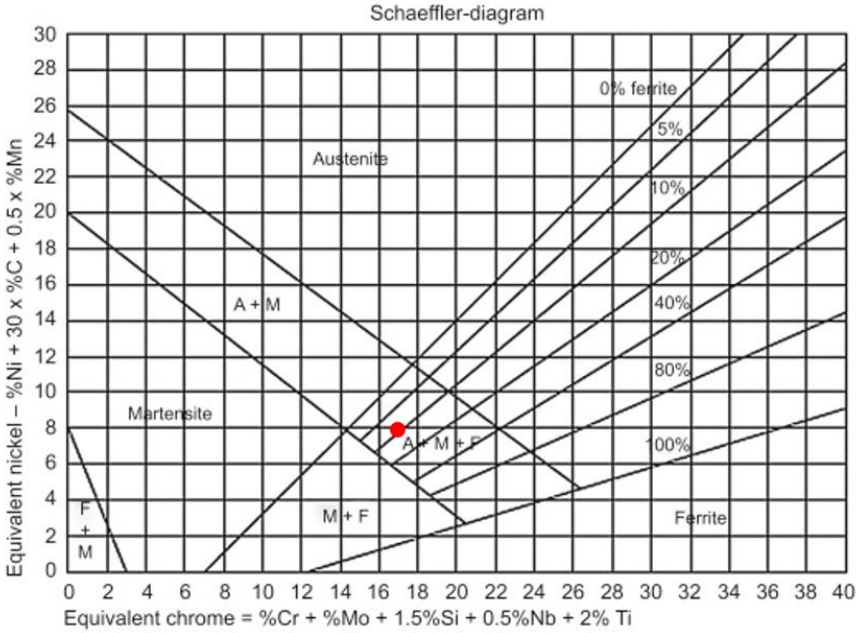

Figure 6-13 Schaeffler diagram for weld metal, where 431 stainless steel is highlighted in red [124]

To better understand the proportions of these phases, the phase diagram in Figure 6-14 demonstrates the evolutions of phases as the melt pool solidifies. Initially austenite forms in the solidifying metal, followed by δ-ferrite in a small region when the liquid phase is still present, which is circled in the diagram below. Once the liquid is entirely solidified, the composition becomes a combination of austinite and α-ferrite, where martensite forms as the metal continues to cool. During the experiment with a scanning speed of 2.5mm/s the cooling rate of approximately 300 °C/s may result in the metal spending more time in the circled region compared to the other cooling rates. Therefore, resulting in a higher concentration of ferrite, which led to a higher hardness compared to the rest of the trend.

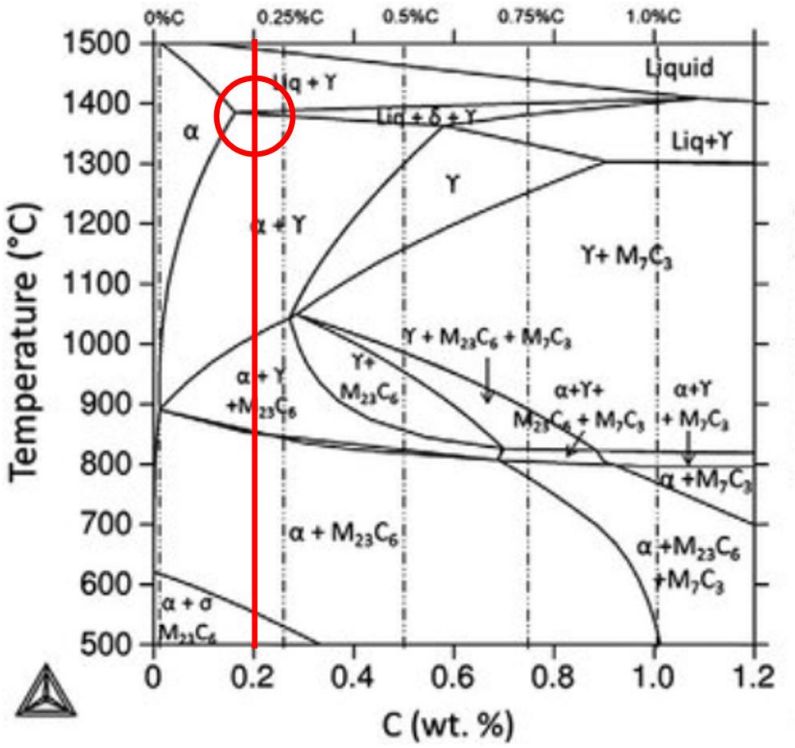

Figure 6-14 Equilibrium phase diagram for stainless steel, where 431 stainless steel is highlighted in red [125]

6.1.3 Correlation of Thermal Dynamics to Inconel 625 Material Properties

To demonstrate the effectiveness of using cooling rate as a metric for microstructure monitoring of other materials, eight experiments were conducted with Inconel 625 powder. This set of experiments were performed on substrates of 6.3 mm thick 1018 cold-rolled steel with a laser spot diameter of 3mm using 60 µm Inconel 625 powder at a feed rate of 3.5 g/min. All eight tracks feature a constant laser power of 1kW, while the scanning speed varied as highlighted in Table 6-3. Just as with the 431 stainless steel, the specimen was allowed to cool to room temperature between each track to eliminate the effect of heat accumulation on the final microstructure.

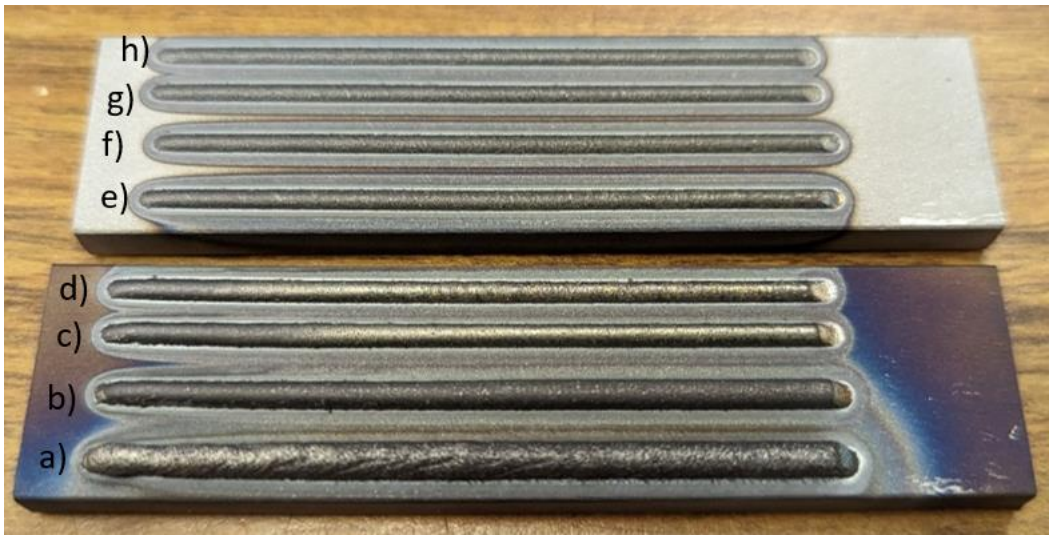

Figure 6-15 Single track LDED experiments to correlate cooling rate to microstructure of Inconel 625

A similar analysis was performed as the 431 stainless steel alloy described previously. The cooling rate was measured for each track using data collected in real-time with the MOC sensor module, with a Butterworth filter to reduce noise. Again, the cooling rate calculation was described in Section 6.1.1 with temperatures predicted as described in Section 4.2. In this experiment, the cooling rate was measured from the temperature at the center of the melt pool to 900 °C. For Inconel 625, the hardness was measured by averaging at least 5 indentations at the center of the deposition with a Clemex microhardness tester using a load of 500 g.

Table 6-3 Correlation of cooling rate and material properties of LDED Inconel 625

Track Label	Scanning Speed	Average Cooling Rate	Average Hardness (HV)	Hardness (HV) Standard Deviation
a	1.0 mm/s	64.4 °C/s	227	8.3
b	1.5 mm/s	140.2 °C/s	233	7.1
c	2.0 mm/s	246.3 °C/s	245	8.5
d	2.5 mm/s	290.9 °C/s	247	7.7
e	3.0 mm/s	333.3 °C/s	252	4.7
f	3.5 mm/s	395.2 °C/s	251	3.8
g	4.0 mm/s	438.6 °C/s	252	6.8
h	4.5 mm/s	489.1 °C/s	249	5.9

The average cooling rate for each experiment was noted in Table 6-3, while the real-time cooling rate throughout the track is shown in Figure 6-16. The cooling rate spikes at the beginning of the

deposition because the substrate is at ambient temperature, but quickly the process reaches steady-state due to the accumulated heat.

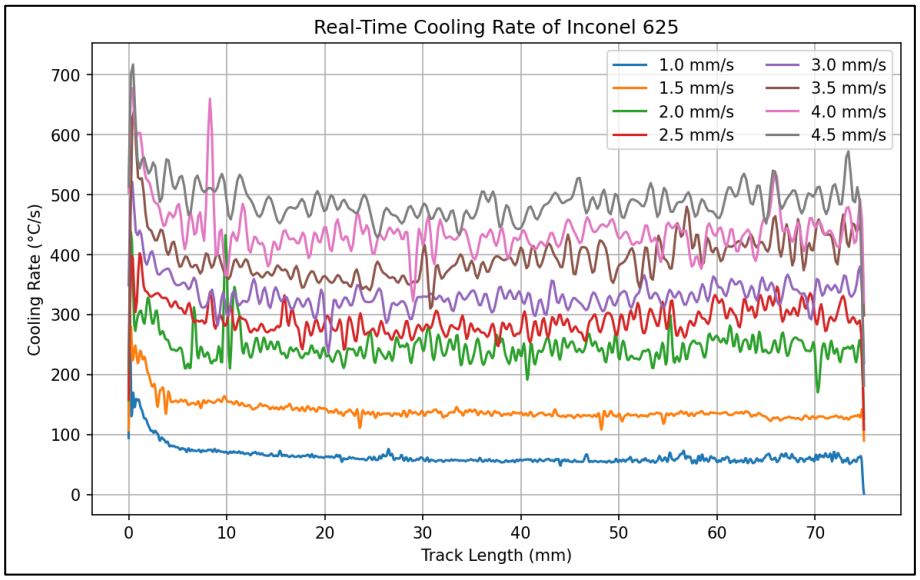

Figure 6-16 Cooling rate of Inconel 625 at various scanning speeds

The specimen was cut at approximately the center of the track to analyze the microstructure and material properties and polished with 0.05 µm Alumina powder to allow for the microhardness to be measured and for microscopy to capture the microstructure of each track. The cut specimens are visible in Figure 6-17 with images of the corresponding microscopy are shown in Figure 6-18. Etching was performed with Glyceregia to make the microstructure more visible, where the reagent was added to the surface of the polished specimen for 10 minutes. The composition of Glyceregia is shown below in Table 6-4. Since Figure 6-17 shows a small dilution zone, it was assumed that the substrate had a minimal impact on the microstructure of the deposition, though they are dissimilar metals.

Figure 6-17 Cut and polished specimens with Inconel 625 depositions

Table 6-4 Composition of Glyceregia

Chemical	Glycerol	HCl	HNO_3
Volumetric Amount	15 ml	10 ml	5 ml

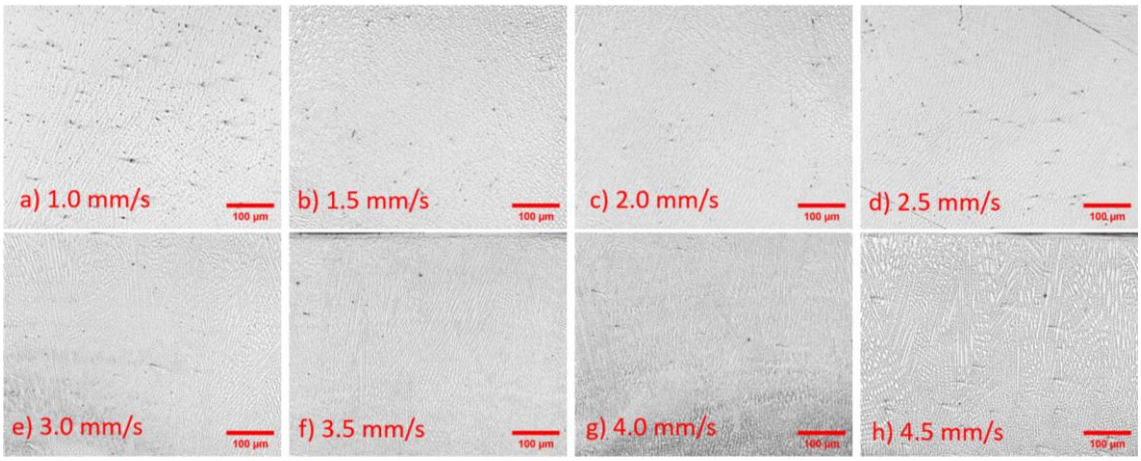

Figure 6-18 Microstructure of Inconel 625 created with various cooling rates with 20x magnification

Higher magnification images were captured to better demonstrate the changing microstructure in Figure 6-19. The samples with slower scanning speed correspond to lower cooling rates, and these feature equiaxed grains due to the slower dendrite growth. Dendrites in face centered cubic (FCC) nickel alloys, such as Inconel 625, grow fastest along the directions most closely aligned to the maximum temperature gradient [126]. Therefore, at slower scanning speeds, the dendrites are limited in their growth by the low thermal gradient due to the excessive heat. While the dendrites in the faster scanning speed samples are columnar due to the substrate acting as a heat sink. Note that the microstructure images displayed in Figure 6-18 and Figure 6-19 were captured at approximately the center of the deposition.

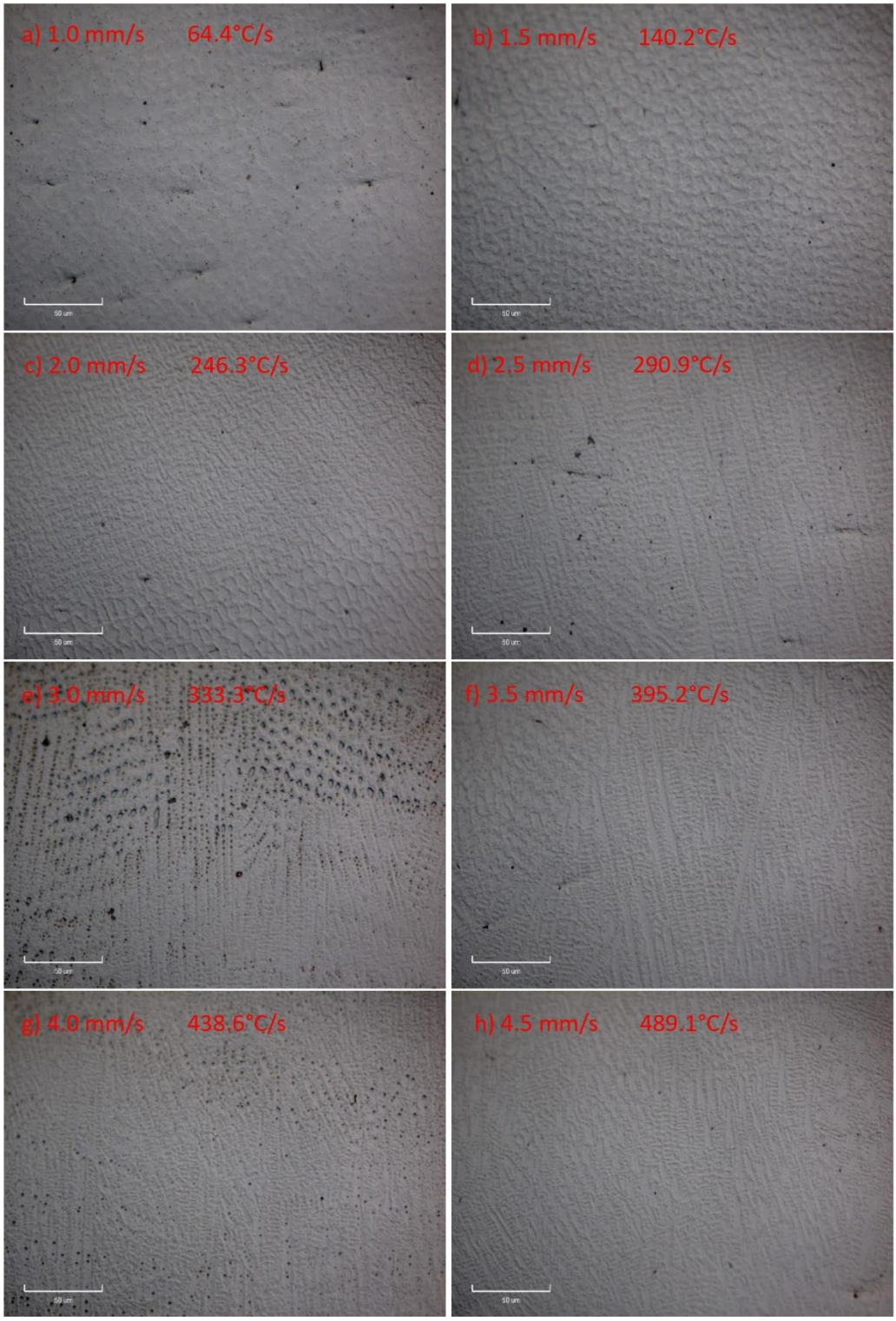

Figure 6-19 Microstructure of Inconel 625 created with corresponding cooling rates 50x magnification

The relationship between scanning speed and calculated cooling rate of Inconel 625 is summarized in Figure 6-20. The cooling rate calculation Eq. (6.6) shows that scanning speed and cooling rate are proportional, which is confirmed in this graph. Figure 6-21 demonstrates the relationship between the calculated cooling rate and measured Vickers hardness. Where the solid line refers to the mean hardness values and the highlighted region is the standard deviation of hardness measurements. The hardness increases linearly with cooling rate until approximately 300 °C/s, where the hardness appears to remain constant. The asymptote in the hardness is likely caused by the columnar dendrites approaching a steady state nucleation, where the dendrites will all form to be the same size at cooling rates above approximately 300 °C/s.

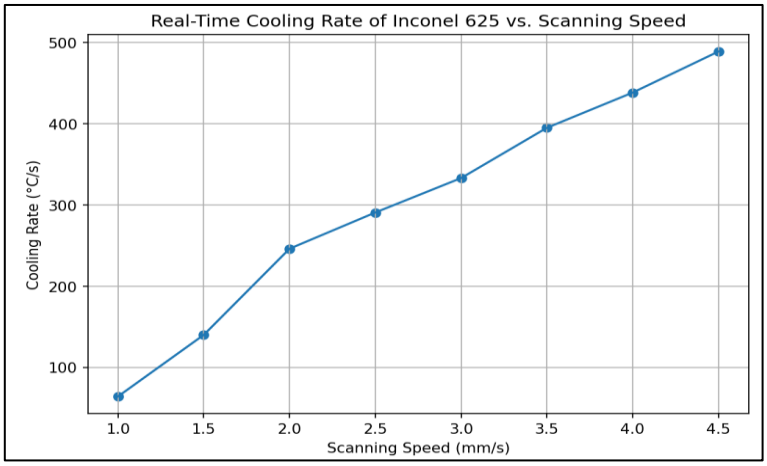

Figure 6-20 Relationship between scanning speed and cooling rate in Inconel 625

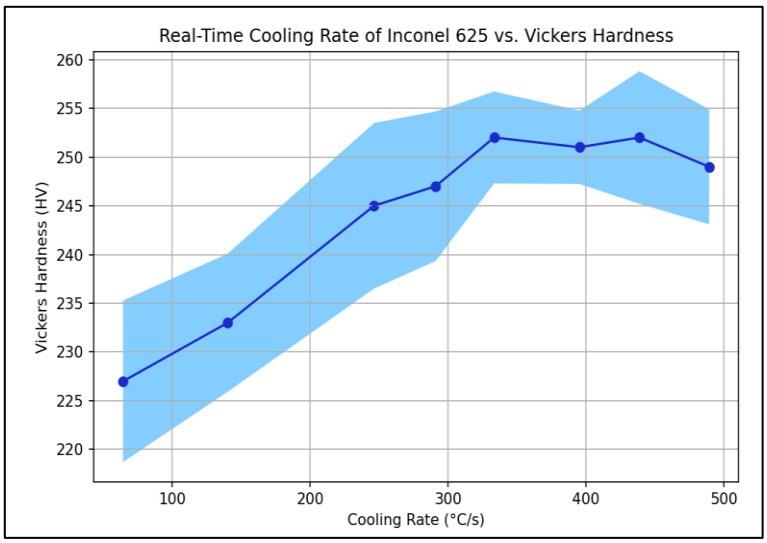

Figure 6-21 Relationship between cooling rate and Vickers hardness in Inconel 625

6.2 Monitoring of Laser Heat Treatment

LHT experiments were conducted to validate the MOC sensor's ability to monitor and control thermal dynamics. This set of experiments were performed on substrates of 6.3 mm thick 1018 cold-rolled steel with a laser spot diameter of 3mm. Prior to the experiment, the substrate was washed with ethanol and quenched in acetone for 10 seconds. The cleaning and quenching ensured there was no debris or accumulated heat that would alter the results. The scanning speed and laser power were different for each experiment to validate the measurements for various conditions and are shown in the accompanying graphs for each experiment.

6.2.1 Real-Time Monitoring of Laser Heat Treatment

Initial LHT experiments were conducted in open loop, where the scanning speed and laser power were set according to four cases. These four cases were: laser power ramp, laser power step, scanning speed ramp, and scanning speed step. In the two former cases the scanning speed was constant, while the laser power was constant in the two latter cases. The solidification time is shown compared to the process parameters in Figure 6-22 below.

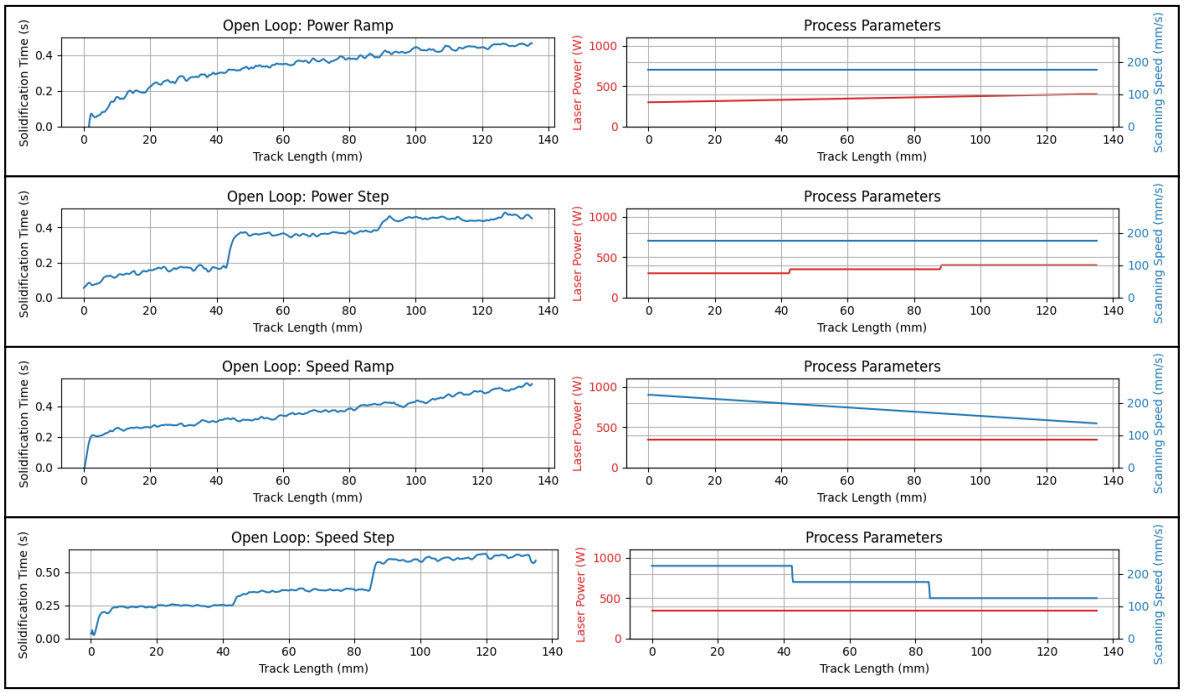

Figure 6-22 Real-time open loop solidification time and process parameters

As shown in the experiments in Figure 6-22 the solidification time is closely correlated to the process parameters. However, these represent ideal scenarios since the substrate was cleaned between each track and cooled to room temperature as described above. If the accumulated heat was considered, then the difference in solidification time, and therefore, the material properties would be more evident. Figure 6-23 below shows five adjacent tracks that were created consecutively with no cleaning or cooling between tracks. All tracks were created with a constant scanning speed of 3 mm/s and a constant laser power of 350W, with approximately 10 s between tracks.

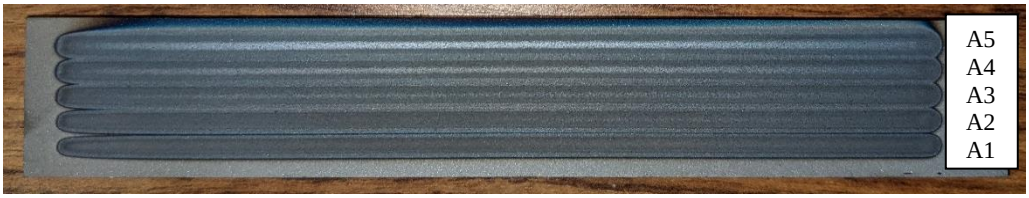

Figure 6-23 Consecutive open loop experiments (A1-A5)

Through visual inspection, the material differences are evident, as seen in the surface quality shown in Figure 6-23. Graphing the solidification time with the process parameters in Figure 6-24 demonstrates that despite constant process parameters, the solidification time of each track differs.

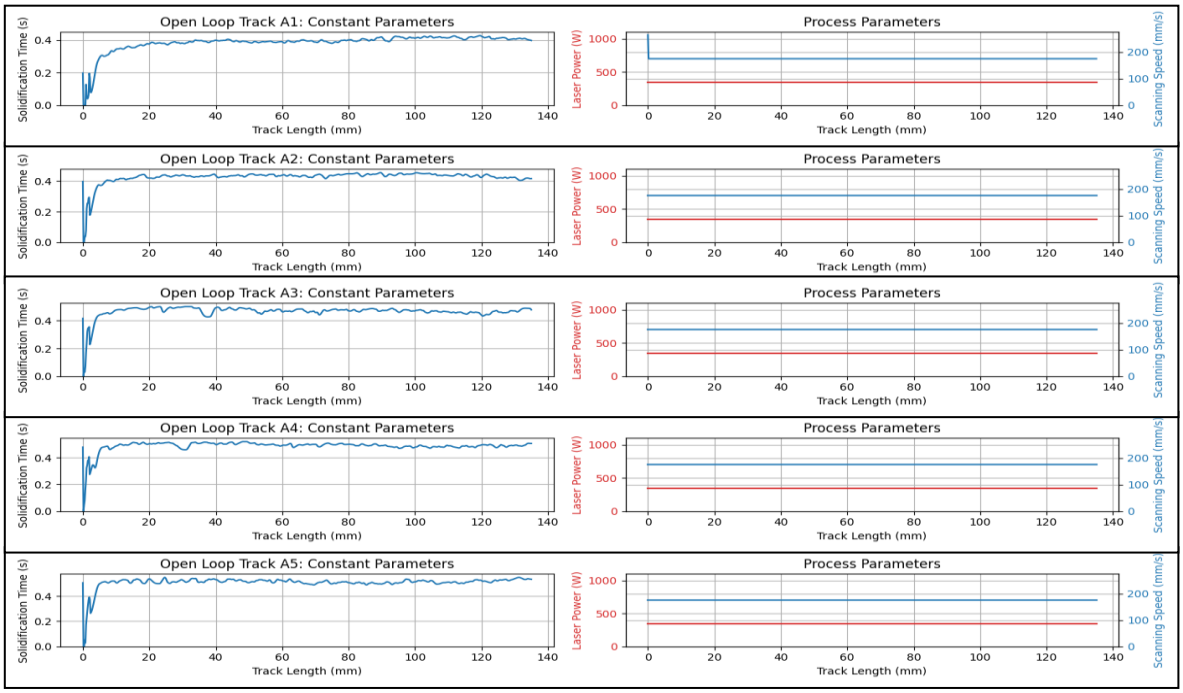

Figure 6-24 Real-time solidification time of five consecutive tracks on the same substrate with constant process parameters

In Table 6-5, the mean solidification of each track is shown to quantify the effect of the accumulated heat during LHT. This further supports the importance of real-time monitoring, so the changing material properties are known during manufacturing. Moreover, pairing these measurements with closed loop control would reduce the deviation and improve consistency in LHT.

Table 6-5 Mean solidification time for open loop tracks (B1-B5)

Track	A1	A2	A3	A4	A5
Mean Solidification Time (s)	0.384	0.426	0.466	0.487	0.509

6.2.2 Closed-Loop Control of Laser Heat Treatment

A proportional-integral (PI) controller was used to demonstrate the potential for using the MOC sensor measurements to correct errors. Here the scanning speed of the laser was controlled, since speed is inversely proportional to the solidification time, while the laser power remained in open loop. Figure 6-25 and Figure 6-26 show the effectiveness of PI control, with $k_p = -1500$ and $k_i = 0.002$. In the following figures, the left graph shows the solidification time while the right graph displays process parameters. The PI controller was tuned using the Ziegler-Nichols method.

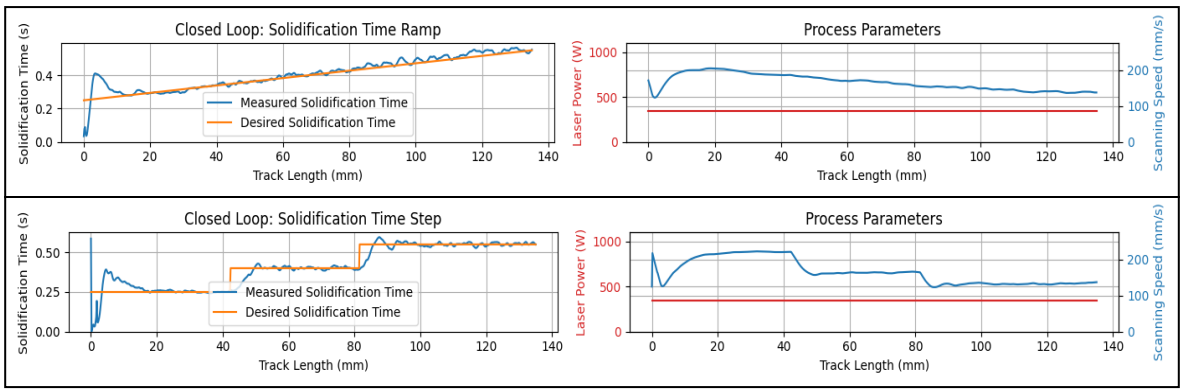

Figure 6-25 Closed loop control with changing solidification time set point

Figure 6-25 validates the effectiveness of using PI control with the measurements acquired from the MOC sensor to control the desired solidification time in real-time. Figure 6-26 demonstrates the ability for the PI controller to correct for disturbances in the process parameters, which are simulated by the changing laser power.

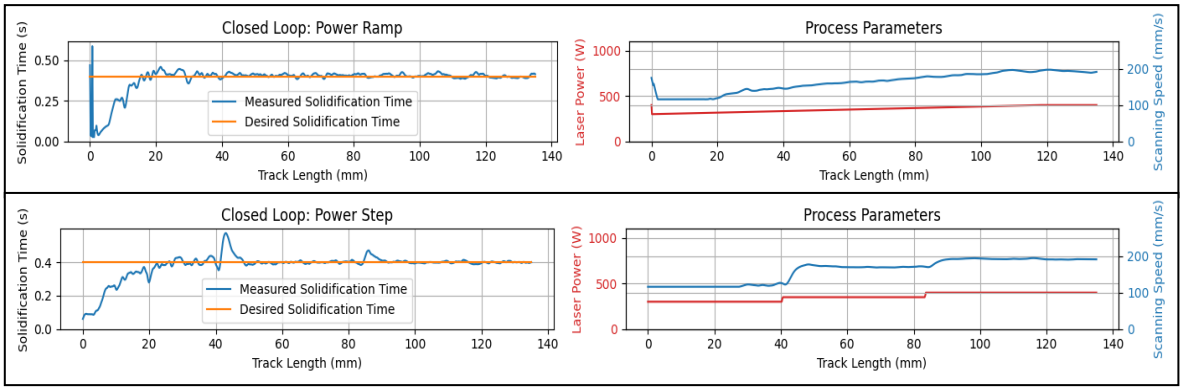

Figure 6-26 Closed loop solidification time control with changing laser power to simulate process disturbances

The control shown in Figure 6-25 and Figure 6-26 demonstrates the effectiveness of using the measurements from the MOC sensor to control the material properties. The variation in the scanning speed, shown in the right graph of the figures illustrates the controller correcting for the difference between actual and desired solidification time. Control can also be used to correct for the accumulated heat affect, which was shown to be a problem for consecutive tracks in the previous section. Each track was made with a set point of 0.4s for the solidification time and a constant laser power of 350W, with approximately 10 s between tracks, results are shown in Figure 6-27.

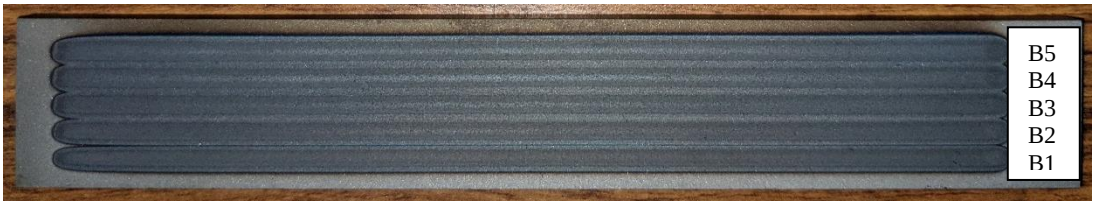

Figure 6-27 Consecutive closed loop tracks (B1-B5)

Visually, the tracks shown in Figure 6-27 appear to have a similar surface finish, which contrasts with the surface finish of the open loop tracks in Figure 6-23. The solidification time is plotted in Figure 6-28, where the solidification time is similar to the set point for all tracks. Thus, the solidification time measured from the MOC sensor demonstrates that the consistent solidification time measurements correlate to a similar surface finish.

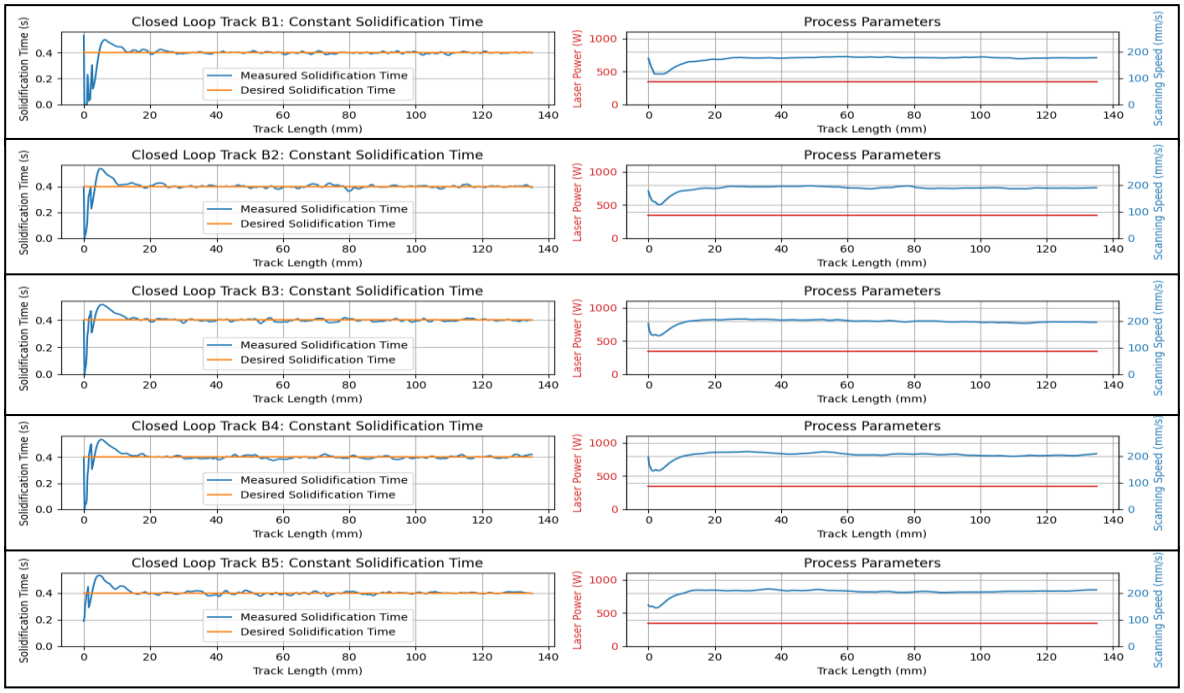

Figure 6-28 Real-time solidification time of five consecutive tracks on the same substrate with closed-loop control

Table 6-6 shows the mean solidification time for each of the tracks and the mean scanning speed, indicating that the speed is increased between tracks to accommodate for the accumulated heat affect. This is supported by the open loop solidification times in Table 6-5 and the general formula for steady state solidification time shown in Section 6.1. Previously, the solidification time was shown to increase between each track with constant parameters, and since steady state solidification time is inversely proportional to scanning speed, the speed should increase to correct for this deviation. Since this is shown empirically, it demonstrates the potential of using the MOC sensor measurements for material property prediction and control.

Table 6-6 Mean solidification time for closed loop tracks (D1-D5)

Track	B1	B2	B3	B4	B5
Mean Solidification Time (s)	0.397	0.401	0.402	0.403	0.403
Mean Scanning Speed (mm/min)	173.03	187.38	197.50	204.11	204.62

The MOC appears to predict the material properties of parts produced with thermal processes by monitoring the solidification time as demonstrated in [43] - [51]. Initially, it was shown that solidification time is influenced by the process parameters. Furthermore, under constant parameters,

the solidification time is affected by accumulated heat in the substrate since thermal processes feature concentrated high energy sources, such as a laser in LHT. The accumulated heat affect is demonstrated in the surface of the substrate in Figure 6-23 and in the process data graphed in Figure 6-24. Hence, monitoring the solidification time with an IR sensor is shown to be an effective method to predict the material properties of thermal processing parts. The measured solidification time can also be used to control the material properties of the final part, which further legitimizes the calculation. The surface of the substrate in Figure 6-27 indicates that the material properties are consistent across all the tracks and the experimental data in Figure 6-28 shows the corresponding solidification time to further support the calculations. Therefore, solidification time, as measured by the MOC sensor, is determined to be suitable in measuring the solidification time, which is essential for predicting and controlling the material properties of a part created through thermal processes.

6.3 Monitoring of Laser Directed Energy Deposition

LDED experiments were conducted to validate the MOC sensor's ability to monitor and control geometry. This set of experiments validated real-time height and width measurements with single-track geometry. Measurements from the MOC sensor were integrated with PI control to demonstrate the potential for using this system with closed-loop control. Multi-layer performance of height monitoring has been validated as well, with 431 stainless steel powder and Inconel 625.

6.3.1 Single-Track Geometry Monitoring

Similar to LHT, LDED experiments were conducted in open loop, where the scanning speed and laser power were set according to four cases. These four cases were: laser power ramp, laser power step, scanning speed ramp, and scanning speed step. In the two former cases the scanning speed was constant, while the laser power was constant in the two latter cases. The height and width measurements from the MOC sensor are shown in the left graph of Figure 6-29, with the solidification time shown in the middle, and the process parameters in the right graphs. This set of experiments were performed on substrates of 6.3 mm thick 1018 cold-rolled steel with a laser spot diameter of 3mm. Prior to the experiment, the substrate was washed with ethanol and quenched in acetone for 10 seconds. The cleaning and quenching ensured there was no debris or accumulated heat that would alter the results.

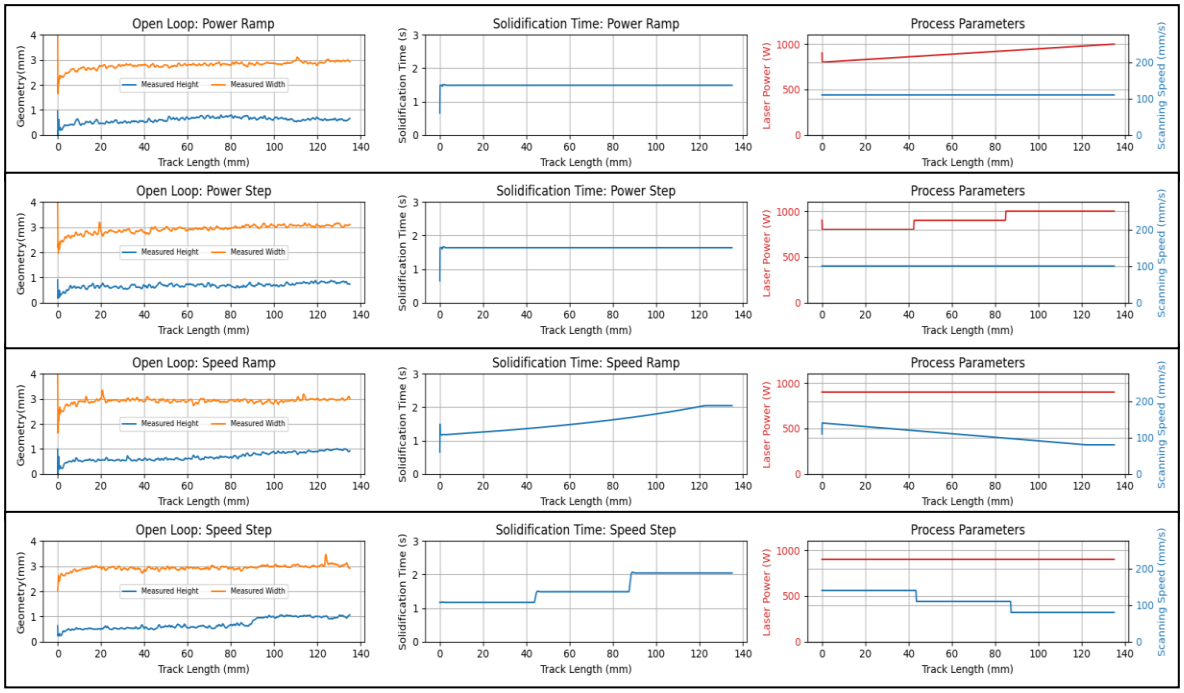

Figure 6-29 Real-time open loop geometry measurements and process parameters

In Figure 6-29 the scanning speed is shown to have a large influence on the measured height, while changes in the laser power have a smaller effect. Since the height appears to be inversely correlated to the scanning speed and the height variation shown in Figure 5-8 it may be effective to correct the height errors by controlling the scanning speed. The relationship between the height and scanning speed may be that a slower speed allows more time for the added material to fuse to the substrate, resulting in a larger clad. Furthermore, it is shown that the width remains consistent at approximately 3mm across all the experiments, this indicates that the width of the clad is mostly influenced by the laser diameter. Therefore, it is most critical to monitor and control the height during LMP to ensure the consistency of parts; though, as shown in Section 5.1, the MOC system can monitor the height and width in real-time.

6.3.2 Single-Track Geometry Closed-Loop Control

To demonstrate the effectiveness of using the MOC sensor measurements, the open loop experiments were modified to include closed loop control. In this section, only single-input single-output (SISO) control is considered, and since there is more deviation in the height, that is chosen as the controlled parameter. A PI controller was added to the system to control scanning speed, since speed was found to have a greater effect on the height of the clad, while the laser power remained in open loop. PI control

was implemented with $k_p = -300$ and $k_i = 0.001$, as found with the Ziegler-Nichols method, to control the desired height and correct process disturbances. Since only the height is being controlled Figure 6-30 shows the measured and desired height on the left, solidification time in the middle graphs, and process parameters to the right.

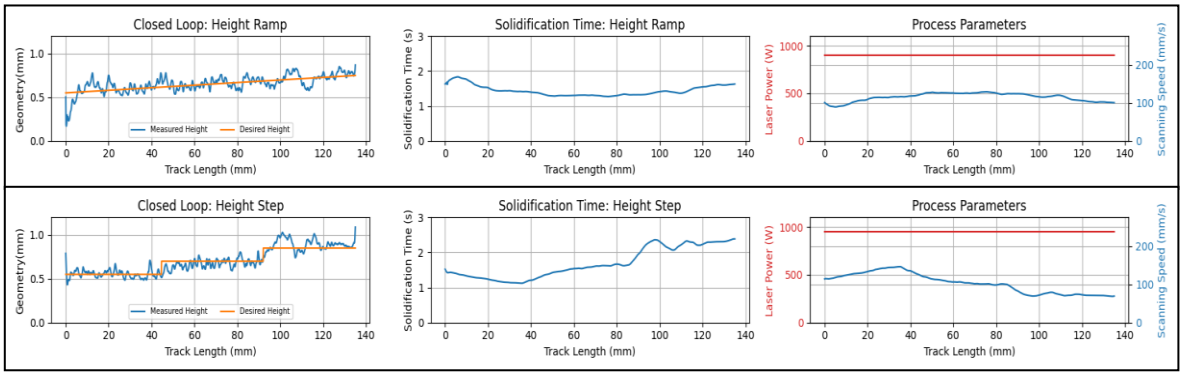

Figure 6-30 Closed loop control with changing height set point

The PI controller's performance regarding a set point for the height is shown in Figure 6-30, where the height was set to linearly increase from 0.55mm to 0.75mm and a step change from 0.55mm to 0.7mm to 0.85mm. There is noticeable deviation between the desired height and measured height, which indicates that the controller gains should be tuned to optimize performance. The solidification time calculations shown in the graph appear to be inversely proportional to the scanning speed, which validates the solidification time monitoring for LDED, since only LHT was shown previously. Again, control can also be used to correct process disturbances when the set point is constant. These results are shown in the experiments graphed in Figure 6-31 where the height was set to a constant 0.65mm and disturbances were introduced by changing the laser power.

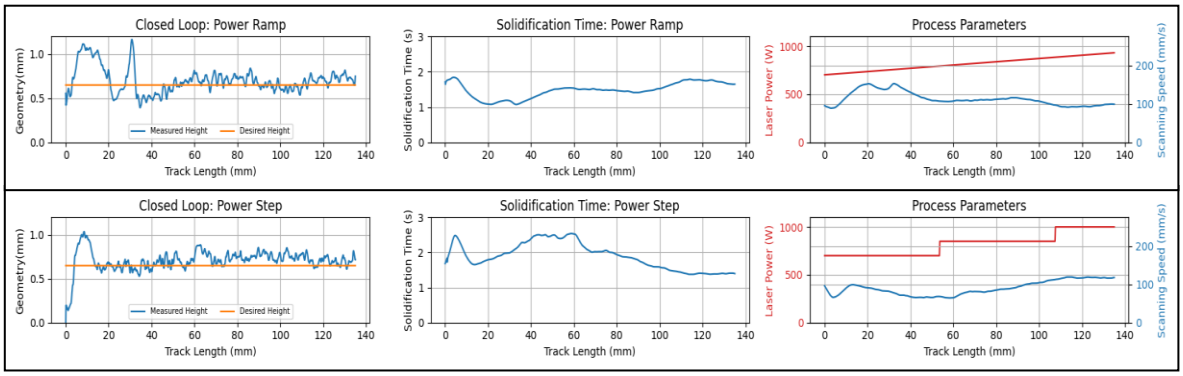

Figure 6-31 Closed loop height control with changing laser power to simulate process disturbances

The height controlled against process disturbances indicates significant overshoot in the beginning of the process, which confirms that the controller gains need to be tuned. However, once the overshoot is corrected the controller can reduce the effect of changing laser power. These results show that with further tuning the height can be controlled during LMP with the MOC sensor's calculations described in Section 5.1. Since the variation in closed loop geometry measurements is significantly higher than the variation of open loop measurements, indicating that poorly optimized control is the cause of this noise in this data and not the MOC sensor calculations. Therefore, geometry prediction by the MOC sensor, is determined to be suitable for fabricating more reliable parts through thermal processes, though the PI controller's performance is not ideal.

6.3.3 Multi-Track Geometry Prediction Performance

To validate the performance of the geometry prediction algorithm described in Section 5.3, four experiments were conducted using intermediate values from the dataset used to train, validate, and test the CNN. This set of experiments were conducted with a constant laser power of 1 kW, Table 6-7 describes the other process parameters, where the distinction between thin-walled and cuboid part geometry was described in Section 5.3.1. Each experiment featured 6 tracks, where each track was 50 mm long.

Table 6-7 Experiments conducted to validate the multi-track geometry prediction CNN

Experiment Number	Scanning Speed	Material	Part Geometry
1	2.0 mm/s	431 stainless-steel	Thin wall
2	2.0 mm/s	431 stainless-steel	Cuboid
3	2.0 mm/s	Inconel 625	Thin wall
4	2.0 mm/s	Inconel 625	Cuboid

This dataset features 4 experiments with 6 tracks each, so there were 24 tracks to analyze in total. Running the CNN with this entire dataset results in an MSE of 0.0063 and a MAE of 0.0555, where each timestep was computed with an average time of 13 ms. The MAPE, which is a more intuitive metric of performance, was found to be 10.25% for this dataset. This performance is summarized in Figure 6-32 where all 24 tracks are shown sequentially to consolidate the data.

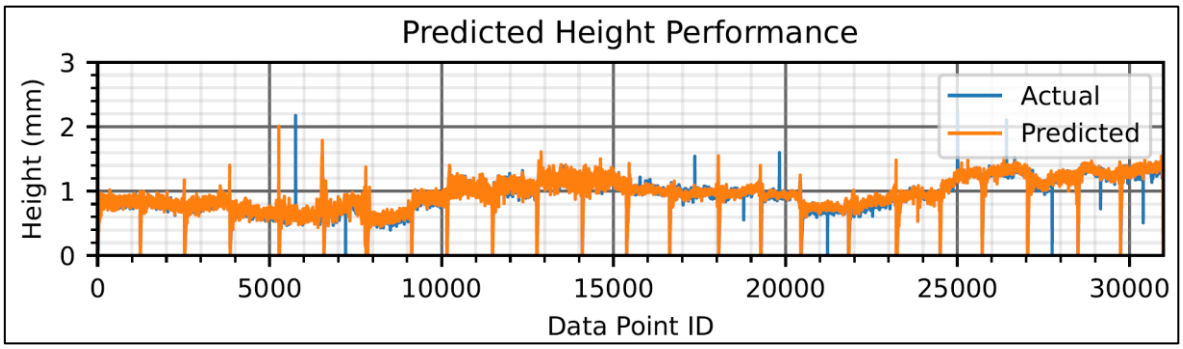

Figure 6-32 Multi-track height prediction performance

Figure 6-32 demonstrates that the predicted height values follow the same trend as the macro-imaging measurements used to validate this algorithm. Also note that the data points that approach zero represent the beginning of each track where the clad is forming and therefore does not have a height. To visualize the performance of multiple tracks, the thin-walled experiments are highlighted in Figure 6-33 and Figure 6-34. The 431 stainless steel has a MAPE of 6.13%, while the Inconel 625 has a MAPE of 3.64%. These figures also demonstrate that this algorithm is robust enough to monitor the height of multiple layers with minimal accumulation of error. These experiments were selected from the test set, however, the process parameters used in these experiments were also used in the training and validation sets.

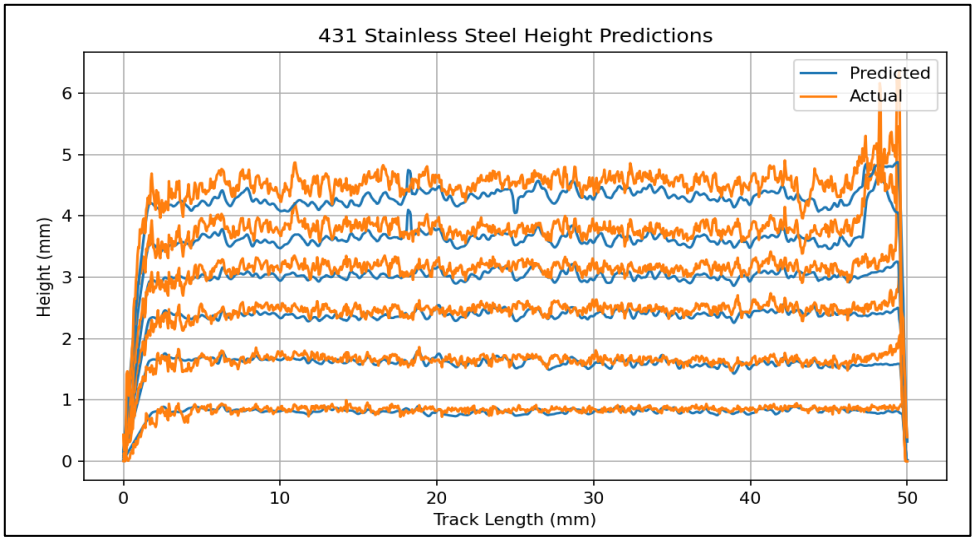

Figure 6-33 Predicted and Actual Height of a 6-layer thin-walled specimen of 431 Stainless Steel

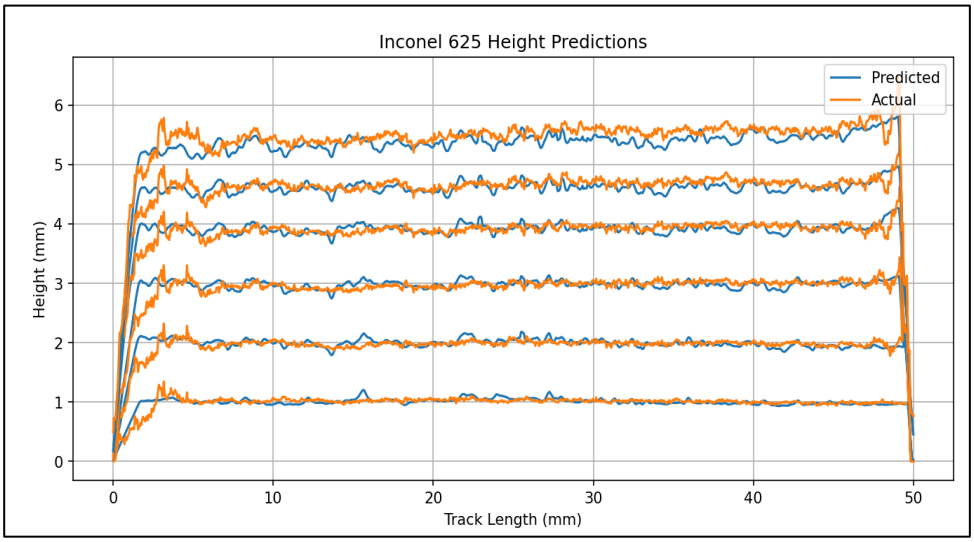

Figure 6-34 Predicted and Actual Height of a 6-layer thin-walled specimen of Inconel 625

Furthermore, applying a Butterworth filter removes some of the high frequency noise as shown in Figure 6-35 and Figure 6-36. Where the corresponding MAPE values for 431 stainless steel and Inconel 625 are 4.89% and 2.71% respectively.

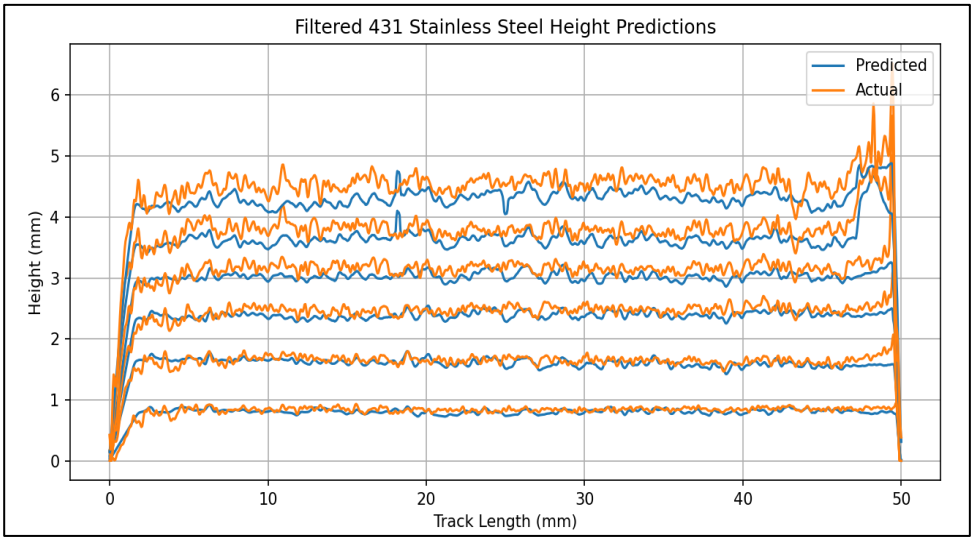

Figure 6-35 Predicted and Actual Height of a 6-layer thin-walled specimen of 431 stainless steel with Butterworth filter

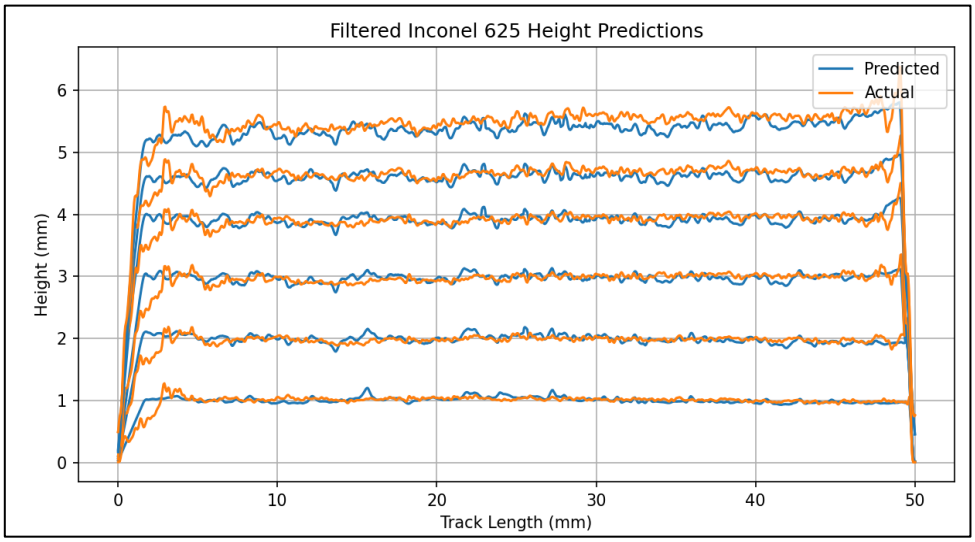

Figure 6-36 Predicted and Actual Height of a 6-layer thin-walled specimen of Inconel 625 with Butterworth filter

Therefore, the height prediction was shown to have a MAPE of 10.25% with a CNN that only uses data extracted from visible-light images for the prediction. Moreover, this algorithm was shown to be robust enough to monitor different materials and different part geometries, featuring both thin-walled sections and cuboids that feature overlapping tracks. This CNN has also been shown to be suitable for in-situ monitoring since the computation takes an average of 12 ms. Finally, the integration of a Butterworth filter also improves the accuracy of height predictions, except at the beginning of the melt pool, where the filter dampens the initial height predictions. However, using extra frames in this region may reduce the dampening effect caused by the Butterworth filter.

6.4 Real-Time Monitoring of Gas Metal Arc Welding

A major goal of this research is to build a system versatile enough to be used in different processes; therefore, GMAW was used to demonstrate the potential of monitoring a thermal process with parameters. GMAW uses an electric arc as the concentrated energy source, as opposed to the previously explored laser. Another notable difference in these processes is the form factor of the added material. Previously, powder-based feedstock was considered, while in this section wire-fed processes are explored. Therefore, validation of the MOC sensor in monitoring key features during GMAW demonstrates the robustness of the tools developed in this research.

6.4.1 Comparison of Double Cooled Wire and Gas Metal Arc Welding

Results shown here involve an electrode wire and base metal with chemistries consistent with plain carbon steel; a standard pulsed GMAW program in a Lincoln PowerWave R500 welding power source for all the welds, in conjunction with a Fanuc robotic arm, and performed at CAMJ. The shielding gas used was 100% Argon with ultra-high purity at the flow of 19 L/min. The welding electrical parameters were selected such that the wire feed rate was at 7.6 m/min, while the travel speed was at 13.5 mm/s for the various experiments conducted, the contact tip to workpiece distance (CTWD) was kept at 19 mm. GMAW experiments were conducted using a standard torch at straight position, and compared to one modified with two cold wires added to the arc as well which leaded the arc during welding, referred to as double cold wire (DCW-GMAW) [127].

The auxiliary wires were fed at 40 % of the mass deposited through the electrode wire, 6.3 m/min. Therefore, in total 20.2 m/min were deposited during welding. Voltage was set to 28V during welding, the nominal heat input was targeted to be approximately 665 J/min. The welds were deposited in hot-rolled plain carbon steel (AISI 1020), the wire electrode was 1.2 mm ER70S-6, and the cold wires were 0.9 mm ER70S-6 as well.

The experimental setup is shown below in Figure 6-37, demonstrating the relative position between the MOC sensor and the HAZ. The MOC sensor was used to observe the HAZ during welding at rates of at least 20 frames per second, allowing one to observe the geometry using the higher resolution visible light sensor, and the thermal dynamics of the process in real-time with the IR sensor. Therefore, the quality of the weld can be determined in real-time through processing these images to extract the most notable properties.

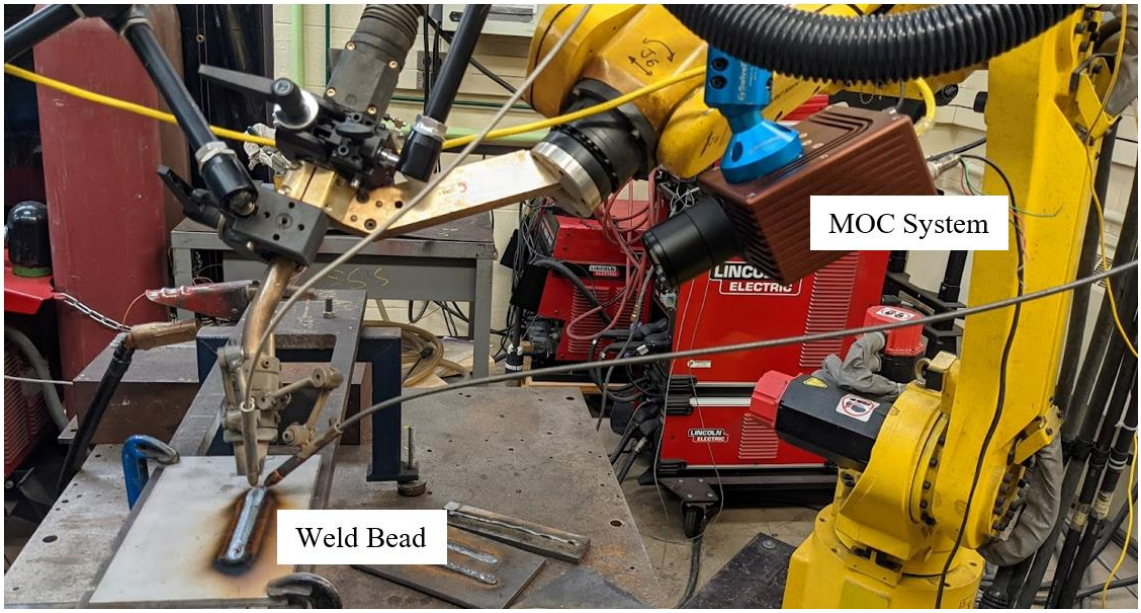

Figure 6-37 Experimental setup featuring the position of the MOC system relative to the weld bead. Since the sensor and electrode are mounted to the same arm the relative position of the camera to the heat affected zone is the consistent throughout the process

In real-time, the MOC System predicted width of the weld bead using images captured with the visible light camera. Thresholding was used to differentiate the weld bead from the surrounding background. Then, since the relative position of MOC system is known, the width was calculated by transforming the image onto the global coordinate system.

The difference in temperature at two locations can be taken as shown in Figure 6-38. The temperature decreases further from the arc because the heat is transferred away from the hottest region as described by thermodynamics. The temperatures of two points, one closer to the arc and one farther from it can be used to calculate the cooling rate, which is assumed to be dependent on the heat conducting through the material. Therefore, the temperature distribution allows for the cooling rate to be calculated based on Eq. (6.6)

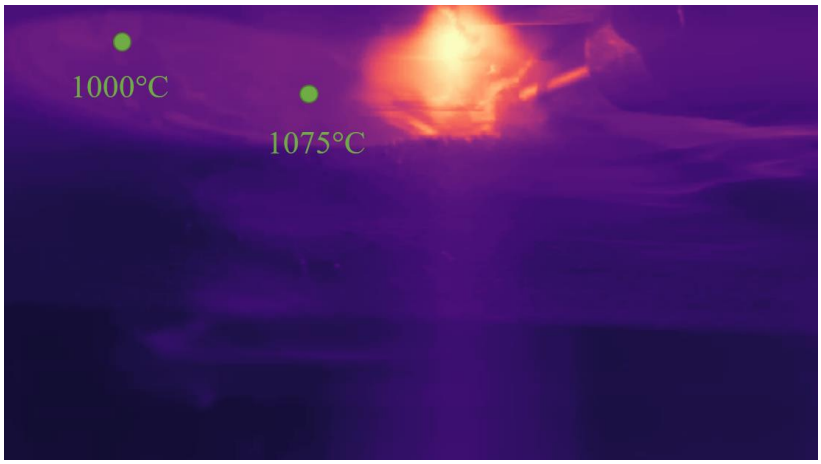

Figure 6-38 Areas of interest demonstrated key temperatures that can be used to calculate the cooling rate of the process

Two sets of experiments were conducted, one run with two cold wires added as well, and one run with only the electrode wire. Using these runs with different parameters allowed the results to be compared to highlight the difference in these processes. The measured cooling rates for both processes are compared in Figure 6-39.

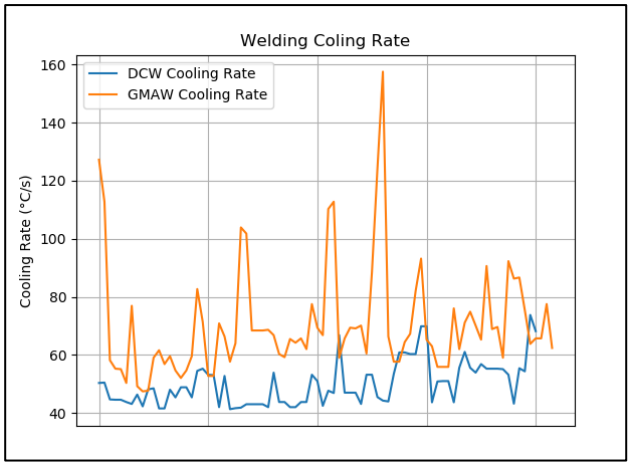

Figure 6-39 Real-time cooling rate comparison during GMAW (orange) and DCW (blue)

There is a notable difference between the cooling rate measured through GMAW and DCW-GMAW. The noise shown in the cooling rate measurements is due to the randomness of plasma moving in the arc which changes the illumination of the melt pool, and therefore, the temperature measurements as well. Though both experiments feature noise, the average cooling rate shows significant difference with an average cooling rate of 70.83 °C/s for GMAW and 50.01 °C/s for DCW-GMAW. The variance in

the signal may be caused by the temperature at the two locations being too close. To achieve more consistent measurements the temperature distribution captured from the infrared sensor must be improved. Applying filters and selecting the correct camera settings to reduce the influence of emissivity may result in more accurate temperature distribution measurements, to reduce the variance in the cooling rate calculation. The microstructures for each experiment are shown in Figure 6-40, which demonstrates that the different welding processes will lead to different microstructures which are corresponding to the differences in cooling rate. These microstructures as expected are ferritic with the DCW-GMAW showing a more refined microstructural pattern consistent with a higher cooling rate. Moreover, primary ferrite (PF(G)) fraction at the grain boundaries was reduced with is also consistent with an increase in cooling rate in DCW-GMAW [44].

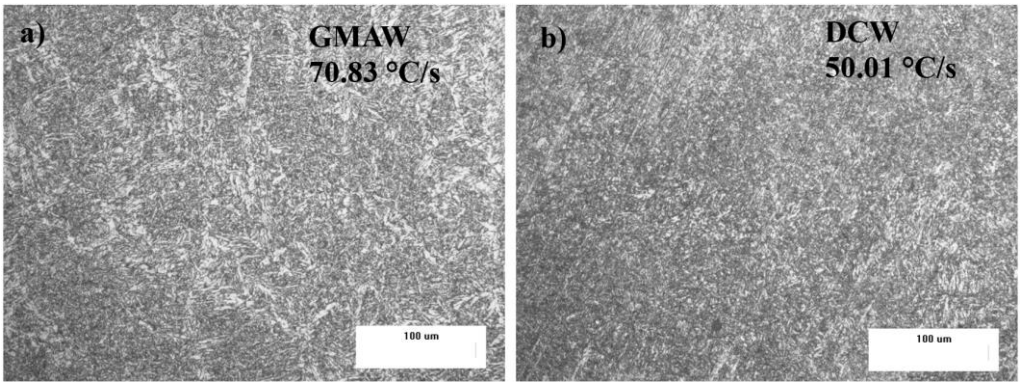

Figure 6-40 a) Microstructure produced during GMAW with an average cooling rate of 70.83 °C/s. b) Microstructure produced during DCW with an average cooling rate of 50.01 °C/s. The different cooling rates correspond to different microstructure and therefore, different material properties

The images captured to predict the geometry of the process are shown in Figure 6-41. The arc is shown to have sufficient brightness to saturate both imaging sensors where the electrode interacts with the base metal. However, the weld bead is clearly visible with both sensors after the arc while the metal is still heated. Therefore, this location was monitored to estimate the width of the weld bead in real-time, based on the size of the bead visible in the image and the position of the MOC sensor. This is similar in experimental setup to weld bead height measurement highlighted by Xia et al. [128].

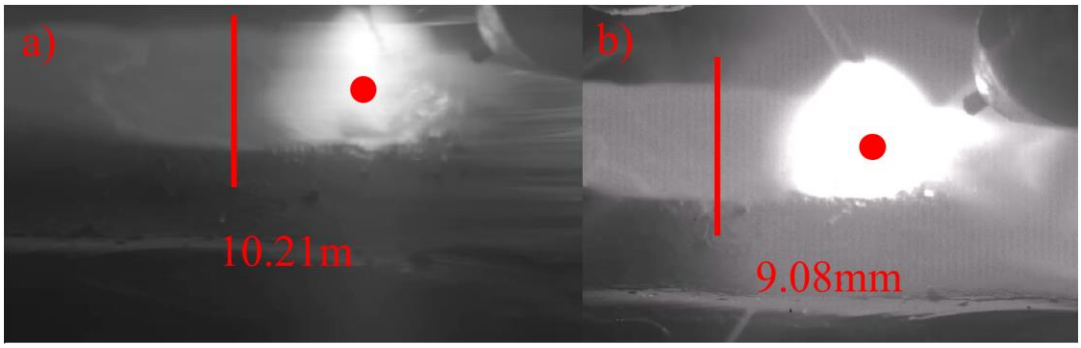

Figure 6-41 a) Images captured during GMAW with the infrared light sensor, since the arc is too bright at the melt pool, the geometry of the heat affected zone is more clearly visible approximately 10.21mm behind the arc. b) Images captured during GMAW with the visible light sensor, since the arc is too bright at the heat affected zone, the geometry of the heat affected zone is more clearly visible approximately 9.08mm behind the arc.

To validate the geometry measurements, bead width was measured with the high-resolution images shown in Figure 6-42, where the scale of 6mm is shown in the bottom right. The scale is used to determine the width of the weld bead at all locations during the track. Moreover, since the frame rate of the camera and travelling speed are known the measured width can be synchronized to the corresponding real-time images at every time step.

Figure 6-42 a) Aerial view of the weld bead produced during GMAW taken after the experiment to measure its width. b) Aerial view of the weld bead produced during DCW-GMAW taken after the experiment to measure its width.

At each time step, the width is predicted by projecting the view of the camera based on its position relative to the HAZ. The measured width is compared to the predicted width from the infrared images and vision images such as in Figure 6-41. The outliers in the geometry predictions are likely caused by

poorly optimized camera settings. Selecting more appropriate camera settings or changing the image processing may reduce the effect of these outliers and improve the geometry prediction.

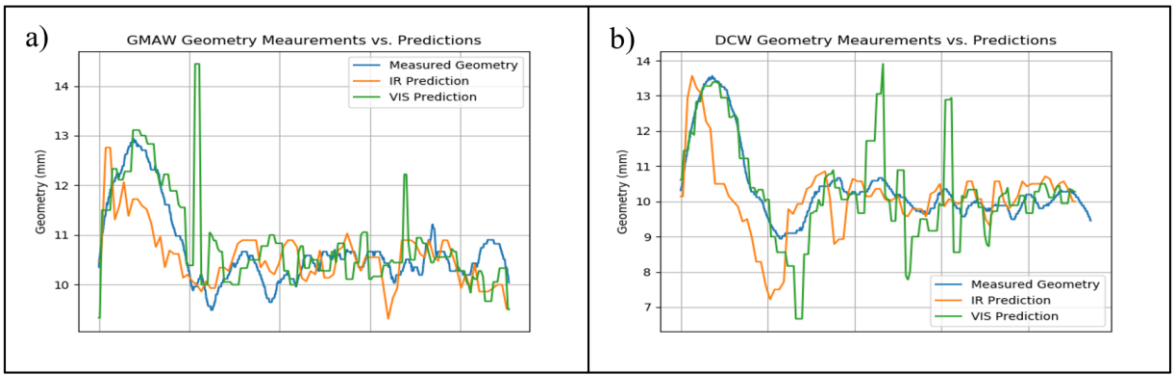

Figure 6-43 a) Comparison of measured and predicted width during GMAW. b) Comparison of measured and predicted width during DCW. Note that the blue line represents the measured width, orange line is the width prediction using infrared light, and green predictions are generated from visible light images.

From the results presented here, it is clear that observing the melt pool with both visible and infrared camera sensors has the benefit of monitoring both the geometry (e.g. bead width) and cooling rate in real time. Vision camera sensors have a higher resolution which allows for more accurate geometry prediction, while the infrared camera can provide the temperature distribution of the HAZ which is used to predict the microstructure. Both sensors sharing the same field of view allows the system to be more compact, easy to set up, and ensures that the relative position to the arc is consistent throughout the track.

These tests show the great potential to use simultaneous monitoring in both the IR and visible light spectrums to simultaneous monitor the geometry and cooling rate in real time. Though there is noise in the current signals, modifying the sensor settings and improving the image processing will reduce the noise and improve the real-time predictions. The results shown here are merely to provide some insights gained from recent work, and an indication of future directions viable in this field.

6.4.2 Hybrid Laser Arc Welding Monitoring

To validate the MOC sensor on different thermal processes, real-time cooling rate monitoring was performed on hybrid arc processes as well. These experiments were conducted with the setup described in Section 0 using 1.1 mm diameter copper coated MIG wire as the feedstock, added with a feed rate of 150 inches per minute (63.5 mm/s) with the other process parameters detailed in Table 6-8. The

voltage modes were run using preset parameters from the original equipment manufacturer (OEM) Lincoln Electric. Figure 6-44 demonstrates one frame captured during the Rapid Arc process described below to illustrate the quality of images captured with the MOC sensor. Just as in Section 6.1, the visible-light image is used to estimate the temperature distribution to calculate the cooling rate.

Table 6-8 Hybrid arc welding process parameters

Laser Power	Voltage	Voltage Mode	Scanning Speed	Average Cooling Rate
4 kW	12 V	Pulse	4.23 mm/s	77.8
0 kW	12 V	Constant	6.35 mm/s	147.1
2 kW	12 V	Constant	6.35 mm/s	133.9
2 kW	20 V	Low Fume Pulse	8.47 mm/s	206.0
2 kW	20 V	Rapid Arc	8.47 mm/s	201.5

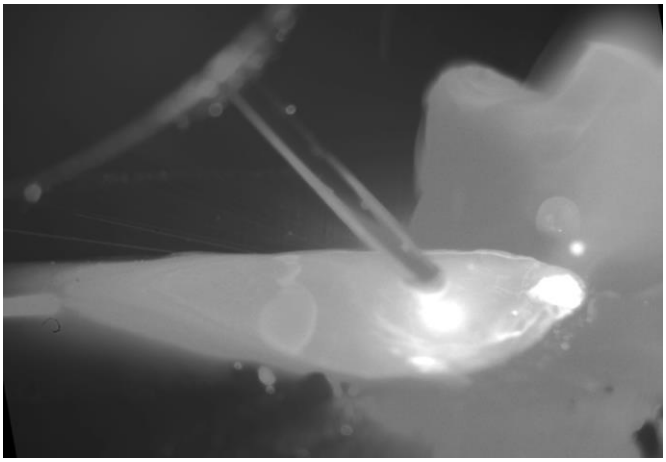

Figure 6-44 Visible-light image captured during Rapid Arc hybrid welding

The average cooling rate of each experiment is noted in Table 6-8, while the real-time cooling rate is graphed in Figure 6-45. The length of each track is determined by setting a start and end position before deposition, resulting in a different length for each track. Therefore, the length of each track is omitted from the below diagram. The calculated cooling rate is within the range of cooling rates observed for stainless steel in Section 6.1.2, which is to be expected since the feedstock wire is an iron-based alloy as well. Analyzing the average cooling rate shows that experiments which feature more input energy have a lower average cooling rate, which is reasonable because the added energy will pre-heat the material and reduce the efficiency of heat conduction away from the melt pool. Additionally, since the cooling rate calculation is localized, the added heat to the melt pool would increase the solidification time, which also contributes to the higher cooling rate calculation. Since the cooling rate

was shown to correlate to material properties in Section 6.3.1, the MOC sensor appears to be sufficient in monitoring the material properties of GMAW and hybrid processes, in addition to LDED.

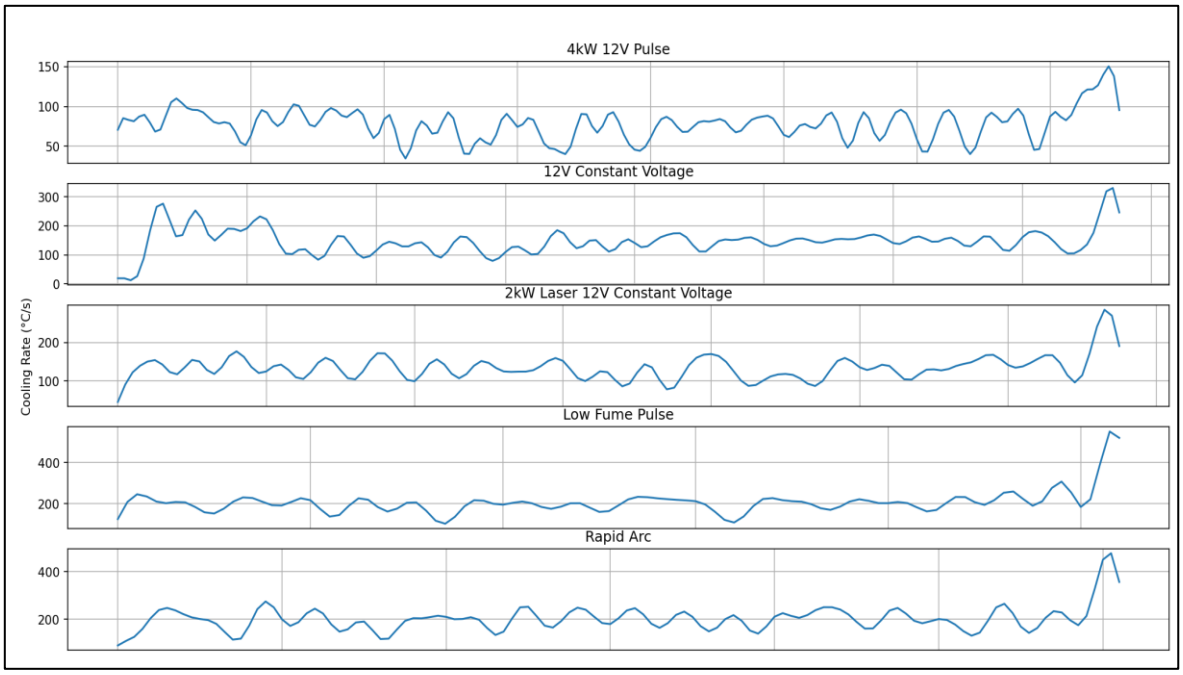

Figure 6-45 Real-time cooling rate of hybrid welding

6.5 Summary

This chapter describes how the temperature measurements captured from the MOC sensor were used to calculate thermal dynamics, namely the heating and cooling rates. Moreover, experiments were conducted featuring these measurements captured in real time and the corresponding microstructure and material properties of both 431 stainless steel and Inconel 625. These experiments were conducted with iron-based and nickel-based alloys to demonstrate that the methodology is general enough to work with materials that have different properties. Furthermore, since the temperatures used in these calculations were based on the predictions outlined in Section 4.2, it was shown that these temperature predictions are suitable for real-time microstructure measurements in thermal processes.

Real-time measurements are critical for control algorithms; hence, it was shown that these measurements are sufficient to be used with PI controllers to correct deviations in LAM and LHT. SISO control has been achieved with measurements from the MOC sensor, where the cooling rate was controlled in LHT by adjusting the scanning speed to correct for the accumulated heat effect. During LAM, a PI controller was used to correct the height calculated with the MOC sensor by adjusting the

scanning speed. In both examples, step and ramp input laser profiles were implemented during the track to validate the effectiveness at compensating for process disturbances. It was found that the PI controllers could correct these disturbances by adjusting the scanning speed to keep the controlled variable at the set point. Moreover, the height prediction CNN was also demonstrated to be robust enough to monitor different part geometry and materials while computing each step at an average time of 12 ms.

Finally, this chapter demonstrated the versatility of the MOC sensor, by showing real-time measurements captured in GMAW. Thus, the objective to create a monitoring system that can be used on a variety of thermal processes has been achieved in this work. The MOC sensor was used to monitor data during LAM, LHT, GMAW, and hybrid (laser and arc) welding processes. During GMAW, the cooling rate was calculated, and the geometry was monitored in the form of width measurements, which is critical to ensure the quality of the weld bead. Cooling rate calculations were also conducted with hybrid welding using various voltage parameters to further demonstrate the versatility of the MOC sensor's measurements.

Chapter 7
Conclusions and Future Work

7.1 Conclusions

In this research, a monitoring system capable of estimating geometry and material properties during thermal processes was developed. Conclusions and contributions of this work are summarized in the following:

- The MOC sensor was developed to be used as a monitoring system for various thermal processes and materials. The unit features a visible light and IR camera sensors to capture high resolution images for geometry predictions and the temperature distributions for material properties prediction. The system was designed with a single optical path to ensure the images of both sensors are comparable and is especially made for the conditions of thermal processes with considerations for the relevant hazards and process conditions.
- In single-track experiments, it has been shown that the height and width of the deposition can be monitored by estimating the shape of the clad. Assuming that the cross-section of the melt pool has a circular shape, the height and width of the clad can be estimated from the captured images.
- ML has been implemented to predict the height and width of the deposition in LDED. Since the appearance of the melt pool is influenced by the geometry of previous layers, it is complex to assume the shape of the melt pool in these cases. Hence, ML was utilized to predict the height and width of the deposition without prior knowledge of the general shape of the deposition. This algorithm has been shown to predict the height with a MAPE of 12.4%. Moreover, this allows for geometric defects to be detected.
- A more cost-effective version of the MOC sensor was created by replacing the IR camera sensor with a pyrometer. It has been shown that visible light images can be augmented with pyrometer measurements to estimate the temperature distribution of the HAZ. Initially, it was shown that visible light images and gradient boosted trees could be used to calculate the approximate temperature around the heat affected zone. Simultaneously, a pyrometer was used to determine the peak temperature at the middle of the melt pool. Finally, a model based on the

generalized heat conduction equation was used to calculate the intermediate temperatures to estimate the distribution over the entire HAZ.

- Utilizing Planck's law allows for the vision camera to estimate the temperature distribution of the HAZ. This improves the temperature prediction by removing the need to have process simplifications when using the generalized heat conduction thermal model. Moreover, this allows the temperature predictions to be invariant to the energy source and material properties, where these parameters were essential in the model-based approach.
- Visible light-based temperature predictions were then further optimized by using calibrated pyrometer measurements to tune the emissivity of the thermal distribution. Comparing the estimated temperature distribution to the corresponding pyrometer measurement allows for emissivity to be calculated from the difference to improve the accuracy of the prediction.
- It has been shown that monitoring thermal dynamics with this system is sufficient in estimating the material properties of the final products. Therefore, this tool can be used to indirectly monitor and eventually control material properties for more consistent products built with thermal processes.
- The measurements from the MOC sensor have been used in conjunction with a PI controller to validate that the system can be used for closed loop control. The potential for integration with a control algorithm is significant since it allows for the opportunity to be used in correcting errors and not just in error detection.
- It has been shown that monitoring can be utilized with multiple different materials. With geometry and thermal dynamics monitored with different steel and nickel-based alloys. Moreover, the form factor of the feedstock was changed with different experiments, having both powder-fed and wire-fed processes monitored in this research. This shows the potential to address one of the major objectives of this research which is to develop the monitor system to be invariant to the feedstock material.
- Monitoring has been implemented in LHT, LDED, and GMAW, which demonstrates the flexibility of using this research to monitor multiple thermal processes. This shows the potential to address one of the major objectives of this research which is to develop the monitor system to be invariant to the energy source.

In summary, through theoretical and experimental studies, a robust monitoring system was developed with the capability of estimating geometry of different tool paths for different materials and processes. Moreover, the material properties are estimated in real-time by analyzing thermal dynamics of the HAZ. Thermal dynamics can also be predicted in a more cost-effective way by augmenting visible light images with pyrometry measurements. Finally, these measurements can be used with control to improve the consistency of parts produced through thermal processes.

7.2 Future Work

In order to improve the performance and capabilities of monitoring system described in this work, the following suggestions are provided to advance this research:

- It has been shown that geometry and material properties can be monitored with 431 stainless steel powder, 316L stainless steel powder, and Inconel 625 powder. As well as steel wire and in both laser process and arc welding. However, other commonly used materials and processes can be explored to further optimize the measurement algorithms and improve the robustness of the MOC sensor. Different variations of AM and welding can be explored as well to prove the robustness of the system devised in this work.
- Currently, the cooling rate has been studied to determine the material properties of the final product. However, since the temperature distribution of a large region of the HAZ is measured, other thermal dynamics can be measured. Average thermal gradient and heating rate may have significant correlation to the material properties and can be used in addition to or instead of the cooling rate calculations.
- Literature has shown that images have been used with ML to predict porosity in thermal processes. Since this research has already extensively discussed the use of imaging to extract features and ML to augment those measurements, there is room to use this combination for porosity measurements. Other defects may be detectable using this combination of sensors as well. ML algorithms can also be improved by utilizing other features in their models, such as material properties, input energy, and powder feed rate. This additional process insight may improve the ML predictions or allow for other features to be predicted in real time. Investigating the performance in a higher domain shift and ensuring training is appropriate would also improve the implementation of ML in this work.

- The temperature of the HAZ is directly related to the intensity of light it radiates, which allows the temperature to be monitored with imaging. One of the benefits of using a visible light sensor for temperature measurements is the ability to change the camera settings allowing for variable image quality. Therefore, it may be possible to adjust the exposure time to change the temperature range that can be predicted with the visible light camera. However, a different validation tool would need to be implemented than the IR camera used in this work. Moreover, having a pyrometer positioned at the center of the melt pool and a CMOS camera capturing the entire HAZ may allow for emissivity invariant temperatures to be measured at the center of the melt pool. With both the pyrometer and CMOS camera capturing intensity of the center of the melt pool at different wavelengths the temperature can be estimated based on the ratio of light intensity. This measurement would be invariant to emissivity and the surrounding temperatures may be estimated based on the center temperature and intensity of the CMOS image, as outlined in this work.

References

[1] A. Saboori, G. Piscopo, M. Lai, A. Salmi and S. Biamino, "An investigation on the effect of deposition pattern on the microstructure, mechanical properties and residual stress of 316L produced by Directed Energy Deposition," *Materials Science & Engineering A*, vol. 780, 2020.

[2] Z.-j. Tang, W.-w. Liu, Y.-w. Wang, K. M. Saleheen, Z.-c. Liu, S.-t. Peng, Z. Zhang and H.-c. Zhang, "A review on in situ monitoring technology for directed energy deposition of metals," *The International Journal of Advanced Manufacturing Technology,* vol. 108, p. 3437–3463, 2020.

[3] J. Dutta Majumdar and I. Manna, "Laser material processing," *International Materials Reviews,* vol. 56, no. 5, pp. 341-388, 2011.

[4] M. Keskitalo, J. Sundqvist, K. Mantjarvi, J. Powell and A. F. H. Kaplan, "The influence of shielding gas and heat input on the mechanical properties of laser welds in ferritic stainless steel," *Physics Procedia,* vol. 78, pp. 222-229, 2015.

[5] D. Thomas, "Costs, benefits, and adoption of dditive manufacturing: a suply chain perspective," *The international Journal of Advanced Manufacturing Technology,* vol. 85, pp. 1857-1876, 2015.

[6] L. Nickels, "Inside out 3d printing," *Metal Powder Report,* vol. 73, no. 3, pp. 148-150, 2018.

[7] G. Bi, C. N. Sun and A. Grasser, "Study on influential factors for process monitoring and control in laser aided additive manufacturing," *Journal of Material Processing Technology,* vol. 213, no. 3, pp. 463-468, 2013.

[8] D. Y. You, X. D. Gao and S. Katayama, "Review of laser welding monitoring," *Science and Technology of Welding and Joining,* vol. 19, no. 3, pp. 181-201, 2014.

[9] P. Sforza and D. de Blasiis, "On-line optical monitoring system for arc welding," *NDT & E International,* vol. 35, no. 1, pp. 37-43, 2002.

[10] S. Donadello, M. Motta, A. Gokhan Demir and B. Previtali, "Monitoring of laser metal deposition height by means of coaxial laser triangulation," *Optics and Lasers in Engineering,* vol. 112, pp. 136-144, 2019.

[11] Y. Cao, S. Zhu , X. Liang and W. Wang, "Overlapping model of beads and curvefitting of bead section for rapid manufacturing by robotic MAG welding process," *Robotics andComputer-IntegratedManufacturing,* vol. 27, pp. 641-645, 2011.

[12] H. El Cheikh, B. Courant, S. Branchu, X. Huang, J.-Y. Hascoet and R. Guillen, "Direct Laser Fabrication process with coaxial powder projection of 316L steel. Geometrical characteristics and microstructure characterization of wall structures," *Optics and Lasers in Engineering,* vol. 50, pp. 1779-1784, 2012.

[13] M. Iravani-Tabrizipour and E. Toyserkani, "An image based feature tracking algorithm for real-time measurement of clad height," *Machine Vision and Applications,* vol. 18, pp. 343-354, 2007.

[14] L. Song, V. Bagavath-Singhm, B. Dutta and J. Mazu, "Control of melt pool temperature and deposition height during direct metal deposition process," *International Journal of Advanced Manufacturing Technology,,* vol. 58, pp. 247-256, 2011.

[15] R. Yu, Y. Cao, H. Chen, Q. Ye and Y. M. Zhang, "Deep learning based real-time and in-situ monitoring of weld penetration: Where we are and what are needed revolutionary solutions?," *Journal of Manufacturing Processes,* vol. 93, pp. 15-46, 2023.

[16] Y. M. Zhang, H. S. Song and G. Saeed, "Observation of a dynamic specular weld pool surface.," *Measurement Science and Technology,* vol. 17, no. 6, 2006.

[17] J. T. Hofman, B. Pathirai, J. van Dijk, D. F. de Lange and J. Meijer, "A camera based feedback control strategy for the laser cladding process," *Journal of Materials Processing Technology,* vol. 212, no. 11, pp. 2455-2462, 2012.

[18] Y. Ding, J. Warton and R. Kovacevic, "Development of sensing and control system for robotized laser-based direct metal addition system," *Additive Manufacturing,* vol. 10, pp. 24-35, 2016.

[19] S. Liu, P. Farahmand and R. Kovacevic, "Optical monitoring of high power direct diode laser cladding," *Optics & Laser Technology,* vol. 64, pp. 363-376, 2014.

[20] P. Aubry, M. Guiraud and R. Fabbro, "Process control on laser cladding for direct manufacturing: Control of the width and height of the deposited material by coaxial vision," in *Pacific International Conference on Applications of Lasers and Optics*, Beijing, People's Republic of China, 2008 .

[21] J. Suh, "Method and System for Real-Time Monitoring and Controlling Height of Deposit by Using Image Photographing and Image Processing Technology in Laser Cladding and Laser-Aided Direct Metal Manufacturing Process". United States of America Patent 7423236, 2008.

[22] F. Meriaudeau, F. Truchetet, D. Grevey and A. B. Vannes, "Laser Cladding Process and Image Processing," *Journal of Lasers in Engineering,* vol. 6, pp. 161-187, 1997.

[23] B. Wang, S. J. Hu, L. Sun and T. Freiheit, "Intelligent welding system technologies: State-of-the-art review and perspectives," *Journal of Manufacturing Systems,* vol. 56, pp. 373-391, 2020.

[24] C. Zhao, K. Fezzaa, R. W. Cunningham, H. Wen, F. De Carlo, L. Chen, A. D. Rollet and T. Sun, "Real-time monitoring of laser powder bed fusion process using high-speed X-ray imaging and diffraction," *Scientific Reports,* vol. 7, no. 3602, pp. 1-11, 2017.

[25] C. Knaak, U. Thombansen, P. Abels and M. Kroger, "Machine learninf as a comparative tool to determine the relevance of signal features in laser welding," *Procedia CIRP,* vol. 74, pp. 623-627, 2018.

[26] N. D. Jamnikar, S. Liu, C. Brice and X. Zhang, "In-process comprehensive prediction of bead geometry for laser wire-feed DED system using molten pool sensing data and multi-modality CNN," *The International Journal of Advanced Manufacturing Technology,* vol. 121, p. 903–917, 2022.

[27] I. Jeon, L. Yang, K. Ryu and H. Sohn, "Online melt pool depth estimation during directed energy deposition using coaxial infrared camera, laser line scanner, and artificial neural network," *Additive Manufacturing,* vol. 47, 2021.

[28] I. Garmendia, J. Flores, M. Madarieta, A. Lamikiz, L. G. Uriarte and C. Soriano, "Geometrical control of DED processes based on 3D scanning applied to the manufacture of complex parts," in *11th CIRP Conference on Photonic Technologies*, Fuerth, Germany, 2020.

[29] J. Mi, Y. Zhang, H. Li, S. Shen, Y. Yang, C. Song, X. Zhou, Y. Duan, J. Lu and H. Mai, "In-situ monitoring laser based directed energy deposition process with deep convolutional neural network," *Journal of Intelligent Manufacturing,* vol. 34, pp. 683-693, 2023.

[30] S. Kim, I. Jeon and H. Sohn, "Infrared thermographic imaging based real-time layer height estimation during directed energy deposition," *Optics and Lasers in Engineering,* vol. 168, 2023.

[31] G. Li, K. Odum, C. Yau, M. Soshi and K. Yamazaki, "High productivity fluence based control of Directed Energy Deposition (DED) part geometry," *Journal of Manufacturing Processes,* vol. 65, pp. 407-417, 2021.

[32] T. A. Davis and Y. C. Shin, "Vision based clad height measurement," *Machine Vision and Applications,* vol. 22, pp. 129-136, 2010.

[33] D. Regulin and R. Barucci, "A benchmark of approaches for closed loop control of melt pool shape in DED," *The International Journal of Advanced Manufacturing Technology,* vol. 126, pp. 829-843, 2023.

[34] J. Yu, M. Rombouts, G. Maes and F. Motmans, "Material properties of Ti6Al4V parts produced by laser metal deposition," *Physics Procedia,* vol. 39, pp. 416-424, 2012.

[35] T. Ressler, J. Wong and J. W. Elmer, "Investigation of Real-Time Microstructure Evolution in Steep Thermal Gradients Using in-Situ Spatially Resolved X-ray Diffraction: A Case Study for Ti Fusion Welds," *The Journal of Physical Chemistry B,* vol. 102, no. 52, pp. 10724-10735, 1998.

[36] W. D. Callister, Jr. and D. G. Rethwisch, "Thermal Processing of Metals," in *Fundamentals of Materials Science and Engineering: An Integrated Approach*, Hoboken, NJ, John Wiley & Sons, Inc., 2012, pp. 601-613.

[37] G. Bi, A. Grasser, K. Wissenbach, A. Drenker and R. Poprawe, "Identification and qualification of temperature signal for monitoring and control in laser cladding," *Optics and Lasers in Engineering,* vol. 44, pp. 1348-1359, 2006.

[38] X. Cai, F. Chen, B. Dong, S. Lin and C. Yang, "Microstructure and mechanical properties of GTA-based wire arc additive manufactured AZ91D magnesium alloy," *Journal of Magnesium and Alloys,* 2022.

[39] B. Zheng, J. C. Haley, N. Yang, J. Yee, K. W. Terrassa, Y. Zhou, E. J. Lavernia and J. M. Shoenung, "On the evolution of microstructure and defect control in 316L SS components fabricated via directed energy deposition," *Materials Science & Engineering A,* vol. 764, 2019.

[40] D. Svetlizky, B. Zhang, A. Vyatskikh, M. Das, S. Bose, A. Bandyopahyay, J. M. Schoenung, E. J. Lavernia and N. Eliaz, "Laser-based directed energy deposition (DED-LB) of advanced materials," *Materials Science & Engineering A,* vol. 840, 2022.

[41] A. Saboori, G. Piscopo, M. Lai, A. Salmi and S. Biamino, "An investigation on the effect of deposition pattern on the microstructure, mechanical properties and residual stress of 316L produced by Directed Energy Deposition," *Materials Science & Engineering A,* vol. 780, 2020.

[42] G. Muvvala, D. P. Karmakar and A. K. Nath, "In-process detection of microstructural changes in laser cladding of in-situ Inconel 718/TiC metal matrix composite coating," *Journal of Alloys and Compounds,* vol. 740, pp. 545-558, 2018.

[43] G. Muvvala, D. P. Karmakar and A. K. Nath, "Online monitoring of thermo-cycles and its correlation with microstructure in laser cladding of nickel based super alloy," *Optics and Lasers in Engineering,* vol. 88, pp. 139-152, 2017.

[44] M. H. Farshidianfar, A. Khajepour and A. P. Gerlich, "Effect of real-time cooling rate on microstructure in Laser Additive Manufacturing," *Journal of Materials Processing Technology,* vol. 231, pp. 468-478, 2016.

[45] G. J. Marshall, W. J. Young II, S. M. Thompcon, N. Shamsaei, S. R. Daniewicz and S. Shao, "Understanding the Microstructure Formation of Ti-6Al-4V During Direct Laser Deposition via In-Situ Thermal Monitoring," *The Journal of The Minerals, Metals & Materials Society (TMS),* vol. 68, pp. 778-790, 2016.

[46] P. A. Kobryn and S. L. Semiatin, "Microstructure and texture evolution during solidification processing of Ti-6A1-4V," *Journal of Materials Processing Technology,* vol. 135, no. 2, pp. 330-339, 2003.

[47] M. H. Farshidianfar, A. Khajepour and A. Gerlich, "Real-time monitoring and prediction of martensite formation and hardening depth during laser heat treatment," *Surface & Coatings Technology,* vol. 315, pp. 326-334, 2017.

[48] A. J. Pinkerton, M. Karadge, W. Ul Haq Syed and L. Li, "Thermal and microstructural aspects of the laser direct metal deposition of waspaloy," *Journal of Laser Applications,* vol. 18, no. 3, pp. 216-226, 2006.

[49] G. L. Knapp, N. Raghavan, A. Plotowski and T. DebRoy, "Experiments and simulations on solidification microstructure for Inconel 718 in powder bed fusion electron beam additive manufacturing," *Additive Manufacturing,* vol. 25, pp. 511-521, 2019.

[50] G. Tapia and A. Elwany, "A Review on Process Monitoring and Control in Metal-Based Additive Manufacturing," *Journal of Manufacturing Science and Engineering,* vol. 136, no. 6, p. 06081, 2014.

[51] W.-W. Liu, Z.-J. Tang, X.-Y. Liu, H.-J. Wang and H.-C. Zhang, "A Review on In-situ Monitoring and Adaptive Control Technology for Laser Cladding Remanufacturing," *Procdeia CIRP,* vol. 61, pp. 235-240, 2017.

[52] Y. Huang, M. Ansari, H. Asgari, M. H. Farshidianfar, D. Sarker, M. B. Khamesee and E. Toyserkani, "Rapid prediction of real-time thermal characteristics, solidification parameters and microstructure in laser directed energy deposition," *Journal of Materials Processing Technology,* vol. 274, p. 116286, 2019.

[53] J. Raplee, A. Plotkowski, M. M. Kirka, R. Dinwiddie, A. Okello, R. R. Dehoff and S. S. Babu, "Thermographic Microstructure Monitoring in Electron Beam Additive Manufacturing," *Scientific Reports,* vol. 7, p. 43554, 2017.

[54] P. S. Mohanty and J. Mazumder, "Solidification Behavior and Microstructural Evolution during Laser Beam–Material Interaction," *Metallurgical and Materials Transactions B,* vol. 29, pp. 1269-1279, 1998.

[55] S. J. Wolff, S. Lin, E. J. Faierson, W. Kam Liu, G. J. Wagner and J. Cao, "A framework to link localized cooling and properties of directed energy deposition (DED)-processed Ti-6Al-4V," *Acta Materialia,* vol. 132, pp. 106-117, 2017.

[56] D. Svetlizky, M. Das, B. Zheng, A. L. Vyatskikh, S. Bose, A. Bandyopadhyay, J. M. Schoenung, E. J. Lavernia and N. Eliaz, "Directed energy deposition (DED) additive manufacturing: Physical characteristics, defects, challenges and applications," *Materials Today,* vol. 49, pp. 271-295, 2021.

[57] C. Vundru, R. Singh, W. Yan and S. Karagadde, "A comprehensive analytical-computational model of laser directed energy deposition to predict deposition geometry and integrity for sustainable repair," *International Journal of Mechanical Sciences,* vol. 211, 2021.

[58] Y. Huang, M. Ansari, H. Asgari, M. H. Farshidianfar, D. Sarker, M. B. Khamesee and E. Toyserkani, "Rapid prediction of real-time thermal characteristics, solidification parameters and microstructure in laser directed energy deposition (powder-fed additive manufacturing)," *Journal of Materials Processing Technology,* vol. 274, 2019.

[59] S. J. Wolff, Z. Gan, S. Lin, J. L. Bennett, W. Yan, G. Hyatt, K. F. Ehmann, G. J. Wagner, W. Kam Liu and J. Cao, "Experimentally validated predictions of thermal history and microhardness in laser-deposited Inconel 718 on carbon steel," *Additive Mnufacturing,* vol. 27, pp. 540-551, 2019.

[60] Y. Guo, G. Quan, Y. Jiang, L. Ren, L. Fan and H. Pan, "Formability, microstructure evolution and mechanical properties of wire arc additively manufactured AZ80M magnesium alloy using gas tungsten arc welding," *Journal of Magnesium and Alloys,* vol. 9, pp. 192-201, 2021.

[61] W. Fan, H. Tan, F. Zhang, Z. Feng, Y. Wang, L.-C. Zhang, X. Lin and W. Huang, "Overcoming the limitation of in-situ microstructural control in laser additive manufactured Ti–6Al–4V alloy to enhanced mechanical performance by integration of synchronous induction heating," *Journal of Materials Science & Technology,* vol. 94, pp. 32-46, 2021.

[62] J. Shao, G. Yu, S. Li, X. He, C. Tian and B. Dong, "Crystal growth control of Ni-based alloys by modulation of the melt pool morphology in DED," *Journal of Alloys and Compounds,* vol. 898, 2022.

[63] Y. P. Hu, C. W. Chen and K. Mukherjee, "Measurement of temperature distributions during laser cladding process," *Journal of Laser Applications,* vol. 12, no. 3, pp. 126-130, 2000.

[64] K. L. Ness, A. Paul, L. Sun and Z. Zhang, "Towards a generic physics-based machine learning model for geometry invariant thermal history prediction in additive manufacturing," *Journal of Materials Processing Technology,* vol. 302, 2022.

[65] A. Paul, M. Mozaffar, Z. Yang, W.-k. Liao, A. Choudhary, J. Cao and A. Agrawal, "A real-time iterative machine learning approach for temperature profile prediction in additive manufacturing processes," in *2019 IEEE International Conference on Data Science and Advanced Analytics (DSAA)*, Washington, DC, 2019.

[66] E. Mirkoohi, J. Ning, P. Bocchini, O. Fergani, K.-N. Chiang and S. Y. Liang, "Thermal Modeling of Temperature Distribution in Metal Additive Manufacturing Considering Effects of Build Layers, Latent Heat, and Temperature-Sensitivity of Material Properties," *Manufacturing and Materials Processing,* vol. 2, no. 63, 2018.

[67] L. Heinrich, T. Feldhausen, K. S. Saleeby, C. Saldana and T. R. Kurfess, "PREDICTION OF THERMAL CONDITIONS OF DED WITH FEA METAL ADDITIVE SIMULATION," in *ASME 2021 16th International Manufacturing Science and Engineering Conference*, Virtual, Online, 2021.

[68] S. Liao, S. Webster, D. Huang, R. Council, K. Ehmann and J. Cao, "Simulation-guided variable laser power design for melt pool depth control in directed energy deposition," *Additive Manufacturing,* vol. 56, 2022.

[69] X.-x. Yao, J.-y. Li, Y.-f. Wang, X. Gao and Z. Zhang, "Numerical simulation of powder effect on solidification in directed energy deposition additive manufacturing," *Transactions of Nonferrous Metals Society of China,* vol. 31, no. 9, pp. 2871-2884, 2021.

[70] Y. Lian, Z. Gan, C. Yu, D. Kats, W. K. Liu and G. J. Wagner, "A cellular automaton finite volume method for microstructure evolution during additive manufacturing," *Materials and Design,* vol. 169, 2019.

[71] X. X. Yao, X. Gao and Z. Zhang, "Three-dimensional microstructure evolution of Tie6Ale4V during multi-layer printing: a phase-field simulation," *Journal of Materials Research and Technology*, vol. 20, pp. 934-949, 2022.

[72] S. Fetni, Q. D. Thinh Pham, V. X. Tran, L. Duchêne, H. Son Tran and A. M. Habraken, "Thermal field prediction in DED manufacturing process using Artificial Neural Network," in *24th International Conference on Material Forming*, Liège, Belgium, 2021.

[73] K. S. Kumar, "Analytical Modeling of Temperature Distribution, Peak Temperature, Cooling Rate and Thermal Cycles in a Solid Work Piece Welded By Laser Welding Process," *Procedia Materials Science*, vol. 6, pp. 821-834, 2014.

[74] P. Farahmand and R. Kovacevic, "An experimental–numerical investigation of heat distribution and stress field in single- and multi-track laser cladding by a high-power direct diode laser," *Optics & Laser Technology*, vol. 63, pp. 154-168, 2014.

[75] M. H. Farshidianfar, *Real-Time Closed-Loop Control of Microstructure and Geometry in Laser Materials Processing*, Waterloo, Ontario, Canada: Ph. D. Thesis, University of Waterloo, 2017.

[76] W. Devesse, D. De Baere, M. Hinderdael and P. Guillaume, "High resolution temperature estimation during laser cladding of stainless steel," *Physics Procedia*, vol. 83, pp. 1253-1260, 2016.

[77] L. Hong, I. Leong-Teng, A. Mackroy, L. Werrett, J. Scott, D. Tree and L. Baxter, "Particle Surface Temperature Measurements with Multicolor Band Pyrometry," *AIChE Journal*, vol. 55, no. 1, pp. 243-255, 2009.

[78] C. Gobbi, *Low Cost Thermal Imaging System for Welding Applications*, Waterloo, Ontario, Canada: M. A. Sc. Thesis, University of Waterloo, 2016.

[79] Z. Zhang, Z. Liu and D. Wu, "Prediction of melt pool temperature in directed energy deposition using machine learning," *Additive Manufacturing*, vol. 37, 2021.

[80] J. Xie, Z. Chai, L. Xu, X. Ren, S. Liu and X. Chen, "3D temperature field prediction in direct energy deposition of metals using physics informed neural network," *The International Journal of Advanced Manufacturing Technology*, vol. 119, p. 3449–3468, 2022.

[81] J. L. Bennett, O. L. Kafka, H. Liao, S. J. Wolff, C. Yu, P. Cheng, G. Hyatt, K. Ehmann and J. Cao, "Cooling rate effect on tensile strength of laser deposited Inconel 718," *Procedia Manufacturing*, vol. 26, pp. 912-919, 2018.

[82] C. Hagenlocher, P. O'Toole, W. Xu, M. Brandt, M. Easton and A. Molotnikov, "In process monitoring of the thermal profile during solidification in laser directed energy deposition of aluminium," *Additive Manufacturing Letters*, vol. 3, 2022.

[83] J. Jeong, S. Webster, S. Liao, J.-E. Mogonye, K. Ehmann and J. Cao, "Cooling rate measurement in directed energy deposition using photodiode-based planck thermometry (PDPT)," *Additive Manufacturing Letters*, vol. 3, 2022.

[84] M. H. Farshidianfar, F. Khodabakhshi, A. Khajepour and A. P. Gerlich, "Closed-loop control of microstructure and mechanical properties in additive manufacturing by directed energy deposition," *Materials Science & Engineering A*, vol. 803, 2021.

[85] M. Schrödera, B. Falk and R. Schmitt, "Evaluation of Cost Structures of Additive Manufacturing Processes Using a New Business Model," *Procedia CIRP*, vol. 30, pp. 311-316, 2015.

[86] M. Mani, B. M. Lane, M. A. Donmez, S. C. Feng, S. P. Moylan and R. R. Fesperman Jr., *Measurement Science Needs for Real-Time Control of Additive Manufacturing Powder Bed*

Fusion Processes, Gaithersburg, MD, USA: US Department of Commerce, National Institute, 2015.

[87] A. Sun, E. Kannatey-Asibu, Jr. and M. Gartner, "Sensor systems for real-time monitoring of laser weld quality," *Journal of Laser Applications*, vol. 11, no. 4, pp. 153-168, 1999.

[88] A. Sumesh, K. Rameshkumar, K. Mohandas and R. Shyam Babu, "Use of Machine Learning Algorithms for Weld Quality Monitoring using Acoustic Signature," *Procedia Computer Science*, vol. 50, pp. 316-322, 2015.

[89] S. A. Shevchik, C. Kenel, C. Leinenbach and K. Wasmer, "Acoustic emission for in situ quality monitoring in additive manufacturing using spectral convolutional neural networks," *Additive Manufacturing*, vol. 21, pp. 598-604, 2018.

[90] S. Liu, W. Liu, M. Harooni, J. Ma and R. Kovacevic, "Real-time monitoring of laser hot-wire cladding of Inconel 625," *Optics & Laser Technology*, vol. 62, pp. 124-134, 2014.

[91] B. Cheng, J. Lei and H. Xiao, "A photoacoustic imaging method for in-situ monitoring of laser assisted ceramic additive manufacturing," *Optics and Laser Technology*, vol. 115, p. 459–464, 2019.

[92] L. Grad, J. Grum, I. Polajnar and J. M. Slabe, "Feasibility study of acoustic signals for on-line monitoring in short circuit gas metal arc welding," *International Journal of Machine Tools & Manufacture*, vol. 44, pp. 555-561, 2004.

[93] M. Khanzadeh, W. Tian, A. Yadollahi, H. R. Doude, M. A. Tschopp and L. Bian, "Dual process monitoring of metal-based additive manufacturing using tensor decomposition of thermal image streams," *Additive Manufacturing*, vol. 23, pp. 443-456, 2018.

[94] U. Sreedhar, C. V. Krishnamurthy, K. Balasubramaniam, V. D. Raghupathy and S. Ravisankar, "Automatic defect identification using thermal image analysis for online weld quality monitoring," *Journal of Materials Processing Technology*, vol. 212, pp. 1557-1566, 2012.

[95] C. E. Seow, J. Zhang, H. E. Coules, G. Wu, C. Jones, J. Ding and S. Williams, "Effect of crack-like defects on the fracture behaviour of Wire + Arc Additively Manufactured nickel-base Alloy 718," *Additive Manufacturing*, vol. 36, p. 101578, 2020.

[96] U. Hassler, D. Gruber, O. Hentschel, F. Sukowski, T. Grulich and L. Seifert, "In-situ monitoring and defect detection for laser metal deposition by using infrared thermography," *Pysics Procedia*, vol. 83, pp. 1244-1252, 2016.

[97] Y. Ma, Z. Hu, Y. Tang, S. Ma, Y. Chu, X. Li, W. Luo, L. Guo, X. Zeng and Y. Lu, "Laser opto-ultrasonic dual detection for simultaneous compositional, structural, and stress analyses for wire + arc additive manufacturing," *Additive Manufacturing*, vol. 31, p. 100956, 2020.

[98] F. Imani, A. Gaikwad, M. Montezari, P. Rao, H. Yang and E. Reutzel, "Layerwise in-process quality monitoring in laser powder bed fusion," in *ASME 2018 13th International Manufacturing Science and Engineering Conference*, College Station, TX, USA, 2018.

[99] B. Zhang, K.-M. Hong and Y. C. Shin, "Deep-learning-based porosity monitoring of laser welding process," *Manufacturing Letters*, vol. 23, pp. 62-66, 2020.

[100] B. Zhang, S. Liu and Y. C. Shin, "In-Process monitoring of porosity during laser additive manufacturing process," *Additive Manufacturing*, vol. 28, pp. 497-505, 2019.

[101] 3D Systems, "DMP Monitoring," 3D Systems, 2020. [Online]. Available: https://www.3dsystems.com/dmp-monitoring-solution. [Accessed 10 October 2020].

[102] S. Coeck, M. Bisht, J. Plas and F. Verbist, "Prediction of lack of fusion porosity in selective laser melting based on melt pool monitoring data," *Additive Manufacturing,* vol. 25, pp. 347-356, 2019.

[103] Y. Zhang, S. Shen, H. Li and Y. Hu, "Review of in situ and real-time monitoring of metal additive manufacturing based on image processing," *The International Journal of Advanced Manufacturing Technology,* vol. 123, pp. 1-20, 2022.

[104] A. Chabot, M. Rauch and J. Y. Hascoet, "Towards a multi-sensor monitoring methodology for AM metallic processes," *Welding in the World,* vol. 63, pp. 759-769, 2019.

[105] R. Avci, B. H. Davis, N. Rieders and K. Lucas, "Role of Metallurgy in the Localized Corrosion of Carbon Steel," *Journal of Minerals and Materials Characterization and Engineering,* vol. 6, no. 6, pp. 618-646, 2018.

[106] Optris, "Thermal Imager PI08M," 2015. [Online]. Available: https://www.optris.com/thermal-imager-pi-08m.

[107] Photonfocus, *MV1-D1312(IE/C) Camera Series: CMOS camera with GigE interface,* MAN049 08/2018 V1.5 ed., 2018.

[108] E. Hecht, "Geometrical Optics," in *Optics*, London, United Kingdom, Pearson Education Limited, 2017, pp. 159-254.

[109] Midwest Optical Systems, "Neutral Density Filters," 2022. [Online]. Available: https://midopt.com/filters/neutral-density/.

[110] "45° AOI, 25.0mm Square, Cold Mirror," Edmund Optics, 2021. [Online]. Available: https://www.edmundoptics.com/p/45deg-aoi-250mm-square-cold-mirror/19160/. [Accessed October 2019].

[111] Thor Labs, "Cube-Mounted Pellicle Beamsplitters," 2013. [Online]. Available: https://www.thorlabs.com/newgrouppage9.cfm?objectgroup_id=4138.

[112] Coherent, *Prealigned External Optics D50 - Product Manual,* Aminogatan 30, SE 431 53 Mölndal, Sweden: Optoskand AB, 2018.

[113] I. Smurov, M. Doubenskaia and A. Zaitsev, "Comprehensive analysis of laser cladding by means of optical diagnostics and numberical simulation," *Surface & Coatings Technology,* vol. 220, pp. 112-121, 2013.

[114] H. Schopp, A. Sperl, R. Kozakov, G. Gott, D. Uhrlandt and G. Wilhelm, "Temperature and emissivity determination of liquid steel S235," *Journal of Physics D: Applied Physics,* vol. 45, p. 235203, 2012.

[115] W. Devesse, D. De Baere and P. Guillaume, "High Resolution Temperature Measurement of Liquid Stainless Steel Using Hyperspectral Imaging," *Sensors,* vol. 17, no. 1, pp. 91 - 103, 2017.

[116] S. Altenburg, N. Scheuschner, A. Straße, G. Andrey and C. Maierhofer, "Towards the determination of real process temperatures in the LMD process by multispectral thermography," in *SPIE 11743, Thermosense: Thermal Infrared Applications XLIII*, 117430B , 2021.

[117] W. A. Belson, "Matching and Prediction on the Principle of Biological Classification," *Journal of the Royal Statistical Society. Series C (Applied Statistics),* vol. 8, no. 2, pp. 65-75, 1959.

[118] Y. A. Cengel and A. J. Ghajar, Heat and Mass Transfer: Fundamentals & Applications, Fifth ed., New York, NY: McGraw Hill, 2011.

[119] H. Kwon, W.-K. Baek, M.-S. Kim, W.-S. Shin and J. J. Yoh, "Temperature-dependent absorptance of painted aluminum, stainless steel 304, and titanium for 1.07 μm and 10.6 μm laser beams," *Optics and Lasers in Engineering,* vol. 50, no. 2, pp. 112-121, 2012.

[120] H. El Cheikh, B. Courant, S. Branchu, J.-Y. Hascoet and R. Guillen, "Analysis and prediction of single laser tracks geometrical charactistics in coaxial laser cladded process," *Optics and Lasers in Engineering,* vol. 50, pp. 413-422, 2012.

[121] P. Ranefall and C. Wahlby, "Global Gray-Level Thresholding Based on Object Size," *Cytometry Part A,* vol. 89, no. A, pp. 385-390, 2016.

[122] Y.-Y. Chang, J.-R. Qui and S.-J. Hwang, "Multi-objective optimization of directed energy deposition process by using Taguchi-Grey relational analysis," *The International Journal of Advanced Manufacturing Technology,* vol. 120, p. 7547–7563, 2022.

[123] M. N. Ozisik, "Moving Heat Source Problems," in *Heat Conduction*, New York, NY, John Wiley & Sons, 1993, pp. 372-389.

[124] P. Barnard, "4 - Austenitic steel grades for boilers in ultra-supercritical power plants," in *Materials for Ultra-Supercritical and Advanced Ultra-supercritical Power Plants*, Woodhead Publishing, 2017, pp. 99-119.

[125] P. Alvaredo, S. A. Tsipas and E. Gordo, "Influence of carbon content on the sinterability of an FeCr matrix cermet reinforced with TiCN," *International Journal of Refractory Metals and Hard Materials,* vol. 36, pp. 283-288, 2013.

[126] T. E. Abioye, D. G. McCartney and A. T. Clare, "Laser cladding of Inconel 625 wire for corrosion protection," *Journal of Materials Processing Technology,* vol. 217, pp. 232-240, 2015.

[127] P. D. C. Assuncao, R. A. Ribeiro, P. M. G. P. Moreira, E. Braga and A. Gerlich, "A preliminary study on the double cold wire gas metal arc welding process," *The international Journal of Advanced Manufacturing Technology,* vol. 106, no. 11, 2020.

[128] C. Xia , Z. Pan, J. Polden, H. Li, Y. Xu, S. Chen and Y. M. Zhang, "A review on wire arc additive manufacturing: Monitoring, control and a framework of automated system," *Journal of Manufacturing Systems,* vol. 57, pp. 31-45, 2020.

[129] Z. Liu, H. Qi and L. Jiang, "Control of crystal orientation and continuous growth through inclination of coaxial nozzle in laser powder deposition of single-crystal superalloy," *Journal of Materials Processing Technology,* vol. 230, pp. 177-186, 2016.

[130] E. Malekipour and H. El-Mounayri, "Common defects and contributing parameters in powder bed fusion AM process and their classification for online monitoring and control: a review," *The International Journal of Advanced Manufacturing Technology,* vol. 95, pp. 527-550, 2018.

[131] D. Masaylo, S. Igoshin, A. Popovich and V. Popovich, "Effect of process parameters on defects in large scale components manufactured by direct laser deposition," *Materials Today: Proceedings,* 2020.